# A Cellular Automata Approach for the Simulation and Development of Advanced Phase Change Memory Devices

Submitted by

## Jorge Alberto Vázquez Diosdado

to the University of Exeter as a thesis for the degree of Doctor of Philosophy (PhD) in

Mathematics, November 2012.

..........................

Jorge Alberto Vázquez Diosdado

# Abstract

Phase change devices in both optical and electrical formats have been subject of intense research since their discovery by Ovshinsky in the early 1960's. They have revolutionized the technology of optical data storage and have very recently been adopted for non-volatile semiconductor memories. Their great success relies on their remarkable properties enabling high-speed, low power consumption and stable retention. Nevertheless, their full potential is still yet to be realized.

Operations in electrical phase change devices rely on the large resistivity contrast between the crystalline (low resistance) and amorphous (high resistance) structures. The underlying mechanisms of phase transformations and the relation between structural and electrical properties in phase change materials are quite complex and need to be understood more deeply. For this purpose, we compare different approaches to mathematical modelling that have been suggested to realistically simulate the crystallization and amorphization of phase change materials. In this thesis the recently introduced Gillespie Cellular Automata (GCA) approach is used to obtain direct simulation of the structural phases and the electrical states of phase change materials and devices. The GCA approach is a powerful technique to understand the nanostructure evolution during the crystallization (SET) and amorphization (RESET) processes in phase change devices over very wide length scales. Using this approach, a detailed study of the electrical properties and nanostructure dynamics during SET and RESET processes in a PCRAM cell is presented.

Besides the possibility of binary storage in phase change memory devices, there is a wider and far-reaching potential for using them as the basis for new forms of arithmetic and cognitive computing. The origin of such potential lies in a previously under-explored

property, namely accumulation which has the potential to implement basic arithmetic computations. We exploit and explore this accumulative property in films and devices. Furthermore, we also show that the same accumulation property can be used to mimic a simple integrate and fire neuron. Thus by combining both a phase change cell operating in the accumulative regime for the neural body and a phase change cell in the multilevel regime for the synaptic weighting an artificial neuromorphic system can be obtained. This may open a new route for the realization of phase change based cognitive computers.

This thesis also examines the relaxation oscillations observed under suitable bias conditions in phase change devices. The results presented are performed through a circuit analysis in addition with a generation and recombination mechanism driven by the electric field and carrier densities. To correctly model the oscillations we show that it is necessary to include a parasitic inductance.

Related to the electrical states of phase change materials and devices is the threshold switching of the amorphous phase at high electric fields and recent work has suggested that such threshold switching is the result of field-induced nucleation. An electric field induced nucleation mechanism is incorporated into the GCA approach by adding electric field dependence to the free energy of the system. Using results for a continuous phase change thin films and PCRAM devices we show that a purely electronic explanation of threshold switching, rather than field-induced nucleation, provides threshold fields closer to experimentally measured values.

# Acknowledgements

It would not have been possible to write this doctoral thesis without the help and support of the kind people around me, only some of whom it is possible to mention here. Above all, I would like to thank my wife Janely for all her love, personal support and great patience at all times. My parents deserve special mention for their support and prayers. My Father, Manuel, is the person who put the base of my character, showing me to never give up ever since I was a child. My Mother, Ma. Lucia, is the one who sincerely raised me with her caring and gentle love. She showed me that the strength of my beliefs determine the power of my personality. To my sister Ana for caring about me and to my brother Jose whose hard work has been an excellent example to me.

This thesis would not have been possible without the help, support and patience of my principal supervisor, Prof. Peter Ashwin, not to mention his advice and unsurpassed knowledge of Mathematics. He has taught me, both consciously and unconsciously, how good applied mathematics are done. I appreciate all his contributions of time and ideas to make my PhD experience productive and stimulating. The joy and enthusiasm he has for his research was contagious and motivational for me, even during tough times in the PhD pursuit. I am also thankful for the excellent example he has provided as a successful mathematician and professor. The good advice and support of my second supervisor, Prof. C.D Wright, has been invaluable on both an academic and a personal level, for which I am extremely grateful. In addition, he was always accessible and willing to help his students with their research. He also generously provided financial support for this research.

The field induced crystallization studies discussed in this dissertation would not have been possible without the helpful discussions with Dr. Krisztian Kohary. I am very

appreciative of his generosity, time, advice, data, and references, to name but a few of his contributions.

I would also like to thank Dr. Mustafa Aziz for his assistance and guidance in the modeling with Comsol Multiphysics. He provided valuable discussions and training on the software during my PhD.

The members of the Functional Materials group have contributed immensely to my personal and professional time at Exeter. The group has been a source of friendships as well as good advice and collaboration. I am especially grateful to: Maria Marklove, Raphael Matelon, Hosseini Peiman, Purav Shah, Lei Wang, Gerardo Rodriguez, Iva Kavcic, Christian Bick, Alejandro Quiroz and Carlos Martinez.

Last but not least, thanks be to God for my life through all tests in the past three years.

# Contents

# List of Figures

9

# List of Tables

# Chapter 1

# Introduction and motivation

## 1.1 Development of data storage technologies

Data storage devices currently available in the market can be classified into two types: slow non-volatile memories and faster volatile memories. A volatile memory loses the data when the power is off. By contrast, non-volatile memories retain information even if encountering a power cut. Volatile memories can exhibit operational speeds of some nanoseconds which are possible to achieve by using CMOS transistors, in the SRAM concept, and small capacitors, in the DRAM concept. In the static random access memory (SRAM) each memory bit is usually stored in four transistors, while two additional transistors are used to control the access to the storage cell during write and read operation. In SRAM a constant application of a supply voltage is needed to maintain the transistor state. Nowadays, the SRAM concept is mostly used in computers embedded with the central processor unit (CPU) and these SRAMs are general high performance level 1 (L1) and Level (L2) cache memories [1].

The Dynamic random access memory (DRAM) is another common type of volatile memory, where each bit comprises a capacitor and a transistor. The leaking charge of the capacitor causes repetitive refreshing to restore the data which generates an extra power consumption limiting this technology. Recently a DRAM cell with several transistor structures have been investigated to overcome the leaking current [2].

In contrast to these purely electronic memory concepts, many other types of mem-

ory devices are used for long term storage. Magnetic disks and optical disks are two dominant storage mediums in this type which allow large storage capacity. In hard disk drives (HDD) and magnetic tapes, the electronic information is converted to different orientations of magnetic domains in ferro-magnetic materials. The information in these devices has a very long lifetime while the operation speed is in the range of milliseconds, or higher.

In optical recording technology (such as CD, DVD, and Blu-ray disks) information is recorded by a laser beam changing the reflectivity of a polymer or a phase-change material [3]. A major difference between optical and magnetic recording is that the former has the ability to be removable and has a relatively low cost. However the highest areal density in optical recording is limited by the diffraction limit, related to the minimum optical spot size, which is proportional to the wavelength of the laser. There are several paths to improve the areal density, including near field optical recording [4], optical multiplexing [5], and holographic optical storage [6], all of which have been investigated. By 2015, optical recording could reach 1 Tb/in$^2$ storage density [7].

Flash memory was introduced as a bridge between volatile electronic memories and non-volatile storage devices [8]. In flash memory, data is stored as in DRAM concept, i.e. using a small capacitor, but with an additional floating gate (FG). Under high electric fields, the additional floating gate (insulated by an oxide layer) will produce a tunneling of electrons to the gate. Any electrons placed in the (FG) can remain there without significant discharge, which defines flash devices as being a non-volatile memory. The read process in flash memories can be performed within some microseconds whereas writing, and especially deleting, are in range comparable to with HDDs. However, due to well known scaling limits, flash memories face steep challenges to achieve higher densities. For example in NAND flash, as geometries decrease, cell-to-cell interference increases while each floating gate stores a diminishing number of electrons making it difficult to keep sufficient gate control [9].

Phase change random access memory (PCRAM) has been intensively investigated in the last decade. Research in the field concerning the electronic properties, materials properties and device technology of phase-change materials have made them able to

compete with rival technologies such as Flash. Their characteristics are close to that of DRAM and flash memory. The operation of PCRAM is similar to that of phase change optical memory, except that the heat source is an electrical current pulse inducing atomic rearrangements of the material. This rearrangement in the structure of the material distinguishes two different phases: amorphous and crystalline. The large resistivity contrast between amorphous (high resistivity) and crystalline (low resistivity) phases can be used to store information for several years.

PCRAM has achieved significant improvements in the reduction of size with a $90nm$ commercial product as a NOR replacement [10], and a 45-nm technology demonstration [11] now available, and there is evidence that it may scale down to nanometer size (2-5nm) in all three dimensions [12]. Even more importantly, the capability of multiple bits per cell operation [13] gives PCRAM an opportunity to reach ultrahigh density. PCRAM exhibits excellent reliability properties, such as good data retention (10 years at 110 ℃), and a very high endurance [14] (up to the endurance of $10^{12}$ cycles). Configurations with single-wall and small-diameter multi-wall carbon nanotube electrodes show a dramatic reduction of the program current down to 0.5 $\mu$A (set) and 5 $\mu$A (reset) [15]. Because of these remarkable features compared to other nonvolatile memories, PCRAM can be considered to have a promising future. To deliver this promising future effectively and efficiently, we need good models of whole device behaviour.

## 1.2    Characteristics of phase change materials

Phase change materials are named because they possess two structurally distinct solid phases: amorphous and crystalline. These two different solid phases possess unusually contrasting physical properties, such as the dielectric constant, optical reflectivity and electrical resistivity. These differences can be used to store information in technological applications and to switch the material repeatedly between the two phases, if both phases are stable at operating temperature. A schematic diagram of the phase transition is shown in Figure 1.1.

The transformation of the metastable amorphous phase to the more energetically favourable stable crystalline (SET-operation) requires annealing of an amorphous bit
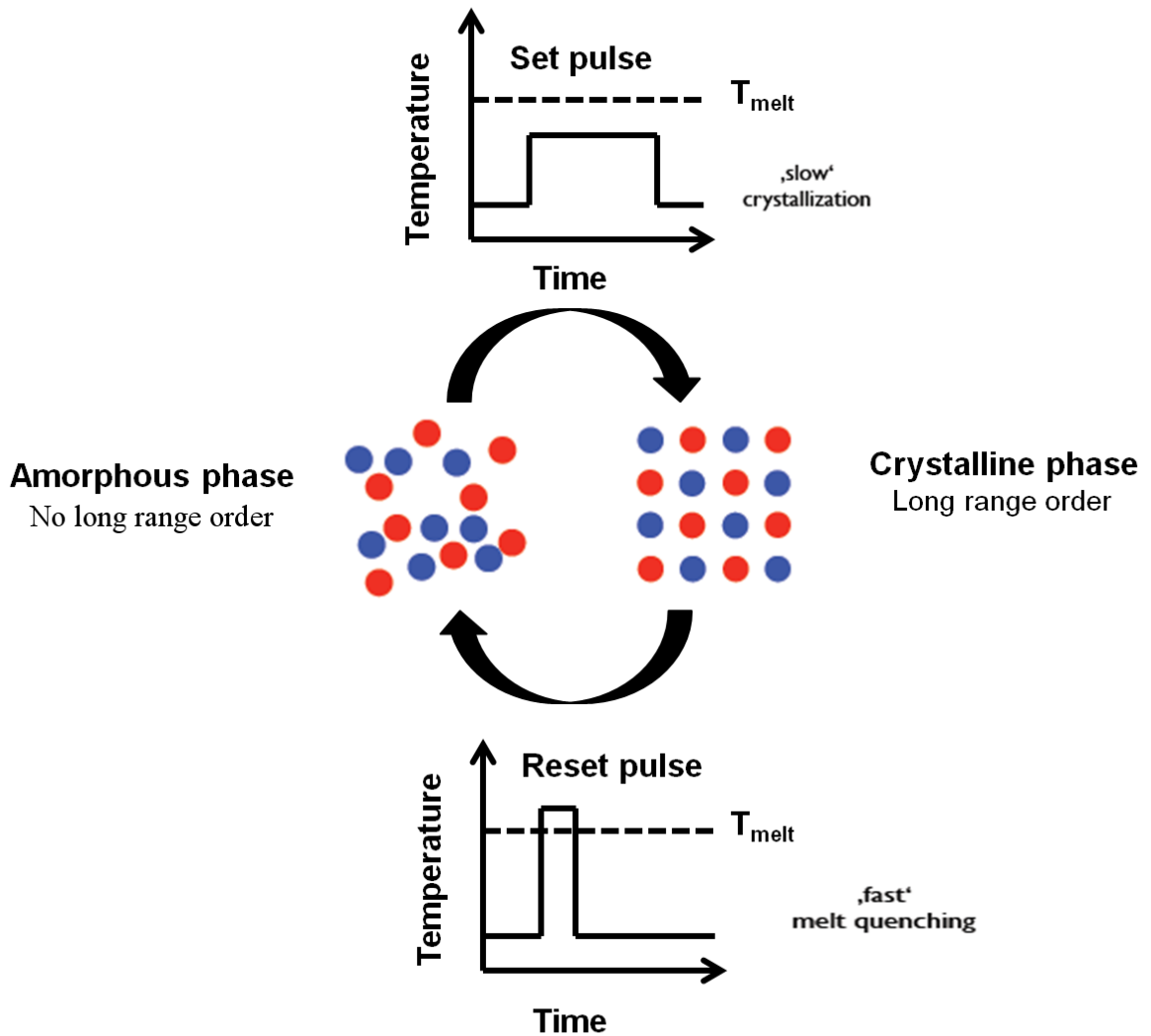
Figure 1.1: Sketch showing atomic configuration in different phases for a phase change material and the applied pulses to perform the phase transition. Slow cooling of the molten material allows ordering of the atoms in the energetically favourable crystalline phase. Fast quenching of the molten state "freezes" the liquid material into a disordered state.

at a temperature below the melting temperature. In the crystalline phase, the atoms are arranged in a periodic pattern, which leads to a metallic-like conduction mechanism [16]. The reverse operation (RESET-operation) is performed via melting-quenching, where the crystalline material is melted and quenched fast enough so that it solidifies in the amorphous state. The high amount of disorder in amorphous phase-change materials prohibits metallic conduction, but it creates a high amount of localized trap states.

The SET process is the data-rate limiting operation since it can take relatively long times for materials to crystallize. By contrast the RESET process has to be very fast, otherwise the material re-crystallizes during cooling. The melt-quenching in the RESET process is the power limiting operation since it requires more power to be delivered to heat the material above the melting temperature. For phase change materials this is typically between $800 - 1100$ K [17]. Read out of the information is performed by a lower amplitude optical or electrical pulse which measures the reflectivity in optical storage and the resistivity in electronic devices. These read pulses are too low amplitude to cause any phase change.

A set of material requirements has to be fulfilled by phase change materials to be useful for technological applications in the memory arena [18]. For instance, fast crystallization (ideally in nanosecond time scale) and very high stability of the amorphous phase against spontaneous crystallization (upon to 10 years) are required [19]. Furthermore, the material should have a relatively low melting temperature, a stable amorphous phase with high activation energy towards crystallization. For these reasons only very few phase change materials are suitable for technological applications.

## 1.3 Structural properties of phase change materials

In order to understand the function in phase change materials first it is necessary to consider their structure. Phase change materials used today can be classified in three main families: the Te-based eutectic alloys, the $GeTe - Sb_2Te_3$ pseudo-binary materials and the Sb eutectic alloys. Generally speaking phase change eutectic alloys have two prominent characteristics, a high melting temperature and a highly stable amorphous state at room temperature [20, 21], whereas pseudo-binary line $GeTe - Sb_2Te_3$ and doped
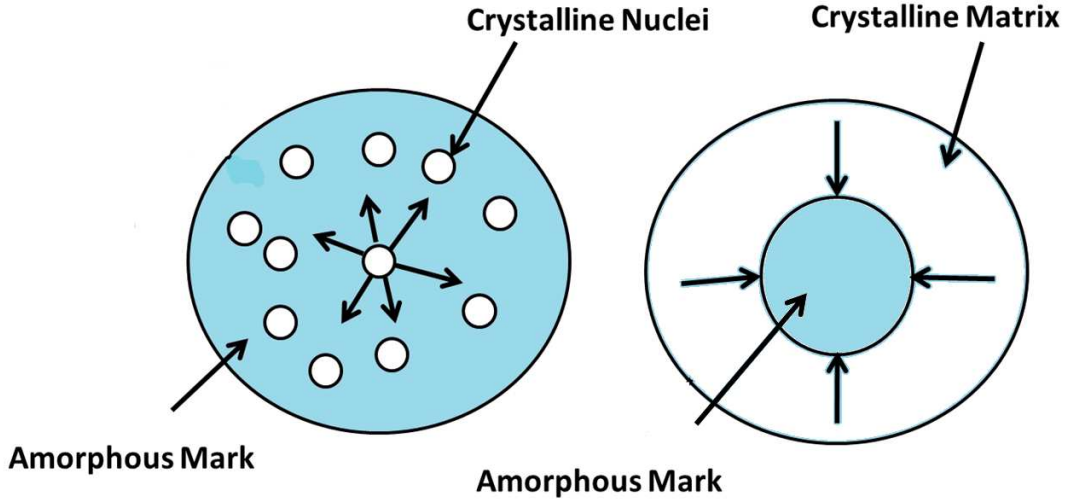
Figure 1.2: Schematic representation of the crystallization of an amorphous mark in a crystalline phase change layer of a material with: (a) "nucleation-dominated" mechanism and (b) with a "growth-dominated" mechanism.

$SbTe$ alloys show fast recrystallization and pronounced optical contrast [22, 23]. On the $GeTe - Sb_2Te_3$ pseudo-binary line, the best known composition is $Ge_2Sb_2Te_5$, which combines all the requirements of fast crystallization, stability of the amorphous phase and high contrast. The $GeTe - Sb_2Te_3$ family usually exhibit a nucleation-dominated crystallization mechanism, whereas the doped $SbTe$ family shows a growth-dominated mechanism. Figure 1.2 shows the difference between these two mechanisms.

In the following section the structural properties of some typical phase change materials are described in the crystalline, liquid and the amorphous phase. We will consider alloys that lie on the pseudo-binary line $GeTe - Sb_2Te_3$ since the well known $Ge_2Sb_2Te_5$ phase change material is going to be considered for the rest of the thesis.

## 1.3.1 Structural properties of the amorphous state

An amorphous material is defined as a material that lacks the long-rate translational and orientational order characteristics present in the ideal crystalline state [24]. Therefore

neither a unit cell, as given in the crystalline state, can be defined nor the atomic positions within such a unit cell. Amorphous materials are never truly random in a statistical sense. However, such material can exhibit several distinct types of marked, random structural correlations at various scales. These statistical properties classify the structure of amorphous solids and liquids by their short, medium and long range structural order [24].

1. **Short-range order**. This occurs in the $2 - 4$ Å length scale and is associated to the nearest-neighbour and next-nearest neighbor atomic correlations, which are determined by 2-body and 3-body correlations respectively.

2. **Medium-range order**. This range characterizes non-random structural correlations in a $4 - 10$ Å length scale. It corresponds to atom-atom correlations beyond the 2-body and 3-body correlations of the short range order.

3. **Long-range order**. Even when, by definition, amorphous materials do not show long range structure, they can exhibit some form of structural order at distances longer that 10 Å.

Amorphous materials are invariably thermodynamically metastable: they generally have a higher configurational entropy than the lowest free-energy state, the corresponding crystal. The main different methods of producing amorphous materials are: melt-quenched vitrification and vapour-phase amorphous-film deposition, which lead to different amorphous states. Generally speaking, vapour deposition leads to a more structurally disordered material than melt-quenching (because of the high rates of cooling needed for the latter [19]).

## 1.3.2 Structural properties of the crystalline state

The phase change materials such as $Ge_2Sb_2Te_5$, $Ge_1Sb_2Te_4$, $GeTe$ or $Sb_2Te_3$ not only exhibit an amorphous and crystalline structure, but also two different crystalline phases. The two different crystalline structures are the rocksalt and trigonal phase structures. The trigonal phase structure can be described as a slightly distorted rocksalt structure.

For example, the most simple binary composition GeTe alloy exhibits a rocksalt structure at high temperatures above 400 °C [25] whereas in the ground state at low temperatures it exhibits a trigonal structure. The rocksalt structure has not been observed in ternary alloys such as $Ge_2Sb_2Te_5$ and $Ge_1Sb_2Te_4$ as a high temperature phase in bulk samples, as it has been in $GeTe$ but only as a metastable phase in thin films [26].

Another important factor in the crystalline phase structure is the role of the vacancies which can be studied by *ab initio* calculations. Numerical results obtained for $Ge_1Sb_2Te_4$ and $Ge_2Sb_2Te_4$ with this method show the influence of differences in the vacancy concentration on the electronic properties [27]. The $Ge_1Sb_2Te_4$ and 25% ($GeSb_2Te_4$) $Ge_2Sb_2Te_4$ alloys are formed in a rocksalt structure which can be visualized as two interpenetrating cubic face centred (fcc) sublattices. Te occupies one fcc sublattice while Ge and Sb are distributed randomly on the other fcc sublattice with 25% ($GeSb_2Te_4$) or 20% ($GeSb_2Te_4$) vacancies.

Well-known phase change materials, such as $GeSbTe$, usually have an octahedral coordination, often accompanied by local distortions [23]. The origins of these characteristic structural arrangements are the bonding properties, which differ significantly from those of more conventional (e.g. Si) semiconductors. However, the structures also show that a rigid octahedral arrangement, which would result in a perfect rocksalt lattice is not stable [28].

In this section we have given a summary description of the current data storage available at present on the market and under research development, highlighting the remarkable features of phase change materials and memories. We have also given a brief description of the structural properties of the amorphous and crystalline phases.

## 1.4 Outline of the thesis

Now we have introduced the main properties of phase change materials, we turn our attention to the phase transformation between the two different structures. In Chapter 2, we briefly describe and confront several different approaches used to simulate the crystallization and amorphization in phase change materials. Firstly the most basic concept of nucleation and growth is introduced and definitions with their respective expressions

for the free energy, critical radius and critical energy barrier are given. Afterwards, the well known JMAK theory, rate and master equation methods are described, highlighting their strengths and limitations. The Cellular Automata approach introduced by Ashwin *et al* [29] is explained in detail. This approach will be used for the remainder of this thesis. A detailed comparison of the different approaches for phase transformations is also presented.

After exploring different approaches to model phase transitions, we discuss the electrical properties of phase change materials in Chapter 3. In this chapter, we present two different explanations of threshold switching previously introduced by Ielmini *et al* [30] and Karpov *et al* [31, 32]. These two different explanations of threshold switching are used for analytical comparison later on, in Chapter 7.

The Cellular Automata approach, in combination with an analytical model for threshold switching are integrated to realize physically realistic simulations of phase change memory devices in Chapter 4. All the details of the complete electro-thermal implementation in phase change random access memory (PCRAM) are presented. Direct correlation between the structural phases and their electrical states during the SET and RESET process is obtained.

In Chapter 5, we explore and study the energy accumulation regime for phase change materials in a continuous $Ge_2Sb_2Te_5$ thin film material. The results obtained in the continuous thin film material suggest that energy accumulation can be accomplished by a sequence of low amplitude excitation pulses. By using the accumulation property of phase change materials, we also design (in simulation) an accumulator response in a simple nanoscale phase change device that can provide a powerful form of arithmetic computing. We also show that this accumulation property can be used to provide a simple form of phase change integrate and fire "neuron".

The mechanisms for threshold switching presented in Chapter 3, can predict experimentally observed relaxation oscillations when phase change devices are subjected to voltages close to threshold switching. In chapter 6, we recall the threshold switching model introduced by Ielmini *et al* [30], and described in Chapter 3, and also introduce a circuit analysis model to explain these oscillations. We also obtain a simplified phe-

nomenological model of the $V - I$ characteristic curve that exhibits threshold switching and with this simplified model relaxation oscillations can also be obtained.

The two different explanations of threshold switching, given in Chapter 3, are used to understand the role of electric field induced crystallization in phase change materials in Chapter 7. First, a study in the a continuous $Ge_2Sb_2Te_5$ thin film material is performed to determine regions where the electric field may play a significant role in crystallization. Afterwards, a detailed comparison of two different explanations for threshold switching in a mushroom like cell (PCRAM cell) are compared and analyzed. Finally, in Chapter 8, overall conclusions are presented, along with suggestions for further work.

# Chapter 2

# Cellular automata approach for modelling phase change transformations in continuous thin films

There are several approaches to mathematical modelling of the crystallization and amorphization behaviour of phase change materials, such as (1) classic nucleation and growth theory, (2) JMAK theory and (3) rate and master equations. In this chapter, we present a review of these approaches and describe a Gillespie cellular automata (GCA) simulation approach previously introduced by Aswhin $et$ $al$ [29]. This GCA approach has the thermodynamic features of previous models (rate equation approach and phase field models) of crystallization and is potentially capable of spanning the scales from atomistic models and bulk-scale methods. Using the GCA simulator, we show the results of some annealings of $Ge_2Sb_2Te_5$ thin films, showing that the simulator can model nucleation and growth effects and spatio-temporal annealings. These results provide a useful test for the GCA code developed in this thesis. We also present a detailed summary on different approaches to modelling phase change transformations.

# 2.1 Classic nucleation and growth theory

The classical theory of steady state crystal nucleation was originally developed by Gibbs, Volmer, Weber, Becker, Döring, Turnbull and Fisher in 1926-1969 [19, 33, 34, 35]. The driving force for crystallization is the difference in Gibbs free energy of the amorphous solid (or liquid) and the crystalline phases. The crystallization of an amorphous solid is a three stage process [33, 34, 35]:

1. **Early (nucleation) stage**. In this stage the dominating process is nucleation, i.e there is a creation of a population of clusters of crystallites at nanoscopically small sizes. The crystallite cluster concentration is relatively low and clusters grow and decay in the model by gaining and losing monomers only. A monomer represents a single "molecule" of phase change material. For the remainder of the thesis we are going to use the $Ge_2Sb_2Te_5$ phase change alloy, in which case a monomer is a $Ge_2Sb_2Te_5$ "molecule".

2. **Advanced stage**. This stage is characterized by the continuation of grow by gaining monomers and losing monomers. In this stage many small clusters that are below the critical size will decay. As the cluster concentration becomes high the contacts between the clusters of different sizes becomes important in the cluster growth. Many of the initial monomers form part of the growing clusters causing a significant decrease of nucleation.

3. **Late (ageing) stage**. Throughout this stage, ageing of the newly formed phase occurs mainly by the decay of small clusters losing monomers that feed the growth of larger clusters. This process will end when the clusters reach a certain concentration ensuring the thermodynamic equilibrium of the system.

## 2.1.1 Homogeneous crystal nucleation

The basic concepts for nucleation theory were provided by Gibbs in 1878 [36]. This early treatment was purely thermodynamic and described cluster formation of a new phase inside the parent phase. Using this approach, the first kinetic model for nucleation

was proposed by Volmer and Weber in 1926 [37] and served as a basis for a further improvement by Becker and Döring in 1935 [38]. Finally, in 1949, Turnbull and Fisher obtained an expression for the pre-exponential factor of the nucleation rate in a condensed phase. Nowadays the so-called *classical nucleation theory* is due to Becker, Döring, Fisher, Turnbull, Volmer and Weber [33, 34, 35].

In the parent phase, atoms approach each other statistically, forming crystalline clusters by thermodynamic fluctuations. For simplicity, these clusters are assumed to be spherical with radius $r$. The equilibrium cluster distribution is given by Boltzmann statistics [39]:

$$N^{equ}(r) = N_0 \cdot \exp\left(-\frac{\Delta G_{cluster}(r)}{k_B T}\right), \qquad (2.1)$$

where $\Delta G_{cluster}(r)$ is the reversible work for crystal cluster formation, $k_B$ the Boltzmann constant, $T$ the absolute temperature, $N_0$ the total number of atoms in the parent phase and $N^{equ}(r)$ the number of clusters of radius $r$ at equilibrium. $\Delta G_{cluster}(r)$ can be expressed as a sum of two contributions:

$$\Delta G_{cluster}(r) = -\Delta g \cdot \frac{4}{3}\pi r^3 + 4\sigma\pi r^2, \qquad (2.2)$$

where $\Delta g$ the bulk free energy difference between the two phases and $\sigma$ the interfacial energy.

The typical evolution of the $\Delta G_{cluster}(r)$ is displayed in Figure 2.1 as a function of both the temperature and the radius of the cluster. The quantity $r_c$ is called the *critical radius*. A cluster of radius $r_c$ is called a critical cluster and $\Delta G_{cluster}(r)$ is *the critical work for cluster formation*. The work of formation of $\Delta G_{cluster}(r)$ increases for $r < r_c$. As a result, clusters of size smaller than the critical size are energetically not favorable and spontaneously decay. For $r > r_c$, clusters grow due to a gain in free energy. Therefore, $\Delta G_{cluster}(r)$ can be considered as an activation barrier against crystallization.

The curve in Figure 2.1 passes through a maximum, which can be obtained by solving

$$\frac{\partial \Delta G_{cluster}(r)}{\partial r} = 0 \qquad (2.3)$$
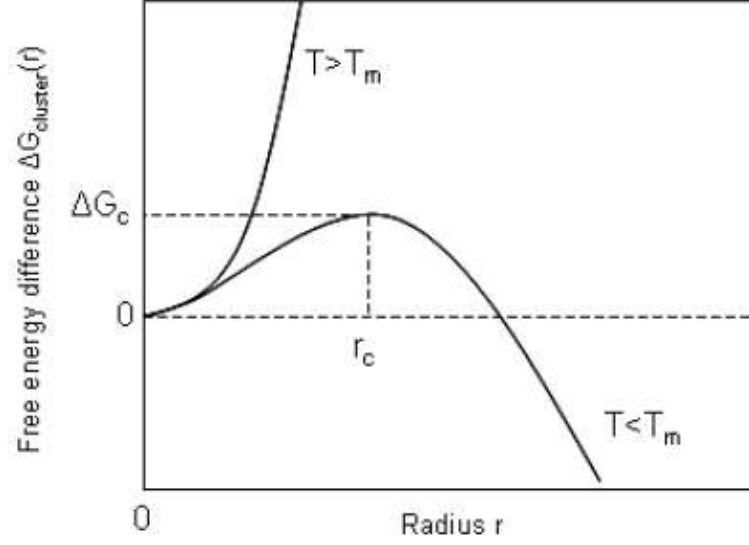
Figure 2.1: Free energy difference as a function of the temperature and the radius of the crystalline cluster. Here $T_m$ is the melting temperature, $\Delta G_c$ is the critical energy barrier for nucleation and $r_c$ is the critical radius. Taken from [40].

and the position of the maximum is therefore

$$r_c = \frac{2\sigma}{\Delta g}. \tag{2.4}$$

The critical value of $\Delta G_{cluster}(r)$ is, by (2.4) and (2.2):

$$\Delta G_{cluster}(r_c) = \frac{16\pi}{3} \frac{\sigma^3}{(\Delta g)^2}, \tag{2.5}$$

where $\Delta G_{cluster}(r_c)$ is defined as the critical energy barrier for nucleation.

The steady-state rate of nucleation of a $Ge_2Sb_2Te_5$ cluster (i.e. the number of newly formed nuclei per unit time and volume) is approximated by [41, 42], as:

$$I^{SS} = 4f(1)\gamma n_c^{2/3} Z \exp(-\frac{\Delta G_c}{k_B T}), \tag{2.6}$$

where $f(1)$ is the concentration of $Ge_2Sb_2Te_5$ molecules, and $Z$ is the Zeldovich factor, given in the expression

$$Z = \sqrt{\frac{\Delta g}{6\pi k_B T n_c}}, \tag{2.7}$$

with $\gamma$ the molecular jump frequency at the interface between the two phases. This attempt frequency, $\gamma$, can be approximated by the diffusional jump frequency of $Ge_2Sb_2Te_5$ molecules (D), according to

$$\gamma = \frac{D}{\lambda^2} \qquad (2.8)$$

where $D$ is the diffusion coefficient and $\lambda$ the atomic jump distance, which is assumed to be the same as the nearest-neighbour distance in $Ge_2Sb_2Te_5$ (2.99 Å) [43]. Based on the Stokes-Einstein relationship, the diffusion coefficient $D$ is related to the viscosity of $Ge_2Sb_2Te_5$ ($\eta$), by

$$D = \frac{k_B T}{3\pi\gamma\eta}. \qquad (2.9)$$

As data of the viscosity of $Ge_2Sb_2Te_5$ can rarely be found in the literature, it is possible to use published data on $Ge - Te$, for a first approximation, as follows:

$$\eta = 1.94 \times 10^{-14} \exp\left(\frac{2 \pm 0.10eV}{k_B T}\right) \qquad (2.10)$$

The values of the viscosity in a temperature range between 500 K and 900 K, according to equation (2.10) are in the range $\eta =$[2.7 $\times$ 10$^7$ 10.9 $\times$ 10$^{-3}$] Pa.s. However, recently Akola $et$ $al$ [44] calculated a viscosity value of 1.1 to 1.2 $\times$ 10$^{-3}$ Pa.s in a molecular-dynamics simulation of $Ge_2Sb_2Te_5$ at 900 K.

## 2.1.2   Crystal growth

After being nucleated, crystalline clusters above the critical size can grow to a macroscopic size by molecular attachment and detachment of molecules to and from the cluster. Crystal growth can be performed in two possible mechanisms: interface-controlled growth and diffusion-controlled growth. In the first one it is assumed that there is no change in the composition of the parent phase and the crystal cluster. Therefore, growth is controlled by the rearrangement of atoms moving only at the amorphous-crystalline interface, thus attaching to the stable crystal. In the second mechanism the stable crystal grows by gathering material that is rich in one of the components, which results in a long range diffusion. The crystallization process of $Ge_2Sb_2Te_5$ does not involve any

composition change which is why we are not going to discuss this growth mechanism here. In the interface-controlled growth mechanism, the rearrangement process may either require a diffusive jump in the case of diffusion-limited kinetics or an atomic collision in the case of collision-limited kinetics. In both cases, the rearrangement frequency is not dependent on the interface position, so the growth velocity $u$ is independent of time. Thus the crystal growth velocity is [45]:

$$u = \gamma_s \lambda \kappa \left[ 1 - \exp\left( -\frac{\Delta g(T)}{k_B T} \right) \right] \quad for \quad (T \leq T_m) \tag{2.11}$$

where $\gamma_s \in [0,1]$ is the fraction of sites where a new atom can be incorporated, $\lambda$ is the atomic jump distance and $\Delta g$ is the bulk free energy between the two phases per unit volume. The value of the rate constant $k$ for diffusion-limited crystallization according to Turnbull and Fisher is:

$$k = \frac{6D}{\lambda^2}, \tag{2.12}$$

For collision-limited crystallization, the collision rate at which atoms attempt to join the crystalline cluster is [19]:

$$k = \frac{u_{sound}}{\lambda}, \tag{2.13}$$

where $u_{sound}$ is the sound velocity in the liquid or the amorphous phase. The growth velocity $u$ in (2.11) at melting temperature $T_m$ is zero since $\Delta g(T) = 0$.

## 2.2 JMAK theory

The JMAK (Johnson-Mehl-Avrami-Kolmogorov) theory allows approximate calculation of the volume fraction of crystallized material, whereas classic nucleation theory provides a means to estimate the cluster nucleation and growth rates, and crystallite size distributions [46, 47, 48].

The kinetics of isothermal phase transformation proceeding via nucleation and subsequent growth are generally described by the JMAK theory according to

$$X(t) = 1 - \exp[-(kt)^n] \qquad (2.14)$$

where $t$ is time, $n$ is the Avrami coefficient, and $k$ is an effective rate constant. The Avrami coefficient is related to the dimensionality of the crystallization process. The effective rate constant describing the nucleation and growth rates is generally given by an Arrhenius equation

$$k(T) = \nu \exp\left(-\frac{E_A}{k_B T}\right) \qquad (2.15)$$

where $\nu$ is a frequency factor, $E_A$ is the activation energy, $T$ is the absolute temperature, and $k_B$ is the Boltzmann constant.

It should be noted that JMAK theory is based on some key assumptions [49], which unfortunately are often violated in a real system. The main assumptions for JMAK theory are:

1. Nucleation takes place randomly and uniformly.

2. The nucleation rate is independent of time.

3. The growth rate is independent of cluster size.

4. Growth is dominated by interface controlled mechanism.

Some of these assumptions are not always fulfilled in real systems. Firstly nucleation can occur on surfaces, at interfaces, and impurities, known as heterogeneous nucleation [50, 51]. There is experimental evidence showing that the interface layer between a substrate and the $Ge_2Sb_2Te_5$ layer is where crystallization starts. The influence of the heterogeneous nucleation taking place at the substrate has been investigated by Ohshima in [50]. Secondly, there is an incubation time that exists before the onset of the crystallization process, which determines that the nucleation rate can not be considered to be time independent over the entire crystallization process [52]. There is also experimental evidence of the existence of non-negligible incubation time during the

crystallization of the $Ge_2Sb_2Te_5$ [52, 53] . Therefore, the use of JMAK equation (2.15) it is not appropriate for the description of phase transformations in real phase change memories [54].

## 2.3 Rate and master equation approaches

During nucleation in a real system, there will not only be a distribution of clusters of critical size, but also a distribution of clusters of different sizes. The interaction existing between these clusters determines the progress of the crystallization process [49]. Postulating that cluster growth and decay takes place only by monomer attachment and detachment from the clusters, as in the Szilard model of nucleation [33], the cluster can change size only by the nearest-size transitions. Possible interactions that a cluster of $n$ $Ge_2Sb_2Te_5$ monomers can have are then

$$[Z_1] + [Z_n] \longleftrightarrow [Z_{n+1}], \qquad (2.16)$$
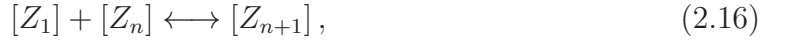
where $[Z_1]$ and $[Z_n]$ are the "chemical" formulae of the monomers and the $n$-sized clusters respectively.

According to this scheme, a continuous kinetic rate equation describing the concentration $Z(\mathbf{n}, t)$, of the clusters of size $\mathbf{n}$ is given by:

$$\frac{d}{dt} Z(n,t) = g(n-1,t)Z(n-1,t) - d(n,t)Z(n,t) - g(n,t)Z(n,t) + d(n+1,t)Z(n+1,t),$$
$$(2.17)$$

for $n \geq 2$, where $g(n,t)$ and $d(n,t)$ are the growth and dissolution rate respectively of a cluster of size $n$. In order to solve such a rate equation given by equation (2.17), the growth and dissolution rates need to be determined, by reaction rate theory [55]

$$g(n,t) = 4\pi r^2 \lambda Z(1,t)\gamma \exp\left(-\frac{\Delta G_{n \longrightarrow n+1}}{2k_B T}\right) \qquad (2.18)$$

$$d(n+1,t) = 4\pi r^2 \lambda Z(1,t)\gamma \exp\left(-\frac{\Delta G_{n+1 \longrightarrow n}}{2k_B T}\right), \qquad (2.19)$$

where $Z(1,t)$ is the concentration of $Ge_2Sb_2Te_5$ monomers at a given time, $r$ is the cluster radius, $\gamma$ is the molecular jump frequency at the interface between amorphous and crystalline phases, and $\lambda$ is the jump distance. In [49] the energy terms in the Boltzmann factors are defined as the free energy differences between sizes $n$ and $n+1$ such that

$$\Delta G_{n \to n+1} = \Delta G(n+1, t) - \Delta G(n, t), \tag{2.20}$$

where $\Delta G$ is the free energy required to form the new phase. This free energy can be described according to Turnbull and Fisher using the Becker-Döring formalism [33, 34, 35] as

$$\Delta G = 4\pi r^2 \sigma - n\Delta g, \tag{2.21}$$

where $\sigma$ is the interfacial energy density between amorphous and crystalline phases and $r$ is the cluster radius. The shape of the clusters is assumed spherical, such that the relation between cluster radius and number $(n)$ of GST molecules (monomers) in the clusters is

$$n = \frac{4}{3}\pi \frac{r^3}{v_m}, \tag{2.22}$$

where $v_m$ is the volume of a monomer ($v_m = 2.9 \times 10^{-22}$ cm³ for $Ge_2Sb_2Te_5$). The parameter $\Delta g$ in (2.21) is the bulk free energy difference per GST molecule between the two phases, which can be calculated with the approximation proposed by [56] as

$$\frac{\Delta g}{v_m} = \Delta H_f \frac{T_m - T}{T_m} \left[ \frac{7T}{T_m + 6T} \right], \tag{2.23}$$

where $T_m$ is the melting temperature of $Ge_2Sb_2Te_5$ and $\Delta H_f$ is the enthalpy of fusion at melting point. The value of $\Delta H_f = 625$ J/cm³ was estimated in [49] using data obtained from differential scanning calorimetry experiments in [57, 58].

Expressions for the critical values $n_c$ and $\Delta G$ can be obtained with the aid of (2.21). In the particular case of spherical nuclei, these are given by

$$n_c = \frac{32\pi}{3} \frac{v_m^2}{\Delta g^3} \tag{2.24}$$

$$\Delta G_c = \frac{16\pi}{3} \frac{v_m^2 \sigma^3}{\Delta g^2}. \tag{2.25}$$

Solution of the set of equations given by (2.17) yields the size distribution function of crystalline clusters of $Ge_2Sb_2Te_5$ at any given time during the phase-transformation process. A typical solution is shown in Figure 2.2, where the density of clusters as a function of cluster size $n$ is plotted (taken from [49]). It should be mentioned that Figure 2.2 shows the steady-state distribution, which is the solution after a long annealing time when the cluster sizes distribution takes a constant value (steady-state value). It can be seen that a very high concentration of small clusters exist, with fewer larger clusters whose concentration decreases in an exponential fashion as cluster size increases. Calculations in [49] assumed that the available material for crystallization is continuously depleted, which is the result of the conservation of matter. The monomer concentration is calculated according to

$$Z(1,t) = Z(1,0) - \sum_{2}^{n_{max}} Z(n,t)dn,$$

where Z(1,0) is the initial concentration of $Ge_2Sb_2Te_5$ monomers. The number of rate equations $n_{max}$ used during calculations in [49] varies between $10^4$ and $10^7$.

The prediction of the crystallized fraction based on such a rate equation model was proven to be in a good agreement with experimental results for a variety of sample types and a range of heating regimes, as shown in Figure 2.3 (taken from [49]). The crystallized fraction is found by integrating $Z(n)$ from $Z(n = 2)$ to $Z(n = n_{max})$. The use of the rate equation provides a way to simulate the process of the nucleation and growth simultaneously, and can also include transient effects (e.g. non steady-steady nucleation/growth rate). However, rate equation theory introduces a very large number of coupled differential equations into the model. As a result, when such a model is used to simulate the phase change process in real-life memory devices, there is a trade off between computational complexity and available computer resources. This is due to the series of rate equations that are required for each calculation point due to the temperature within a memory device changing spatially. As a result, the rate-equation method is not suitable for situations where it is necessary or desirable to simulate spatial variations in crystallization.

It should be noted that the rate equation (2.17) can be given in the form of a continuity equation, or more precisely, an analogue of equation (2.17) with a continuous $n$
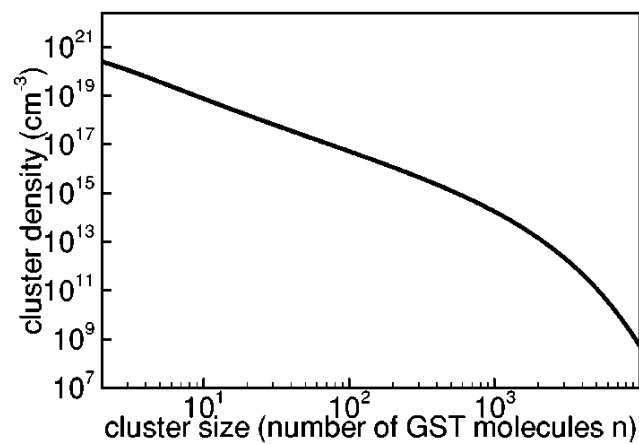
Figure 2.2: Size distribution function of crystalline clusters for $Ge_2Sb_2Te_5$ for describing density as a function of cluster size. Taken from [49]. It should be mentioned that the annealing time for this plot is long enough to reach the steady state, when the cluster size distribution takes on a constant value.

.
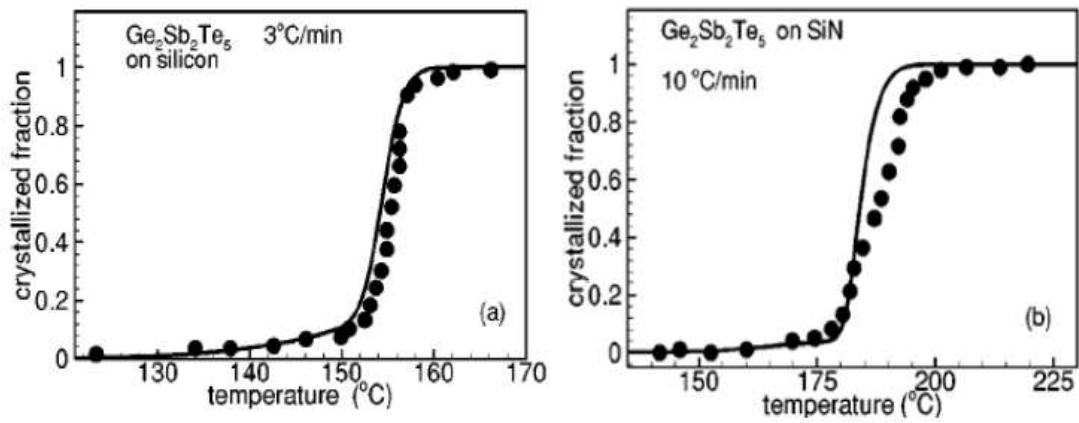
Figure 2.3: Taken from [49], experimental (dots) and calculated (lines) results showing crystallized fraction of $Ge_2Sb_2Te_5$ as a function of temperature during ramped anneals for (a) $Ge_2Sb_2Te_5$ on silicon for 3 °C/min ramp rate and (b) $Ge_2Sb_2Te_5$ on SiN for 3 °C/min ramp rate.

term. Here, we consider the transformation of (2.17) into a partial differential equation of Fokker-Planck type, as outlined by Zeldovich [33]. One of the main problems in the transformation of (2.17) is the determination of the two transition frequencies $d(n,t)$ and $g(n,t)$. The determination of the detachment frequency $d$ can be very complicated since it depends on parameters characterising the cluster rather than the new phase. Therefore, it is advantageous to eliminate the detachment frequency in equation (2.17).

Following [33], let us approximate $g(n-1,t)Z(n-1,t)$ and $d(n+1,t)Z(n+1)$ by a truncated Taylor expansion around the point $n$:

$$g(n-1,t)Z(n-1,t) = g(n,t)Z(n,t) + \left\{ \frac{\partial}{\partial n}[g(n,t)Z(n,t)] \right\} [(n-1)-n]$$

$$+ \frac{1}{2}\left\{ \frac{\partial^2}{\partial n^2}[g(n,t)Z(n,t)] \right\} [(n-1)-n]^2, \quad (2.26)$$

$$d(n+1,t)Z(n+1,t) = d(n,t)Z(n,t) + \left\{ \frac{\partial}{\partial n}[d(n,t)Z(n,t)] \right\} [(n-1)-n]$$

$$+ \frac{1}{2}\left\{ \frac{\partial^2}{\partial n^2}[d(n,t)Z(n,t)] \right\} [(n-1)-n]^2. \quad (2.27)$$

Replacing the first and the fourth terms in (2.17) by the right-hand sides of equations (2.26), (2.27) leads to

$$\frac{\partial}{\partial t}Z(n,t) = -\frac{\partial}{\partial n}\left( [g(n,t)-d(n,t)]Z(n,t) - \frac{1}{2}\frac{\partial}{\partial n}[g(n,t)+d(n,t)]Z(n,t) \right). \quad (2.28)$$

The problem with equation (2.28) is that we must know the two frequencies $g(n,t)$ and $d(n,t)$ in order to be able to solve it. To find the dependence of $n,t$ of the attachment frequency $g(n,t)$ is straightforward since the attachment of a molecule to a given cluster depends, above all, on the state of the old phase. On the contrary, the detachment of a molecule from a cluster depends on the cluster properties, which are poorly known, since the cluster is a new phase. Moreover, the detachment frequency $d(n,t)$ can be calculated

using transition state theory which relies on the constrained equilibrium hypothesis [35]. The calculated detachment frequency will depend on the molecular jump frequency at the interface between the amorphous in a similar manner as in (2.19) and this jump frequency is taken as that governing bulk diffusion in (2.8). Since the structure near the interface and the parent phase are likely do be different, this assumption is questionable. In addition, the jump frequency should be dependent on cluster size. That is why it is convenient to eliminate the the detachment frequencies from the description. The reduction of $d$ is done following Zeldovich as in [33]. First, let us define the function $C(n,t)$, the equilibrium cluster size distribution, with the help of the equality

$$g(n,t)C(n,t) - d(n+1,t)C(n+1,t) = 0. \tag{2.29}$$

This function, $C(n,t)$, is used to exclude the $d(n,t)$ and $d(n+1,t)$ terms from (2.17). The resulting equation containing $C(n,t)$ instead of $d(n,t)$ is [59, 33]

$$\frac{d}{dt}Z(n,t) = g(n-1,t)C(n-1,t)\left[\frac{Z(n-1,t)}{C(n-1,t)} - \frac{Z(n,t)}{C(n,t)}\right]$$

$$-g(n,t)C(n,t)\left[\frac{Z(n,t)}{C(n,t)} - \frac{Z(n+1,t)}{C(n+1,t)}\right]. \tag{2.30}$$

Using the following truncated Taylor expansion

$$\frac{Z(n+1,t)}{C(n+1,t)} = Z(n,t)/C(n,t) + \left[\frac{\partial}{\partial n}[Z(n,t)/C(n,t)]\right][(n+1) - n] \tag{2.31}$$

twice, it is possible to replace the first and the second finite differences in (2.30) by the partial derivatives $-\partial[Z(n-1,t)/C(n-1,t)]/\partial n$ and $-\partial[Z(n,t)/C(n,t)]/\partial n$, respectively. The resulting finite difference is then represented as a derivative with the help of the Taylor expansion

$$g(n-1,t)C(n-1,t)\frac{\partial}{\partial n}[Z(n-1,t)/C(n-1,t)]$$

$$= g(n,t)C(n,t)\frac{\partial}{\partial n}[Z(n,t)/C(n,t)]$$

$$+ \frac{\partial}{\partial n}\left[g(n,t)C(n,t)\frac{\partial}{\partial n}[Z(n,t)/C(n,t)]\right][(n-1)-n] \quad (2.32)$$

Therefore, by replacing (2.31) into (2.30) and then substituting (2.32), the so-called master equation of nucleation was obtained [33]:

$$\frac{\partial}{\partial t}Z(n,t) = \frac{\partial}{\partial n}\left\{g(n,t)C(n,t)\frac{\partial}{\partial n}[Z(n,t)/C(n,t)]\right\}, \quad (2.33)$$

which is the analogue of (2.17) and (2.28) and which describes the kinetics of the process when $n$ is taken as a continuous variable.

Next we describe a slight variation of (2.33) as presented in [60]. This different formulation of (2.33) assumes a continuous distribution of clusters of sizes $n \geq 2$ while retaining a separate scalar for the monomer ($n = 1$) concentration. The dynamics are determined by the temporal evolution of a cluster size distribution function. Rate equations are used to obtain the frequencies of attachment and detachment of monomers.

A set of continuous (2.34) or discrete (2.17) equations are closed by applying appropriate boundary conditions at $n = 2$ and $n = \infty$ and then using an integral to incorporate the exhaustion of monomer. This makes it possible to examine the effect of monomer exhaustion that is critical in the dynamics of the cluster distribution.

In this master equation approach, the crystallization process is characterized by a time-dependent cluster size density $Z(n, \mathbf{x}, t)$ which denotes the probability that at time $t$ the point $x$ is a part of a size $n$ cluster of crystallized material [60]. We consider, as in [60, 61], a continuum of $n \geq 2$ and set

$$Z_m = Z(1, \mathbf{x}, t)$$

to be the density of monomer. The proportion of crystallized material in some sample (or size large compared to crystal size) is defined as the ratio of monomers that are in

size $n$ clusters ($n \geq 2$) to the total monomers in that sample. The relationship between this definition of crystallinity and material properties such as reflectivity or electrical conductance is not necessarily linear or simple [62].

The temporal dynamics of $Z(n, \mathbf{x}, t)$ for $n \geq 2$ and $Z_m$ is governed by the master equation which describes the kinetics of a crystallization process.

The master equation for evolution of the cluster size density $Z(n, \mathbf{x}, t)$ is

$$\frac{\partial}{\partial t} Z(n, \mathbf{x}, t) = \frac{\partial}{\partial n} \left\{ f(n, T, Z_m(\mathbf{x}, t)) C(n, T) \frac{\partial}{\partial n} \left[ \frac{Z(n, \mathbf{x}, t)}{C(n, T)} \right] \right\} \qquad (2.34)$$

for $n \geq 2$, which is a time and space-dependent version of the master equation derived by Zeldovich for isothermal nucleation at constant supersaturation [60]. In (2.34 $f(n, T, Z_m(\mathbf{x}, t))$ is the frequency of monomer attachment to an $n$-sized cluster at temperature $T$ which also depends on the concentration of the available monomer $Z_m(\mathbf{x}, t)$. The function $C(n, T)$ can be defined using the general approach by Zeldovich [33] and equation (2.29). Moreover, $C(n, T)$ is the quasi equilibrium cluster size distribution, and the spatial dynamics of the cluster size distribution function $Z$ is driven by spatial variations in $f$ and $C$, which are in turn determined by variations in $T$. The total density of the crystalline material is then expressed as

$$\int_{n=2}^{\infty} n Z(n, \mathbf{x}, t) dn,$$

and is assumed to remain finite at all times. The density of monomer $Z_m$ is determined by conservation of the material as

$$Z_m(\mathbf{x}, \mathbf{t}) = Z_0 - \int_2^{\infty} n Z(n, \mathbf{x}, t) dn, \qquad (2.35)$$

where $Z_0$ is the total density of the material.

The boundary conditions for the master equation (2.34) require, for large $n$,

$$\lim_{n \to \infty} Z(n) \to 0,$$

to maintain a bounded total density of crystal cluster sizes [60].

In Figure 2.4(a) it is shown several initial iterations of the master equation for $T = 140$ $^oC$ (taken from [60]). This figure suggests that the monomers start forming clusters at an early stage, which subsequently grow into the clusters of larger sizes. Later, the
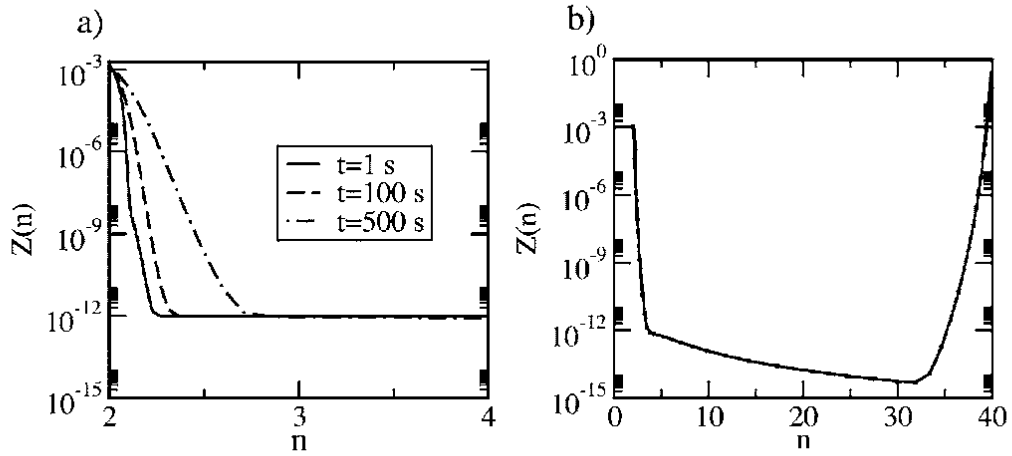
Figure 2.4: Numerical solutions of the master equation (2.34).(a) Initial iterations for T = 140 °C; (b) Final cluster size distribution profile for T = 140 °C the final profile is determined by the exhaustion of monomer. Taken from [60].

original pool of monomers is being exhausted, and a redistribution of cluster sizes takes place with larger clusters gaining further monomers and smaller clusters losing them. Eventually the system settles on the distribution shown in Figure 2.4(b) (taken from [60]).

One of the advantages of the master equation technique is the fast prediction of cluster size distributions from the thermodynamics of the crystallizing material. In addition, some insight into the dynamics of crystallization can be gained from the analytical solution of the master equation in particular cases.

## 2.4 General characteristics of cellular automata approaches

Phase change processes have been studied and modelled in the past using the well-known Johnson-Mehl-Avrami-Kolmogorov model (JMAK). The JMAK model attempts to find the fraction of the crystallized material at every given point in time. This model assumes

that the nucleation occurs randomly and uniformly, and the nucleation rate is time independent [28, 63, 33, 29]. The validity of the assumptions in JMAK was investigated. Experimental evidence has demonstrated that some important assumptions are violated: for example nucleation takes place mainly on the boundary between the material and the substrates. This model does not show the incubation time preceding the onset of crystallization [28, 63, 30, 29]. Another disadvantage of this model is that it cannot give information about the distribution of the clusters sizes. This means that the JMAK will not distinguish materials with the same crystallized fraction but different crystallite size distributions. This is an important factor to predict the dynamical progress of the complex spatio-temporal anneals which are necessary for memory applications [33, 29].

Another way of modeling phase change is based on separable nucleation and growth models [28, 33, 29, 19]. These approaches only consider clusters above the critical size, but sub-critical clusters have been seen to play an important role in the nanoscale dynamic behaviour. The rate-equation approach models the evolution of the crystal cluster size distribution during the whole process [33, 29, 19]. However this approach is computationally intensive and not suited to cases like electrical memories in which understanding the spatial distribution of crystallization is desirable [33, 19].

Recently, ab-initio atomic-scale models of crystallization processes in phase change materials have been developed based on Density Functional Theory [64, 33, 19]. These models take huge computational power to simulate only a few hundred of atoms, making such approaches, while useful for fundamental studies, unsuitable to predict the operation of real devices.

In the next section, we review a Gillespie-Cellular automata modelling approach [29], which is capable of spanning the scales between atomistic methods, such as DFT, and bulk scale methods like JMAK theory. The model has the thermodynamic features of the rate equation approach with elements from probabilistic cellular automata (PCA) models [65] and phase-field models [66]. Furthermore, due to the speed of the Gillespie algorithm used for the time-stepping it is possible to simulate complex spatial and temporal annealing (cooling/heating) cycles of the operation in realistic models of phase change memory devices.

## 2.5   Description of a Gillespie cellular automata approach

Now we introduce the GCA model from [29]. In this model a homogeneous, isotropic material on a square lattice is considered. The state of the material is defined on the discrete regular lattice of points. Each site of the lattice is assumed crystalline or amorphous. Each grid $(i, j) \in G$, is described by the quantities:

   a)  $r_{ij}$ is defined as the phase, which can be amorphous (0) or crystalline (1).

   b) $\phi_{ij}$ is an "orientation" variable which ranges from 0 to $2\pi$. The orientation mimics the many possible orientations that a crystal can form.

   Two neighbouring sites $(i, j)$ and $(k, l)$  are in the same crystal if

$$r_{ij} = r_{kl} = 1 \quad \text{and} \quad \phi_{ij} = \phi_{kl}$$

The temporal evolution is based on a stochastic model, which provides an estimate of rates of the possible local changes to the state of the system employing a Gillespie algorithm [67, 68, 29].

In the Gillespie cellular automata approach the following events in each site $(i, j)$ are possible:

**Nucleation:** A site $(i, j)$ and an adjacent amorphous site change from amorphous to a single crystal at a rate $C_{ij}^{nu}$.

**Growth:** A site in amorphous state becomes crystalline and part of an adjacent crystal of orientation $\Psi$ with rate $C_{ij}^{gr}$.

**Dissociation:** A site which is originally crystalline it is removed from the crystal of which it was part and becomes amorphous at rate $C_{ij}^{di}$ and assumes a new random orientation.

At each site $(i, j)$ in the domain the set of rate coefficients for nucleation, growth and dissociation (defined as $C_{ij}^{nu}$,$C_{ij}^{gr}$,$C_{ij}^{di}$) are approximated by the change in bulk and surface energies of crystallites adjacent to that site. It should mentioned that the terms attachment and dissociation here are in the context of celullar automata, meaning that there is nor real movement of the molecules and there is only a change on the crystalline

phase of the site. For each site $(i, j)$ the set of neighbours is defined as: $N_{ij} = \{(k, l) \in G$ is a neighbour of $(i, j)\}$ and $n_{ij} = |N_{ij}^{am}|$.

The set of amorphous neighbours of $(i, j)$ is defined as:

$$N_{ij}^{am} = \{(k, l) \in N_{ij} : r_{kl} = 0\} \quad and \quad n_{ij}^{am} = |N_{ij}^{am}|, \tag{2.36}$$

and for the set of neighbours of $(i, j)$ with a given orientation $\Psi$ by:

$$N_{ij\Psi}^{or} = \{(k, l) \in N_{ij} : \phi_{kl} = \Psi, r_{kl} = 1\}, \quad and \quad n_{ij\Psi}^{or} = |N_{ij\Psi}^{or}|. \tag{2.37}$$

The rates for these events are analogous to those obtained in the master equation rates in [49].

Possible "interactions" (which represent the molecular collisions), are assumed to occur at a temperature dependent rate

$$R(T) = k_0 e^{-\frac{E_a}{k_B T}} \tag{2.38}$$

where $E_a$ is the activation energy and $k_B$ is the Boltzmann constant and $k_0$ is a fitting parameter.

Overall, it is possible to define the rate coefficients for nucleation as

$$C_{ij}^{nu} = \begin{cases} k_0 \exp\left(-\frac{E_a}{k_B T}\right) \frac{n_{ij}^{am}}{n_{ij}} \xi(T, S_m) & \text{if } r_{ij} = 0 \\ 0 & \text{if } r_{ij} = 1 \end{cases} \tag{2.39}$$

where:

$$\xi(T, A) = \{\text{rate at which a site transforms from amorphous to crystalline}\}, \tag{2.40}$$

and where $T$ represents the temperature and $A$ is the surface area change. Thermal equilibrium is assumed, meaning the rate of the inverse transformation is $\xi^{-1}(T, A)$. The rate in (2.40) varies with temperature in a similar way to the rate equations in [49] as the bulk and the energy surface vary. The change in the surface area of the crystallites is computed by adding a site $(i, j)$ to a neighbouring crystal of orientation $\Psi$ using the linear approximation

$$A = S_m \left[ \frac{n_{ij} - 2n_{ij\Psi}^{or}}{n_{ij}} \right], \tag{2.41}$$

where $S_m$ the surface of a single site.

The growth rate for an amorphous site to join a crystalline neighbour with orientation $\Psi$ is:

$$C_{ij}^{gr} = \begin{cases} k_0 \exp\left(-\frac{E_a}{k_B T}\right) \xi(T, S_m \frac{n_{ij}-2n_{ij\Psi}^{or}}{n_{ij}}) & \text{if } r_{ij} = 0, \\ 0 & \text{if } r_{ij} = 1 \end{cases} \tag{2.42}$$

and the rate for a crystalline site to become amorphous is:

$$C_{ij\Psi}^{di} = \begin{cases} 0 & \text{if } r_{ij} = 0 \\ k_0 \exp\left(-\frac{E_a}{k_B T}\right) \xi(T, S_m \frac{n_{ij}-2n_{ij\Psi}^{or}}{n_{ij}})^{-1} & \text{if } r_{ij} = 1. \end{cases} \tag{2.43}$$

Let $T_m$ be the melting temperature: assuming the free energy change associated with the crystallization of a single site varies linearly with $T - T_m$ and the energy change associated with the change in surface $A$ is $\sigma A$ with $\sigma$ as a constant, then

$$\xi(T, A) = \exp\left[ L \left(1 - \frac{T}{T_m}\right) - \frac{\sigma A}{k_B T_m} \right], \tag{2.44}$$

where, as in [67], the parameter $L$ is defined as

$$L = \frac{\Delta H_f v_m}{2 k_B T_m}.$$

For the simulations in the rest of the thesis we use the constants for the thermodynamics and kinetic parameters as in Table 2.1.

## 2.6    Simulation of phase change processes in continuous thin films

In the following subsections (2.6.1 and 2.6.2), the phase change processes of $Ge_2 Sb_2 Te_5$ "bulk" material, are simulated. By a "bulk" material, we mean continuous thin films of

| Symbol | Parameter | Value | Unit |
|:---:|:---:|:---:|:---:|
| $\sigma$ | interfacial energy | $10^{-5}$ | J/cm$^2$ |
| $s_m$ | molecular surface area | $21.187 \times 10^{-14}$ | cm$^2$ |
| $E_a$ | activation energy | $2.1$ | eV |
| $k_0$ | molecular jump frequency | $10^{16}$ | $\mu$s$^{-1}$ |
| $\Delta H_f$ | enthalpy of fusion | $625$ | J/cm$^3$ |
| $v_m$ | volume of a GST monomer | $2.9^{-22}$ | cm$^3$ |
| $T_m$ | melting temperature | $889$ | K |

Table 2.1: Numerical values for the thermodynamic and kinetic parameters used in this section. See [49, 29].

material as opposed to device-like configurations. The results obtained in the section aim to reproduce the simulations for case of nucleation and crystal growth and the case of spatio-temporal annealings, obtained in [61]. The results of this section are also a test for our Gillespie Cellular Automata code. We used the same parameters and temperatures to those used in [61]. The $Ge_2Sb_2Te_5$ phase change material has a fine balance between bulk and surface energies of crystals, meaning that one can find nontrivial nucleation and growth dynamics that vary with $T$. The following simulations are performed in a 2-dimensional grid $N^2$ with $N = 256$. The crystalline fraction $\chi$ for this grid can be calculated as $\chi = \frac{1}{N^2} \sum_{i,j} r_{ij}$ where $0 \leq \chi \leq 1$. The fully crystalline state corresponds to $\chi = 1$.

## 2.6.1 Nucleation and crystal growth

When phase-change materials are subject to high temperatures there is a competition between growth and dissociation. This can be observed in Figure 2.5 which shows annealing at different stages for a sample subjected to a relatively high temperature T = 407 ºC. The crystallization time is shorter for high temperatures than for low temperatures, as it has been suggested in [69, 70] and as we will show later in this thesis in Figures 7.1, 7.2 and 7.3 (Section 7.2). There are still processes of detachment and
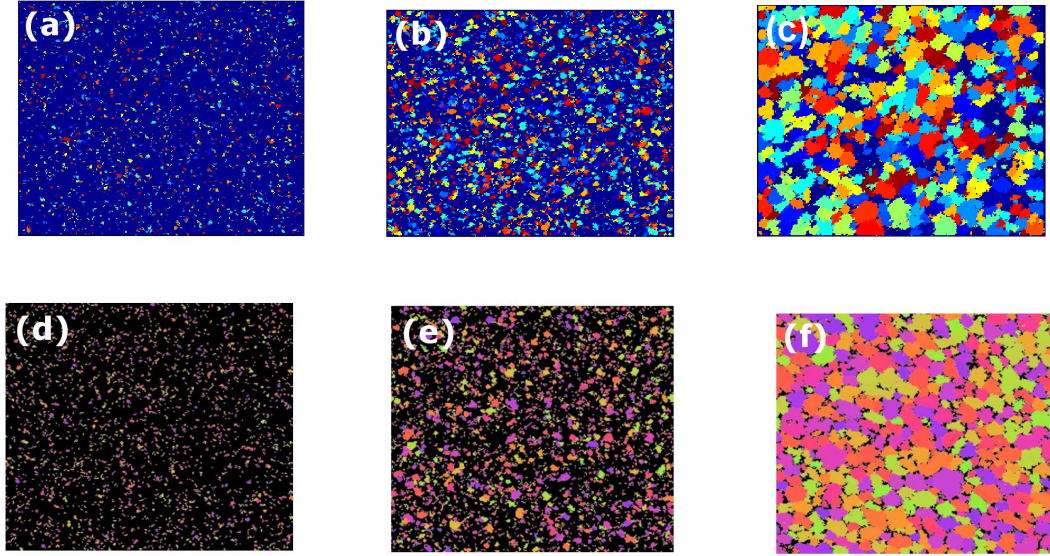
Figure 2.5: Grain structure of $Ge_2Sb_2Te_5$ held at temperature T = 407 ℃. The figures at the top ((a)-(c)) were obtained with our code and the time is (a) 140.51 ns (b) 650 ns and (c) 4.3474 $\mu$s. In the bottom figures the time is (d) 145 ns (e) 679 ns (f) 4.347 $\mu$s. A few nucleated crystals grow while other smaller crystals decay, since there is a non-trivial nucleation size at this temperature. Observe the large crystal size due to this high temperature. Numerical values used are as in Table 2.1. The simulation was performed in a 2D grid with $256 \times 256$ monomers. The results obtained here aim to reproduce a similar nucleation and crystal growth case obtained in [61], using the same parameters and conditions. These results are also used to test our Gillespie Cellular Automata code.

reattachment of sites from crystals showing some fluctuations in the crystal fraction, as shown more clearly in Figure 2.6.

## 2.6.2   Spatio-temporal annealings

In phase change devices, the transitions between crystalline and amorphous structures occur with a temperature that depends on time and space. With the GCA algorithm it is possible to simulate such spatio-temporal annealings. For example, Figure 2.7 shows the simulated crystal structure for a $Ge_2Sb_2Te_5$ film held at T = 207 ℃ on the left
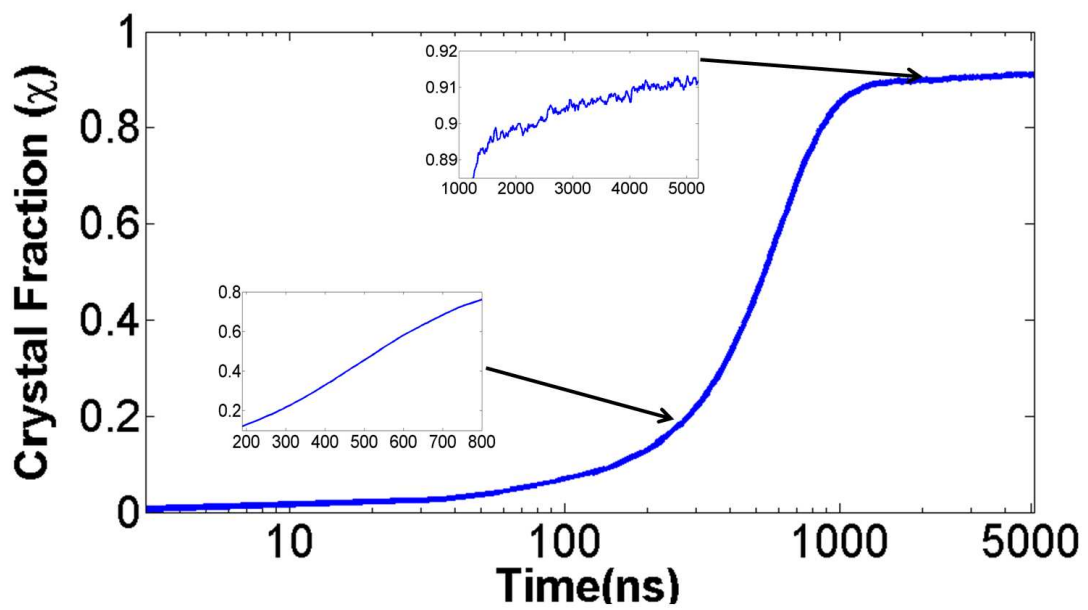
Figure 2.6: Crystal fraction $\chi$ as function of time for $Ge_2Sb_2Te_5$, starting as amorphous and annealed at T = 407 °C. We also show detail of the progress of the anneal near saturation and during the growth. Numerical values as in Table 2.1.

boundary, and T = 477 °C on the right boundary. This case aims to reproduce a similar spatio-temporal annealing obtained in [61], thus providing a useful test for the GCA code developed in this thesis. In Figure 2.7 it is seen that in left hand side the crystallization is slow compared to the right side and that at the right there is a dissociation process due to the high temperatures (near melting temperature). Therefore, in Figure 2.7 we see that the crystallization is faster in the intermediate region near the right boundary.

The crystal fraction evolution of this spatio-temporal anneal is depicted in Figure 2.8.

## 2.7 Comparison of different models for phase change transformations

An overview different approaches to modelling phase transformations have been described in this chapter, where the chalcogenide material used was the $Ge_2Sb_2Te_5$ phase change alloy. Recently ab-initio atomic-scale models of crystallization process have been also developed based on the well-known Density Functional Theory [64, 19]. Tables 2.2 and 2.3 briefly summarize these different approaches, noting their strengths and limitations.
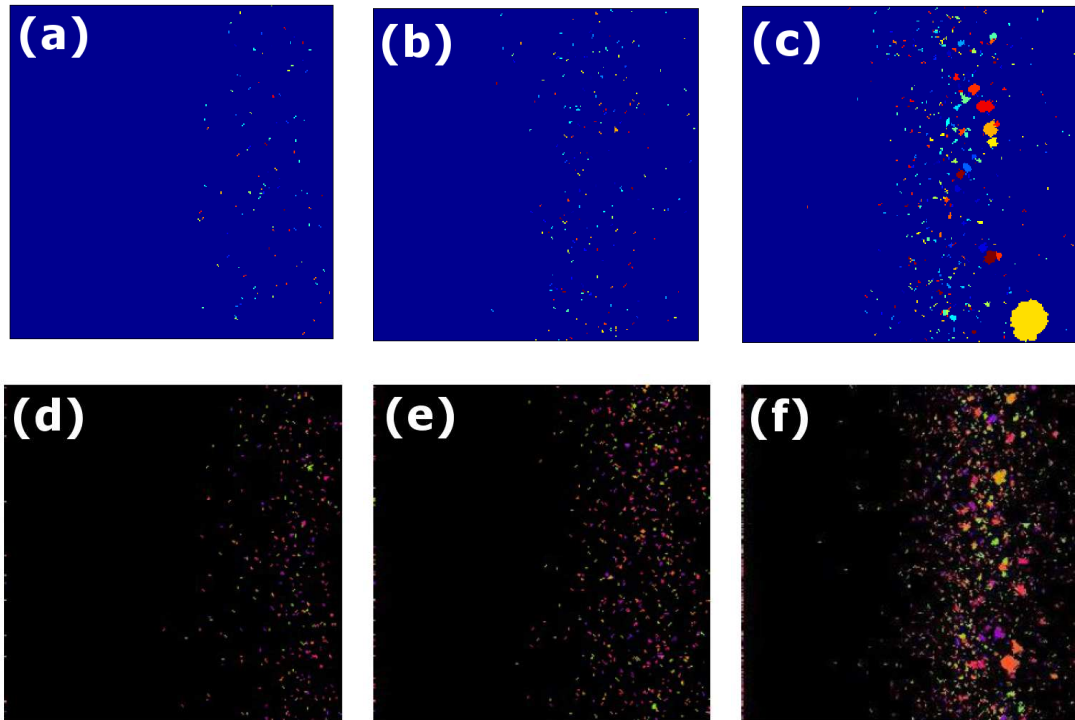
Figure 2.7: Images showing the crystal phase evolution for $Ge_2Sb_2Te_5$ held at T = 207 °C on the left boundary and T = 477 °C on the right boundary. Observe that as time progresses a band of higher crystallinity appears. In this band the size of the crystals is larger on the right side of the sample. The figures at the top ((a)-(c)) were obtained with our code and the time is (a) 19 ns (b) 75 ns and (c) 570 ns. In the bottom figures the time is (d) 17.6 ns (e) 70 ns (f) 554 ns. Numerical values as in Table 2.1. The results obtained here aim to reproduce a similar nucleation and crystal growth case obtained in [61], using the same parameters and conditions. These results are also used to test our Gillespie Cellular Automata code.
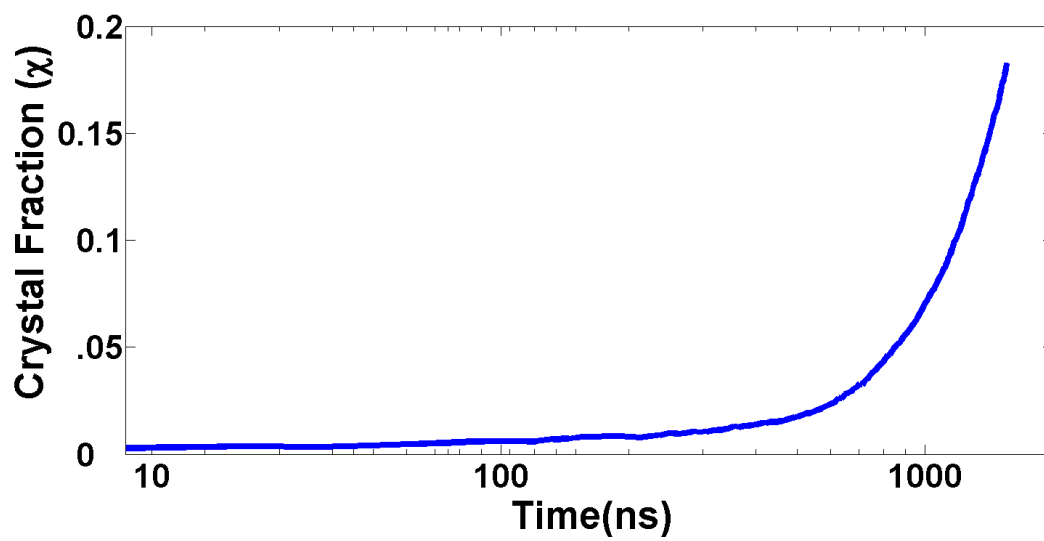
Figure 2.8: Crystal fraction $\chi$ as a function of time for $Ge_2Sb_2Te_5$ starting as amorphous and annealed at T = 207 ºC on the left boundary and T = 477 ºC on the right boundary. Numerical values as in Table 2.1.

| Modelling approach | Models growth | Spatio-temporal anneals | Speed of simulation | Dimension of the sample for reasonable computational time |
|---|---|---|---|---|
| JMAK (Section 2.2) | *Ad hoc* assumptions on the activation energy [51] | Limited | Very fast due to its simplicity | Unlimited |
| Nucleation and Growth (Section 2.1) | Yes, illustrated in [49] | Yes | Faster than Master Equation | $10^4 - 10^7$ monomers [49, 60] |
| Rate/Master Equation (Section 2.3) | By attachment and detachment of molecules | Requires coupled heat eq. | Slow if include spatial derivatives, and very stiff | $10^4 - 10^7$ monomers [49, 60] |
| Phase field | Yes, illustrated in [71] | Yes, as in [72] | Slower than nucleation and growth | $10^4 - 10^5$ monomers [73, 74] |
| Ab-initio | Yes as in [75] | No | Extremely slow | Hundreds of monomers [75] |
| GCA (Section 2.4) | By attachment and detachment of molecules | Illustrated in Section 2.6.3 and [29] | Very fast | $10^4 - 10^7 monomers$ |

Table 2.2: Summary remarks on different approaches to modelling phase change transformations.

This page is intentionally left blank.

| Modelling approach | Models melting | Incubation time | Anisotropy | Suitability for modelling PCRAM |
|---|---|---|---|---|
| JMAK (Section 2.2) | No | Negligible from experimental result in [52, 51] | Extension incorporating anisotropic growth [76] | Fully and easy to implement |
| Nucleation and Growth (Section 2.1) | Yes | No | Uses spherical cap model [45] | Fully, as in [77] |
| Rate/Master Equation (Section 2.3) | No | Yes as illustrate in [49] | Uses spherical cap model [45] | Feasible [60] |
| Phase field | Yes as in [72] | No | Yes as in [78] | Computational limited |
| Ab-initio | Yes | Yes as in [75] | Yes | Unfeasible |
| GCA (Section 2.4) | Yes | Illustrated in Section 2.6.1 | Crystals independent on orientation [60] | Fully as in [79, 70] |

Table 2.3: Continuation on the summary remarks on different approaches to modelling phase change transformations.

# Chapter 3

# Threshold switching in phase change materials

In 1968, Stanford Ovshinsky published a paper [80] describing: "a rapid and reversible transition between a highly resistive and a conductive state effected by an electric field which we have observed in various types of disordered materials, particularly amorphous semiconductors". In that paper, a sudden decrease in the dynamic resistance when the applied voltage exceeds a threshold voltage $V_{TH}$ was observed. Ovshinsky also announced that "an unusual memory effect is observed in materials in which structural changes are facilitated by removal of cross link elements", which is the basis of phase change memory. The publication generated a rapid response from the research community and industrial research laboratories where researchers reported threshold switching in many amorphous chalcogenide materials. The threshold switching effect has been the topic of investigation for the last decades, and different explanations have been proposed.

This chapter is a review of some of the possible threshold mechanisms, focusing on the electronically driven model developed by Ielmini [30] and the non-electronic alternative explanation by Karpov [32]. In Section 3.2, we will briefly describe the electrical properties of the crystalline phase and the electrical phenomena for the amorphous phase. In the amorphous phase two different behaviours can be distinguished: subthreshold conduction and threshold conduction. These conduction regimes are described using a model developed by Ielmini [30] and in which threshold switching is an electronically-driven

process. Finally in Section 3.3, an alternative non-electronic explanation for threshold switching, based on field-induced nucleation, is introduced.

## 3.1 Possible threshold switching mechanisms

Before describing the different models, we first describe the phenomenology of the threshold switching effect. In Figure 3.1 it is shown the $I - V$ characteristic curve of a chalcogenide alloy amorphous semiconductor (taken from [81]). In Figure 3.1 it is observed that for low applied voltage the device has ohmic behaviour. As the device voltage is increased the device current starts to increase linearly, until the threshold voltage, $V_{TH}$, is reached, where the device switches from a low conductive state ("OFF") to a high conductive state ("ON"). The device will remain in the "ON" state as long as sufficient minimum current $I_h$ is applied. If the current is reduced below the value $I_h$ the device will switch back to the "OFF" state. In Figure 3.1 the $I - V$ characteristic curve clearly shows S-type negative differential resistance.

Threshold switching was originally attributed to the thermal breakdown in the amorphous film [82, 83]. Under this assumption, a high voltage applied to the phase change material results in both current density and temperature increase due to the Joule heating effect, thus enhancing the electrical conductivity in the amorphous phase. If the phase change material is heated sufficiently, a huge thermal generation of electrical carriers occurs. As a result, the high current density can be sustained with a moderate voltage drop across the phase change material. The appearance of this thermal model can be understood since thermal runaway in semiconductors generate an S-type negative differential resistance curve. In the following years several purely electronic switching models appeared [81] such as: the double injection model proposed by Henisch [84], the charge controlled model by Haberland [81] and the model of Adler [85]. In 1978, Adler *et al* [85] proposed an analytical electronic switching model where the threshold switching effect is the result of a high field carrier generation process that leads to trap filling and saturation of the carrier recombination process. In the Adler's model an S-type negative differential resistance was obtained and recovery of both threshold voltage and resistance in the "OFF" state were explained in terms of the carrier diffusion of the conduction
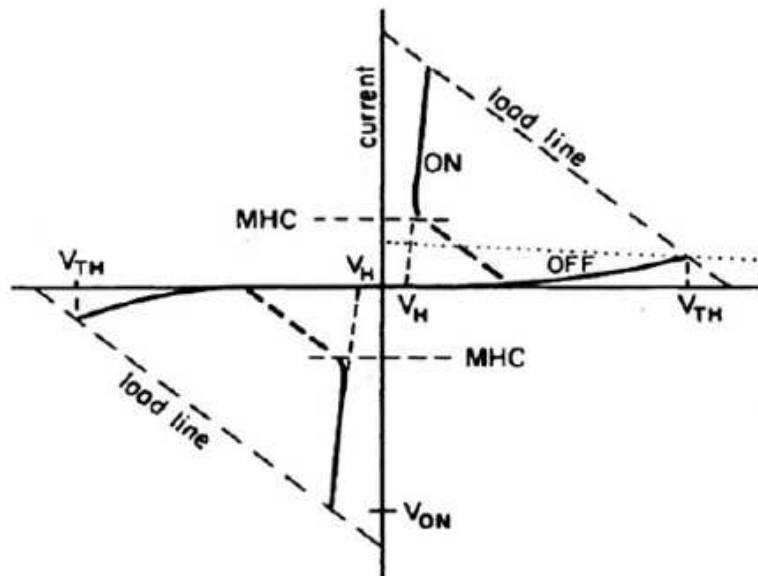
Figure 3.1: Schematic $I-V$ characteristic curve of the threshold switching phenomenon. In the figure $V_{TH}$ is the threshold voltage, $VH$ is the minimum "holding voltage" to sustain the "ON" state and $MHC$ is the correspondent minimum hold current. Taken from [81].

filament. The Adler model was also able to successfully predict measured results [86].

Recently, the first modern threshold switching model was presented by Radielli *et al* [87] assuming low field conductivity controlled by a Fermi level pinned at mid-gap by the valence alternating pair defects used in the model proposed by Adler. In 2006, a slight variation of the original Adler model was presented by Fritzsche [88]. The model calls upon the presence of valence alternating pairs to explain the low field behaviour in the amorphous state and explains the threshold switching effect by the Zener breakdown. Another threshold model related to the Redaelli, Adler and Fritzsche models was proposed in 2008 by Ielmini [30]. In the Ielmini model, the connection between sub-threshold conduction and threshold switching is based on a electron heating process in which carriers tunnel under high field between traps in the semiconductor gap. Similar to the model by Redaelli *et al* [87], the Ielmini model does not explicitly assume current filament formation, and the S-type negative differential resistivity occurs from homogeneous current flow in the device. In section 3.2, we present a complete description of Ielmini's model.

An alternative non-electronic model for threshold switching was recently proposed by Karpov [32]. The Karpov model is based on a structural transition that occurs under a field-induced nucleation and growth of a needle shape conductive filament in the host insulating amorphous phase. The model can explain the statistical distribution of switching times, temperature dependence phenomena observed in chalcogenides, and measurements of relaxation oscillations observed in phase change devices. In section 3.3, we present a complete description of the Karpov model.

## 3.2   An analytical model for electronically-driven threshold switching

In this section, we review Ielmini's analytical model for threshold switching [30] based on trap-limited transport theory. A brief introduction into the conduction mechanism in semiconductor devices is given below to gain more insight into this conduction mechanism. It should be emphasized that the mechanism behind threshold switching is still

debated [87, 89, 90].

The Figure 3.2 shows schematic band diagrams for a typical chalcogenide semiconductor in both the crystalline and the amorphous phase. There are some notable differences in the band diagrams. First, the energy gap for the amorphous phase is large compared to the crystalline phase. Second, while the forbidden gap and conduction/valence bands are clearly distinct in the crystalline phase, the amorphous phase is characterized by a large concentration of localized states in the gap [91]. Third, due to the large concentration of localized states, the Fermi level is pinned at about midgap in the amorphous chalcogenide, which results in both electrical resistivity and its correspondence activation energy being relatively large.

### 3.2.1   Subthreshold conduction

To study the conduction mechanism in the amorphous phase, first the subthreshold characteristic is considered. Figure 3.3 shows measured $I - V$ curve for a PCRAM cell in the amorphous (reset) state at different temperatures in the range 25-85 ºC. The PCRAM cell exhibits a linear behaviour at relatively low voltages, while an exponential regime is observed at higher voltages.

In addition, the activation energy for conduction decreases for increasing applied voltage, as observed in materials where conduction is controlled by trapped carriers [93]. This can be observed in Figure 3.4 where the activation energy for conduction is extracted from an Arrhenius plot of the current as a function of $1/kT$ [30].

The Arrhenius plot in Figure 3.4 is consistent with the Poole−Frenkel model for conduction shown in Figure 3.5. It is assumed that the current is due to a Poole-Frenkel (PF) transport of electrons through traps, located at distance $\Delta z$ from each other. In the Poole-Frenkel model conduction is caused by thermal emission of carriers from one trap to conduction band, and then acceptance by another trap. Therefore, the energy barrier for electron transport with no applied voltage is $\Delta\Phi(0) = E_C - E_T$ (where $E_T$ and $E_C$ are the energy levels for donor-like traps and the conduction band, respectively). The potential barrier that needs to be overcome is decreased in the same direction as the electrostatic force along with increasing the applied voltage. Therefore, the forward
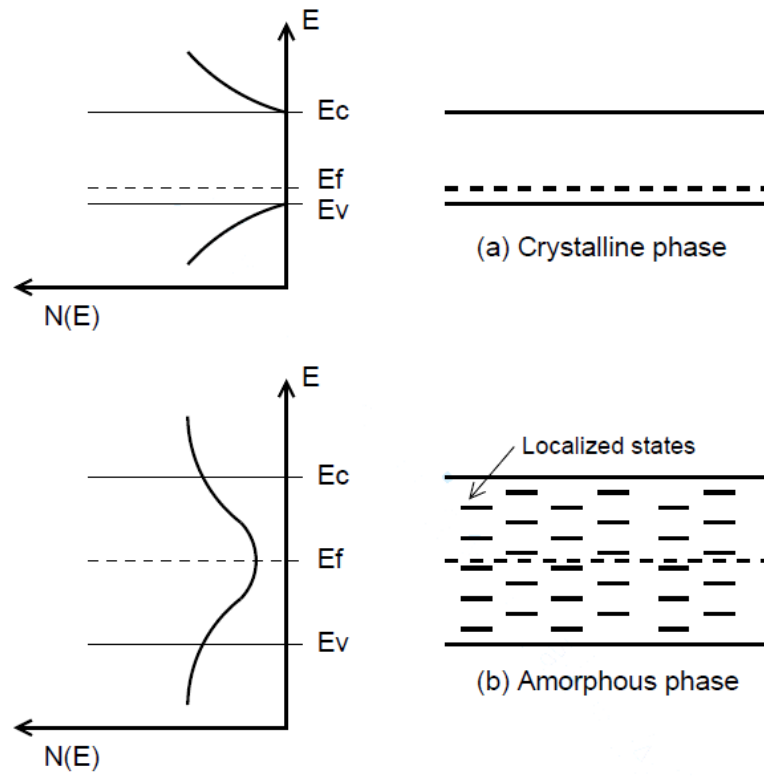
Figure 3.2: Schematic band diagrams for typical chalcogenide semiconductors in the crystalline and the amorphous phases. There are three important differences between the two diagrams: First, generally the energy gap for the amorphous phase is large compared to the crystalline phase. Second, while the forbidden gap and conduction/valence bands are clearly distinct in the crystalline phase, the amorphous phase is characterized by a large concentration of localized states in the gap [91]. The third difference regards the position of the Fermi level: due to the large concentration of localized states, the Fermi level is pinned at about midgap in the amorphous chalcogenide [92]. Taken from [28].
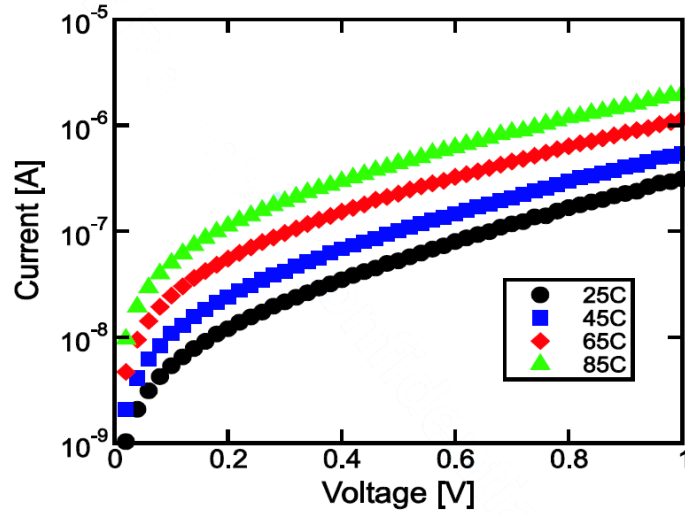
Figure 3.3: Measured $I - V$ curves for a $Ge_2Sb_2Te_5$ phase change cell in the amorphous state, subjected to increasing temperatures T = 25, 45, 65, 85 °C. The voltage is kept under the threshold switching voltage to preserve the initially programmed cell state. The measured current strongly increases with increasing temperature. Taken from [30].
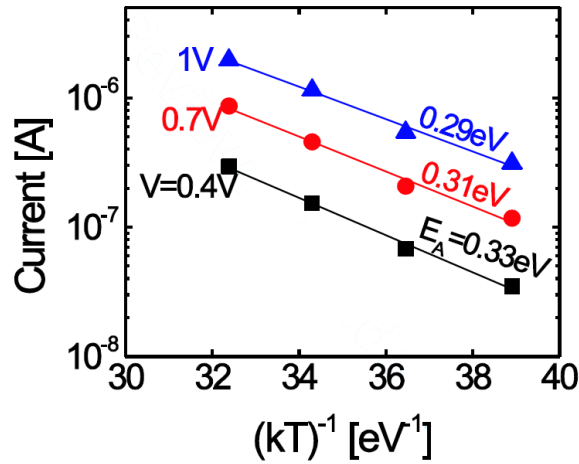


Figure 3.4: Measured current in an Arrhenius plot for various voltages (V = 0.4, 0.7 and 1 V) applied to a $Ge_2Sb_2Te_5$ PCRAM cell in the amorphous phase. The activation energy for conduction can be obtained as the slope of data in the Arrhenius plot. Taken from [30].
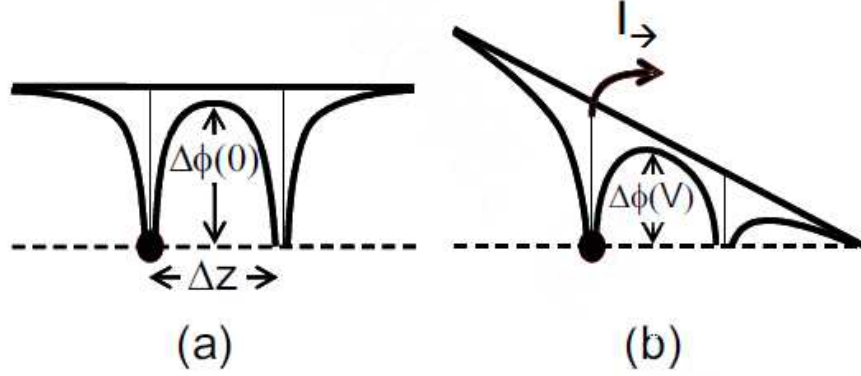
Figure 3.5: Scheme for the conduction mechanism in $Ge_2Sb_2Te_5$ as described by Ielmini in [30]. Here the current is due to (a) donor-type trapped electron subjected to a potential barrier $\Delta\Phi(0)$ at zero voltage. In (b) the potential barrier decreases as the voltage $V$ is applied, enhancing electron transport in the direction of the electrostatic force. The parameter $\Delta z$ represents the inter-trapping distance. Taken from [30].

current $I_\rightarrow$ due to the thermal emission is given by [30]:

$$I_\rightarrow = qAN_T\frac{\Delta z}{\tau_0}\exp\left(\frac{-(E_C - E_T - qV_A\Delta z/2u_a)}{kT}\right),$$ 

(3.1)

where $q$ is the unit charge $A$ is the area of contact of the active volume in the PCRAM cell, $n_T$ is the concentration of trapped carriers at $E_T$, $\tau_0$ is the attempt to escape time of the electron, $E_C$ is the mobility edge at the conduction band, $u_a$ is the thickness of the amorphous layer, and $N_T$ is the trap concentration, defined by:

$$N_T = n_T\exp([E_T - E_F]/kT)$$

where $E_F$ is the Fermi energy.

In a similar form, the reverse current is expressed in [30] as

$$I_\leftarrow = qAN_T\frac{\Delta z}{\tau_0}\exp\left(\frac{E_C - E_T - qV_A\Delta z/2u_a}{kT}\right)$$

(3.2)

Therefore the total current can be calculated from the difference between $I_\rightarrow$ and $I_\leftarrow$, yielding

$$I = 2qAN_T \frac{\Delta z}{\tau 0} e^{-\frac{E_C - E_F}{kT}} \sinh\left(\frac{qV_A}{kT}\frac{\Delta z}{u_a}\right), \tag{3.3}$$

where the sinh function is the result of the difference between the two exponential terms in (3.1) and (3.2).

## 3.2.2 Threshold conduction

The so called *threshold switching* phenomenon is clearly seen in Figure 3.6. Threshold switching results in a negative-differential-resistance (NDR) behaviour: increasing the voltage in the sub-threshold region, an unstable point ($V_{TH}$) is reached, corresponding to the transition from a positive differential resistance (the subthreshold regime) to the NDR region. In a real experiment, the current suddenly jumps to the next available stable positive-differential-resistance state, that is the ON state. In the ON state, the current is typically so large that the amorphous chalcogenide is quickly crystallized.

Following similar arguments from the subthreshold model it is possible to extend the previous model to describe the physics of threshold switching. For low voltages, the current is assumed to be due to PF transport under equilibrium energy distribution of electrons. For relatively high voltages the trapped electrons at or below the Fermi level can access empty trap states close to the conduction band at high energy levels, resulting in the movement from the equilibrium distribution to a nonequilibrium distribution of carriers. However it should be pointed out that a finite distance from the cathode-chalcogenide interface is required for electrons to jump into high energy states. This mechanism is schematically shown in Figure 3.7. Within a critical $u_{a,OFF}$ from the cathode interface, electrons are still in their equilibrium state. Empty traps are efficiently occupied only above $u_{a,OFF}$ , with a thickness of $u_{a,ON} = u_a - u_{a,OFF}$. Observe that the distance $u_{a,OFF}$ is inversely proportional to the applied electric field, which results in the appearance of threshold switching above a certain electric field (known as the threshold field). Due to current continuity requirements, the strong differences between conductivities in the ON and OFF layers result in a strong electric field nonuniformity, as shown in Figure 3.7. Under the OFF state of conduction (Figure 3.7(a)) the trap filling obeys the equilibrium condition, hence the electric field and conductivity are uniform
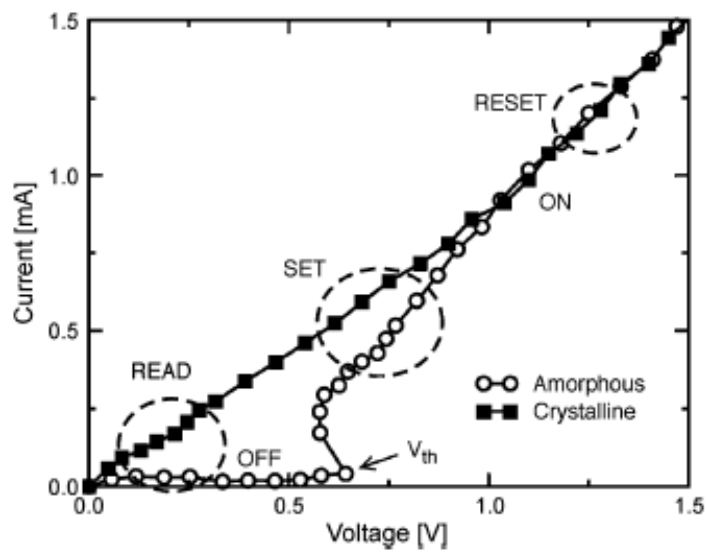
Figure 3.6: Measured $I - V$ characteristic for a PCRAM cell in the SET and RESET state.  When the threshold voltage $V_{th}$ is reached, a dramatic drop in voltage (and increase of current) is observed. Afterwards, current and voltage continue increasing to the ON state. Taken from [94].

(a)                                            (b)
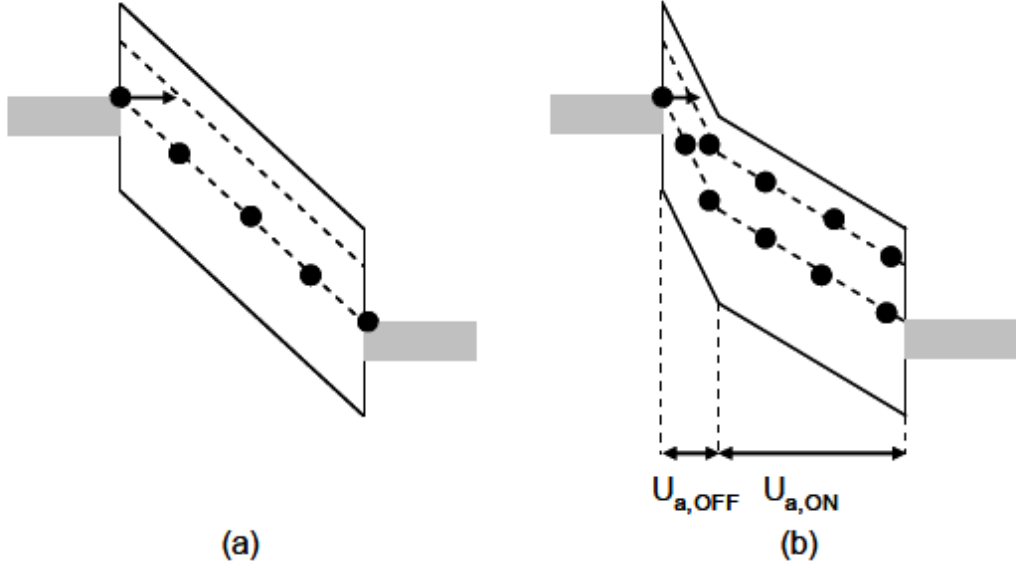
Figure 3.7: Schematic of the potential profile and energy distribution of electrons in the amorphous chalcogenide film. (a) under low field and (b) high field regimes in the amorphous chalcogenide. Here $u_{a,OFF}$ is the layer in the "OFF" conductive state and $u_{a,ON}$ is the layer in the "ON" state. In the high field regime the electrons occupy shallow trap states the "ON" layer with thickness $u_{a,ON}$. An equilibrium distribution of electrons is featured in the "OFF" layer. Taken from [95].

all over the amorphous layer. In Figure 3.7(b) observe that when the conductivity is switched to ON regime (above the critical threshold condition), the energy distribution of electrons will turn into nonequilibrium within the ON layer thickness $u_{a,ON}$ [30].

The collapse of the field in the ON region results in the negative differential resistance (NDR) effect, which turns into the "snap back" along the $I - V$ curve shown in Figure 3.6. Hence, the current in the threshold switching regime is calculated [30] according to:

$$I = 2qA(N_{T1})\frac{\Delta z}{\tau 0}e^{-\frac{E_C - E_F}{kT}}\sinh\left(\frac{qV_A}{kT}\frac{\Delta z}{u_a}\right)(1 + \gamma), \tag{3.4}$$

with $N_{T1}$ the concentration of the deep traps at energy level $E_{T1}$ aligned with the Fermi level, and $\gamma$ is the nonequilibrium term on the "ON" layer, as in [30]

$$\gamma = \frac{N_{T1}}{N_{T1} + N_{T2}}\frac{\tau_n}{\tau_0}e^{-B_{12}u_a/V_A}e^{-(E_{T1} - E_{T2})/kT}, \tag{3.5}$$

where $\tau_n$ is the effective relaxation of the electrons from shallow to deep traps, $N_{T2}$ is the concentration of the shallow traps at energy $E_{T2}$, and the constant $B_{12}$ is defined by:

$$B_{12} = \frac{4(2m)^{1/2}(E_{T2} - E_{T1})^{3/2}}{3q\hbar}, \tag{3.6}$$

with $m$ the effective mass of the electron and $\hbar$ is the Planck constant. Based on the systems of (3.4) to (3.6) the current in the threshold switching regime can be calculated. It should be pointed out (3.4) can describe the behaviour of the current in the subthreshold regime when $\gamma = 0$ and in the threshold regime with $\gamma > 1$.

In Figure 3.8 is a comparison between the measured and calculated $I - V$ curves for a $Ge_2Sb_2Te_5$ phase change cell in different programmed states. The calculated $I - V$ characteristic used the analytical model mentioned above (eqs. (3.3), (3.4) and (3.5)). The reset states were obtained using pulses with amplitude $V = 3.2$, 3.5 and 5 V to the cell, which result in three different final volumes of the amorphous phase. The different amorphous volumes are modelled by three different thickness values for $u_a$, corresponding to $u_a = 19$, 27 and 38 nm [30].

The calculated $I - V$ characteristic curve reproduces the resistance, subthreshold slope and threshold voltage in good agreement with the experimental data. Moreover this model accounts for the measured temperature dependence, the dependence of subthreshold slope on the thickness of the amorphous phase and the voltage dependence of the activation energy. Therefore, this analytical model seems to provide physically-realistic simulations of phase change cells under different voltages, temperatures and programming states. Furthermore, the model is computationally efficient (simple and fast). Hence, this model has been used extensively in this thesis for simulating the electrical behaviour of phase change materials and devices.

## 3.3 Electric field induced nucleation

An alternative explanation for threshold switching based on field-induced crystal nucleation has recently been suggested by Karpov et al. [31, 96, 97]. In this explanation, switching will start with the nucleation of a particle that increases locally the electric
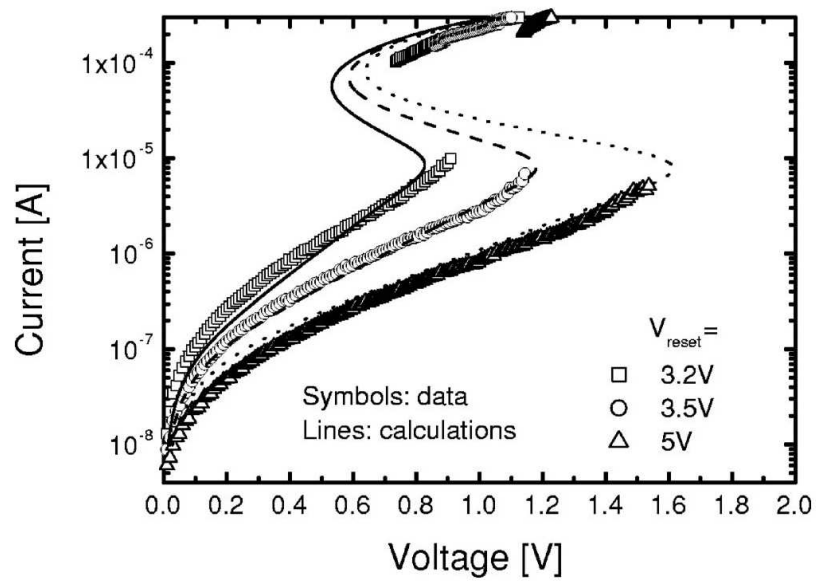
Figure 3.8: Measured and calculated $I - V$ curves for a PCRAM cell at three different reset states that arise from increasing the reset voltage. These three different states were obtained by pulses with amplitude $V = 3.2$, 3.5 and 5 V, respectively. Different sizes of the amorphous chalcogenide were obtained in correspondence to the amplitude of the pulses. Taken from [30].

field. This stronger field enhances nucleation of an additional neighbour conductive particle, resulting in the growth of a needle shaped conductive crystallite. This process continues until the conductive crystalline filament reaches through the entire amorphous region.

As mentioned by Greer *et al* [35] "in the presence of an electric field, the electrostatic energy is lowered by the polarization of the dielectric medium". A nucleated particle decreases the electrostatic energy [97] according to

$$F_E = -\frac{\Omega E^2 \varepsilon}{8\pi n}, \tag{3.7}$$

where $E$ is the local strength field, $\varepsilon$ is the dielectric permittivity of the material, $\Omega$ is the molecular volume of the nucleus and $n$ is the depolarizing factor. For a spherical particle, the depolarizing factor is $n = 1/3$.

Adding this electric field induced nucleation $F_E$ to the free energy $F_{sph}$ for a spherical particle yields

$$F_{sph} = 4\pi R^2 \sigma - 4\pi R^3 \Delta g / 3 - R^3 E^2 \varepsilon / 2, \tag{3.8}$$

where $\sigma$ the surface energy and $\Delta g$ the bulk free energy between the two phases. The critical radius $R_{sph}$ and nucleation barrier $W_{sph}$ is calculated by minimizing $F$, giving

$$R_{sph} = \frac{R_0}{1 + E^2 / E_0^2}, \quad R_0 \equiv 2\sigma / \Delta g, \tag{3.9}$$

$$W_{sph} = \frac{W_0}{1 + E^2 / E_0^2}, \quad W_0 \equiv 16\pi \sigma^3 / 3\Delta g^2. \tag{3.10}$$

where the characteristic field $E_0$ [96] is defined as:

$$E_0 = 2[W_0 / (\varepsilon R_0^3)]^{1/2}, \tag{3.11}$$

and values of $E_0$ are typically in the range of several MV/cm. The threshold field $E_{th}$ which is necessary to grow a nucleus to a conducting filament between the electrodes according to [97] can be calculated as

$$E_{th} = \frac{1}{\ln(\tau/\tau_0)} \frac{W_0}{k_B T} \sqrt{\gamma \frac{W_0}{\varepsilon}} \tag{3.12}$$

where $W_0$ is the energy barrier at zero field, $k_B$ is the Boltzmann constant $\tau_0 \approx 10^{-13}$ is the characteristic vibrational time and $\gamma$ summarizes the geometry properties of the nucleus and the electrodes [97].

Following this model, Karpov et al. [96], estimated the field effect on the threshold switch delay time by

$$\tau(E) = \tau(0) \exp[W(E)/K_B T], \tag{3.13}$$

where $\tau(0)$ is the nucleation time in the zero field, and $W$ is the nucleation barrier depending on the electric field $E$, yielding good agreement with experiments [96].

In the Karpov model the switching statistics are found to be consistent with the field-induced nucleation mechanism [96]. In addition to this, in the Karpov's model the physical mechanism of oscillations and their stochastic nature can be effectively described in the framework of field-induced nucleation. A more advanced model based on the field-induced nucleation framework should incorporate the electric field on the activation energy of nucleation, as it has been recently suggested that high applied fields can reduce the activation energy of nucleation [98].

# Chapter 4

# A multiphysics cellular automata model for simulation of phase change devices

Phase change devices are based on reversible switching between amorphous and crystalline states, which is accompanied by a change in their optical and electrical properties. This renders phase change materials suitable for optical and electronic data-storage applications, where a structural transformation occurs by appropriate heating via laser and electrical pulses respectively [23, 99].

After great success in optical data storage (e.g. for re-writable CD, DVD and BD disks), phase change materials are perhaps the most mature of the emerging non-volatile, electrical memory technologies. Phase change memory has demonstrated the possibility for large-scale manufacture and it is soon expected to enter production for NOR flash memory and some embedded memories. Furthermore it may also replace low-cost NAND flash [100]. Phase change random access memory (PCRAM) devices rely on reversible transitions between the amorphous (high resistivity) and polycrystalline (low resistivity) phases of a phase change material. The transitions are accomplished by heating the material via electrical pulses.

To understand the physical processes involved in the use of phase change materials for electrical data storage applications, and to design and optimize future devices, it is

necessary to develop realistic physical models for the electrical, thermal, phase change, and other processes that may be involved in writing and reading data.

In this chapter therefore, a fully-coupled electrical, thermal and phase change simulator for 2D PCRAM geometries (with cylindrical symmetry) is presented. The electrical and thermal models are implemented using finite element (FE) software ($Comsol^{TM}$), to simultaneously solve the Laplace and heat-diffusion equations. For the threshold switching, the model described in [30] and in Chapter 3, is used to simulate this effect. The cellular automata approach (GCA), described in Section 2.5 and [29], is incorporated for realistic simulation of the phase change transformations. A detailed study of the Gillespie cellular automata (GCA) approach [29] was included in Section 2.5 and a thorough analysis and simulation of the different crystallization processes (nucleation and growth, partial crystallization and spatio-temporal annealings) in a continuous thin film of $Ge_2Sb_2Te_5$ material was provided. The GCA approach was shown to have great potential (as is shown in Tables 2.2 and 2.3) for the realistic simulation and design of current and future phase change based devices [23]. Here, we give a complete description of the numerical implementation of the coupled physical model, as well as applying the model to investigate switching processes in typical PCRAM cells.

## 4.1 Implementation for realistic devices

As mentioned above, phase change memory (PCRAM) devices utilize a reversible switching transition from a high-resistance (amorphous) state to low-resistance (crystalline) state in order to store data. The transitions between these two states are referred to as the SET process (amorphous to crystalline) and the RESET process (crystalline to amorphous). Therefore, these two process have to be simulated in order to be able to completely investigate the phase transformation in PCRAM. The general approach for modelling of the SET and RESET processes is described through a block diagram as in Figure 4.1. This diagram will be used in the rest of this chapter as a general scheme to simulate any of these two processes (SET and RESET) in phase change devices.

Firstly, the geometry of the PCRAM device in the graphical user interface ($Comsol^{TM}$ Multiphysics software) is created, specifying the parameter values for each of the ma-
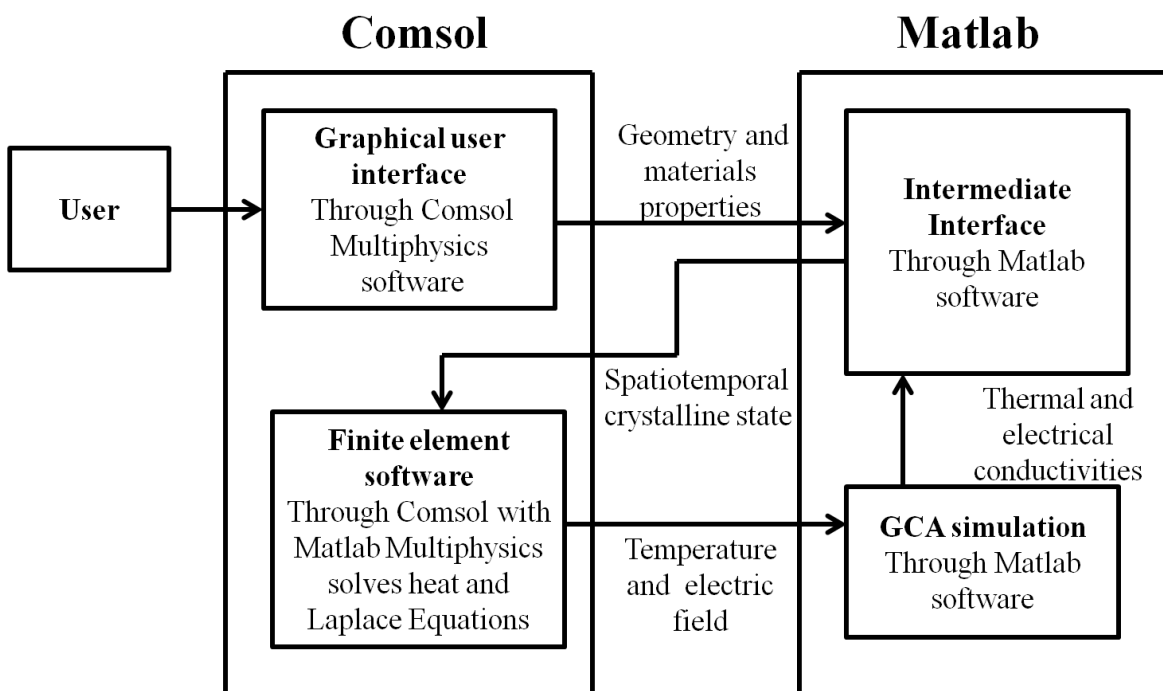
Figure 4.1: Block diagram of the interfaces for the implementation of the coupled FE-GCA model for device-like configurations.

terials used in that geometry. Secondly, the device geometry is loaded through an intermediate interface which enables one to apply the corresponding electrical pulse for a SET or RESET process. This intermediate interface passes the actual spatiotemporal crystalline state to the finite element software $Comsol^{TM}$ to solve, for the specified time step, the potential distribution and the resulting current density. With the current density from the electrical model, the temperature distribution in the phase change material is solved by the thermal model. This electro-thermal solution is made in $Comsol^{TM}$ Multiphysics with Matlab, which allows one to integrate the finite element software with the GCA algorithm, which is written in Matlab. The temperature and electric field distributions are returned to the GCA algorithm to simulate crystallization, melting, and re-amorphization in the device. The resulting phase transitions affect the electrical and thermal characteristics of the material. Finally the new thermal and electrical conductivities are returned to $Comsol^{TM}$ Multiphysics. The process repeats until the algorithm reaches the pre-established time. This pre-established time is the time required for the phase change material to get back to room temperature. A schematic flow diagram which describes all the numerical details of the algorithm is shown in Figure 4.2.

## 4.2   The electrical model

For the SET and RESET processes, current is injected into the material through the electrode and the resulting resistive heating (Joule heating) effects the phase transformation. The electrical model provides the current density distribution in the material. The current density distribution is modelled by the solution of the Laplace equation:

$$\nabla \cdot (\sigma \cdot \nabla V) = 0 \tag{4.1}$$

where $V(\mathbf{x})$ is the electrical potential, $\sigma$ is the electrical conductivity and $\nabla$ is the gradient operator. In (4.1) the only parameter required is the electrical conductivity, which has to represent the electrical characteristics of the phase change materials, and appropriate boundary conditions have to be set. The boundary conditions for the electrical model were set as electrical insulation on all exterior boundaries except across the elec-

trodes, where a constant voltage was applied. For the interior boundaries continuity was applied. In phase change materials, a reversible electrical transition between a highly resistive state and conductive state can be observed in the amorphous alloy (see Chapter 3). A simple model that describes this behaviour by the introduction of temperature and electrical field dependencies of the electrical conductivity of the amorphous chalcogenide alloy [101, 102], i.e.:

$$\sigma_{am}(T, E) = \sigma_{0am} \times \exp\left(-\frac{\Delta\xi_{am}}{kT}\right) \times \exp\left[\frac{E}{E_0}\right] \quad \Omega^{-1}m^{-1} \tag{4.2}$$

where $\sigma_{am}$ is the electrical conductivity of the $Ge_2Sb_2Te_5$ for the amorphous phase, $\sigma_{0am}$ is a constant and $\Delta\xi_{am}$ is the activation energy for the temperature dependence of $\sigma$. The electrical field is $E$ and $E_0$ is the electrical field at which threshold switching occurs (with $E_0$ typically $5 \times 10^7 V/m$ -see [103]).

In this simple model the electrical conductivity of the crystalline chalcogenide behaves in a way which conforms to a Arrhenius relation [82] as follows:

$$\sigma_{cryst}(T) = \sigma_{0cryst} \times \exp\left(-\Delta\xi_{cryst}/kT\right) \quad \Omega^{-1}m^{-1} \tag{4.3}$$

with $\sigma_{cryst}$ the electrical conductivity of the $Ge_2Sb_2Te_5$ for the crystalline phase, $\sigma_{0cryst}$ a constant, $\Delta\xi_{cryst}$ the activation energy for the temperature dependence of $\sigma_{cryst}$ in the crystalline state. $\sigma_{0cryst}$ and $\Delta\xi_{cryst}$ are obtained by fitting to experimental data.

While this simple approach has been used with some success previously, in particular for modelling scanning probe based phase change memories [103], here the more complex, but physically realistic, model by Ielmini and previously described in Section 3.2 and [30] is used.

## 4.2.1 Integration of Ielmini's model in the Multiphysics framework

It is easily seen that equations (3.3) and (3.4) cannot be directly applied into the Laplace equation. Therefore, it is essential to derive the electrical conductivity of the amorphous

$Ge_2Sb_2Te_5$ from Ielmini's model, and then introduce this conductivity into the Laplace equation.

In order to derive an expression for the electrical conductivity of the amorphous $Ge_2Sb_2Te_5$, Ohms Law is used in a specific element by

$$\frac{u_{ele}}{\sigma \cdot S_{ele}} = \frac{V_{ele}}{I_{ele}} \tag{4.4}$$

where $u_{ele}$ and $S_{ele}$ are the thickness and the cross-sectional area of the element, respectively, $V_{ele}$ and $I_{ele}$ are the voltage across the element and the current flowing through the element, respectively, and $\sigma$ is the electrical conductivity of the element.

Rewriting (3.4) as

$$I_{ele} = 2qS_{ele}(N_{T1} + N_{T2})\frac{\Delta z}{\tau_0}e^{-\frac{E_C - E_F}{kT}} \sinh\left(\frac{qV_{ele}}{kT}\frac{\Delta z}{u_a}\right)(1 + \gamma) \tag{4.5}$$

and now substituting (4.5) into (4.4) to give

$$\frac{u_{ele}}{\sigma \cdot S_{ele}} = \frac{V_{ele}}{2qS_{ele}(N_{T1} + N_{T2})\frac{\Delta z}{\tau_0}e^{-\frac{E_C - E_F}{kT}} \sinh\left(\frac{qV_{ele}}{kT}\frac{\Delta z}{u_a}\right)(1 + \gamma)} \tag{4.6}$$

results in

$$\sigma = \frac{u_{ele}}{V_{ele}} \cdot 2qS_{ele}(N_{T1} + N_{T2})\frac{\Delta z}{\tau_0}e^{-\frac{E_C - E_F}{kT}} \sinh\left(\frac{qV_{ele}}{kT}\frac{\Delta z}{u_a}\right)(1 + \gamma) \tag{4.7}$$

Now we use the fact that the electric field across the element $E = V_{ele}/u_{ele}$, so that

$$\sigma = E^{-1} \cdot 2qS_{ele}(N_{T1} + N_{T2})\frac{\Delta z}{\tau_0}e^{-\frac{E_C - E_F}{kT}} \sinh\left(\frac{qV_{ele}}{kT}\frac{\Delta z}{u_a}\right)(1 + \gamma) \tag{4.8}$$

where $\gamma$ is as given in (3.5).

Therefore, the electrical conductivity of the amorphous phase of $Ge_2Sb_2Te_5$ is now expressed in a form that: is consistent with the Ielmini model and which can describe both sub-threshold conduction and threshold switching in a compact and physically realistic way.

## 4.3 The thermal model

| Parameter | Value | Units |
|:---:|:---:|:---:|
| $N_{T1} + N_{T2}$ | $1 \cdot 10^{25}$ | $\text{m}^{-3}$ |
| $N_{T1}$ | $0.5 \cdot 10^{25}$ | $\text{m}^{-3}$ |
| $\tau_n$ | $1 \cdot 10^{-9}$ | s |
| $\tau_0$ | $1 \cdot 10^{-15}$ | s |
| $\Delta z$ | $5 \cdot 10^{-9}$ | m |
| $E_C - E_F$ | 0.35 | eV |
| $E_{T2} - E_{T1}$ | 0.35 | eV |
| **m** | $9.1 \cdot 10^{-31}$ | kg |
| **q** | $1.6 \cdot 10^{-19}$ | C |
| $\hbar$ | $1.05 \cdot 10^{-34}$ | J· s |
| **k** | $1.38 \cdot 10^{-23}$ | J/K |

Table 4.1: Parameters for the analytical threshold switching model of $Ge_2Sb_2Te_5$ phase change material as in [30].

In the switching operation an electric current passes as a heat source through the memory cell creating the Joule heating. As a consequence, a heat diffusion process induces a temperature distribution throughout the material. The temperature profile is obtained by the solution of the heat transfer equation for temperature $T(\mathbf{x}, t)$

$$\rho C_p \frac{\partial T}{\partial t} - K \cdot \nabla T = Q \tag{4.9}$$

with $\rho$ being the material density, $C_p$ the specific heat capacity per unit mass, $K$ the thermal conductivity of the material, and $Q$ the heat source per unit volume generated inside the material. The heat source thorough Joule heating is $Q = E \cdot J$, with $E$ and $J$ the electrical field and the current density respectively.

At room temperature the thermal conductivity of the material in the amorphous state is 0.19 W/mK and in the crystalline state is in the range 0.5-0.58 W/mK [104, 105, 106, 107]. In this work, the values of the thermal and electrical conductivity of $Ge_2Sb_2Te_5$ are assumed to switch from amorphous to crystalline values when the crystal fraction of the material reaches the percolation value 15 % [62].
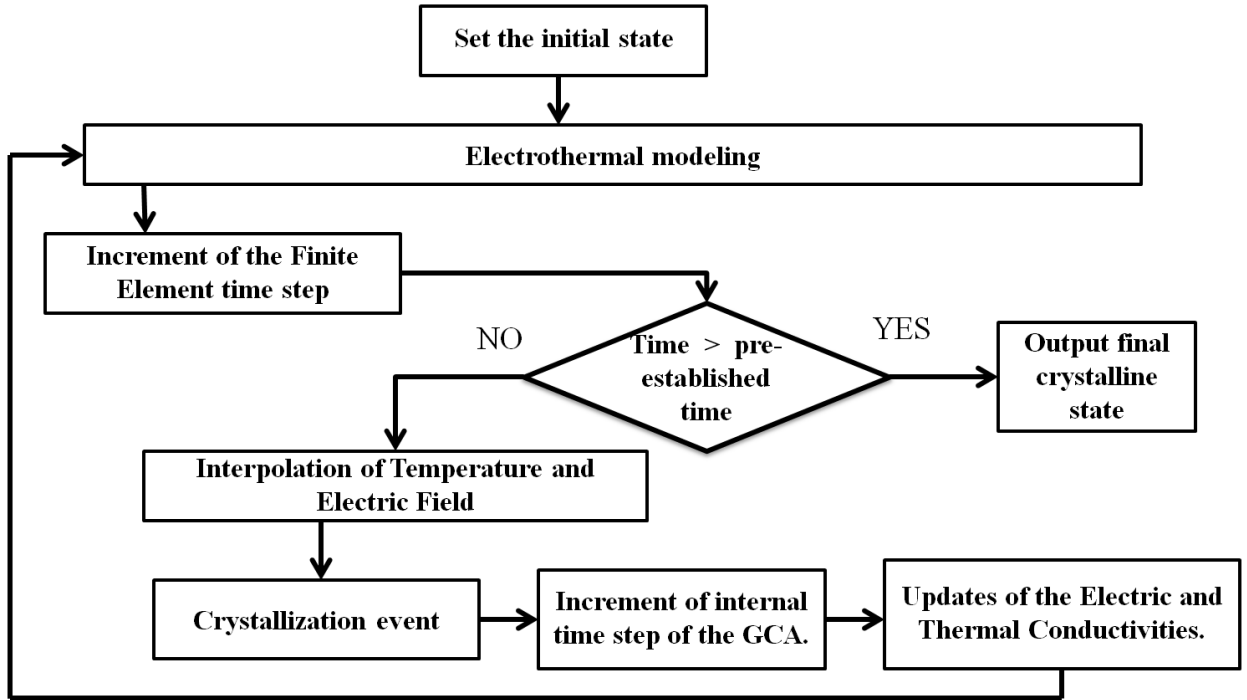
Figure 4.2: Scheme of the numerical implementation for the complete coupled physical model which describes the full integration of the electro-thermal interaction with the phase change transformation.

## 4.4   Numerical Implementation

The complete coupled physical model describing the electro-thermal interaction with the phase change model is shown schematically in Figure 4.2 and described in the following:

1. The device geometry is created and the parameter values are loaded into $Comsol^{TM}$ Multiphysics. Figure 4.3 shows the typical geometry structure considered in this chapter. The mesh created with this finite element software is chosen to be finest in the phase change region. The mesh used through the simulations is illustrated in Figure 4.3.

2. Depending on the process to be simulated (SET or RESET), the initial phase is specified. The RESET process has two possible initial states: (a) Initial monocrystalline state and (b) Initial polycrystalline state (meaning that a SET pulse has
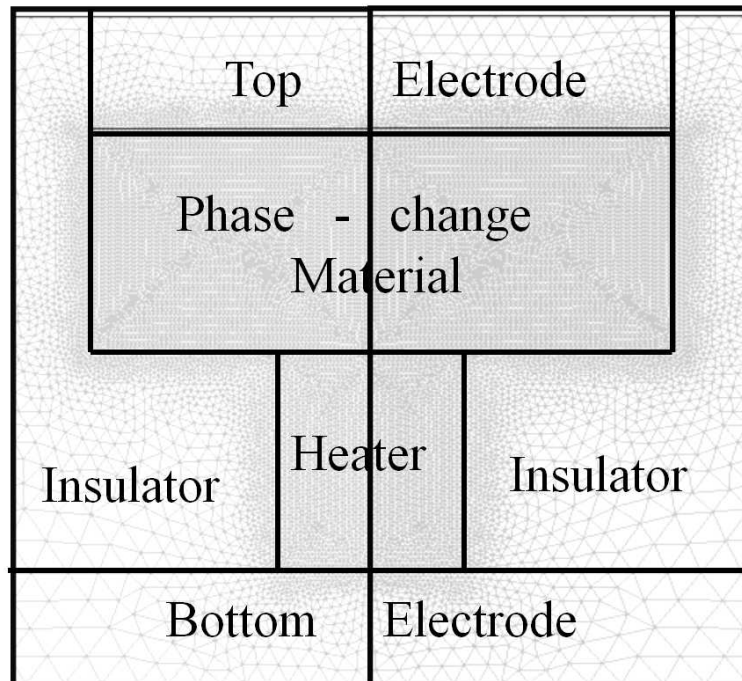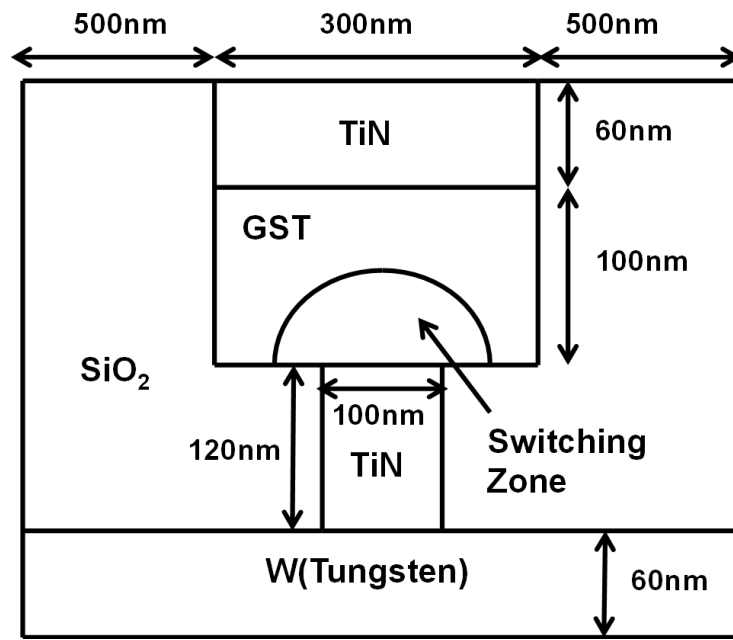
Figure 4.3: Schematic of the PCRAM "mushroom" cell used for the device simulations. The phase change region contains smaller elements since this is the region where phase transformations occur. The total number of elements in the geometry is 35808.

previously been applied).

3. After choosing the process, the coupled transient heat diffusion and Laplace equation are simultaneously solved to find the temperature and electric field in the device. The solution is obtained through $Comsol^{TM}$ Multiphysics using a internal loop with controlled time step $dt$.

4. A rectangular mesh in the GCA with square elements of size 0.82 nm (corresponding to the diameter of a reduction of a spherical "monomer" of $Ge_2Sb_2Te_5$) is created.

5. Temperature and electric field are extracted for the phase change region ($Ge_2Sb_2Te_5$ in this case) and then interpolated into the GCA mesh. The GCA mesh differs from the finite element mesh as the GCA mesh is a rectangular lattice.

6. A complete sequence of crystallization events occur according to the GCA algorithm (as described in Section 2.5 and [29]). This series of events have their own internal loop. These crystallization events continue until the internal time step of the finite element $dt$ is reached. The value of $dt = 0.1$ ns is chosen to maintain an approximating isothermal assumption. The choice of $dt$ represents a compromise between maintaining the isothermal assumption and the time it takes to complete the simulation.

7. According to the new crystalline phase state, an update of the electrical and thermal conductivities is performed. This requires an interpolation onto the finite element mesh.

8. The new thermal and electrical conductivities are used for the electro-thermal modelling of the next FE timestep.

9. The process repeats until the pre-established time is reached. The pre-established time is the time required for the phase change material to get back to room temperature. The final crystalline phase is saved for further analysis and to serve as an initial state of future processes.

| Element | K(W/mK) | C(J/m$^3$K) | $\sigma(\Omega m)^{-1}$ |
|---|---|---|---|
| $TiN(heater)$ | 17 | $7 \times 10^5$ | $1.12 \times 10^5$ |
| $TiN(electrode)$ | 19 | $2.16 \times 10^6$ | $5 \times 10^6$ |
| $SiO_2$ | 1.4 | $3.1 \times 10^6$ | $1 \times 10^{-16}$ |
| $W(electrode)$ | 175 | $2.35 \times 10^6$ | $18 \times 10^6$ |
| $Ge_2Sb_2Te_5(amorphous)$ | 0.2 | $1.25 \times 10^6$ | $\sigma_{am}(T, E)$ as in (4.8) |
| $Ge_2Sb_2Te_5(crystalline)$ | 0.5 | $1.25 \times 10^6$ | $\sigma_{0crys} \exp(\Delta\xi_{crys}/KT)$ as in (4.3) |

Table 4.2: Thermal and electrical material properties. See [108].

## 4.5  Simulation of the RESET and SET processes in PCRAM "mushroom-type" cells

The RESET operation (crystalline $\rightarrow$ amorphous) in a PCRAM cell is accomplished by applying a large electrical current pulse for a short time period, which first melts and then quenches rapidly the programming region (the switching zone shown in Figure 4.3). By doing this a (highly resistive) amorphous region in the PCRAM cell is created. This amorphous region is in series with any crystalline region of the PCRAM cell and effectively determines the resistance of the cell between the top electrode contact (TEC) and the bottom electrode contact (BEC). The tungsten ($W$) layer is used as the plug bottom electrode contact. The function of the $SiO_2$ layer is the dissipation of the heat. For the re-crystallization of the amorphous material from the RESET operation, a medium amplitude electrical current pulse is applied to anneal the programming region at a temperature between the crystallization temperature and the melting temperature for a time period long enough to re-crystallize the amorphous region. To read the state of the programming region, the resistance of the cell is measured by passing an electrical current small enough so as not to disturb the existent state.

For electrical evaluation of RESET/SET behaviour, the PCRAM is typically embedded into a test bench comprising an electrical pulse source, an external load resistance $R_L$, and the PCRAM itself, as in Figure 4.4. The material parameters used in the simulations of the RESET and SET processes are summarised in Table 4.2.
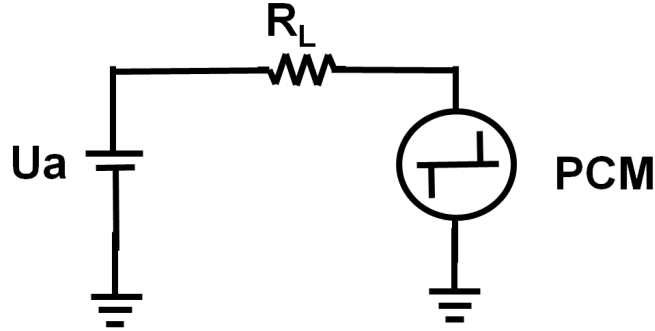
Figure 4.4: Typical test system for the investigation of switching operations of a PCRAM cell comprising an electrical pulse generator and an external load resistance $R_L$ in series with the device. Typical values for $R_L$ are 1-10 k$\Omega$, whereas for $u_a$ goes around 1-5 V depending on the PCRAM geometry.

## 4.5.1   Reset operation

The RESET process consumes a relatively large amount of power due to the high temperatures required to melt the material. The current during this process is determined by the properties of the material such as the resistivity and thermal conductivity as well as the device structure. For the device structure in Figure 4.3 with materials properties as in Table 4.2 a pulse of 2.5 V was required. We performed several simulations with lower pulse amplitudes but the temperatures exhibited in the PCRAM cell were below melting temperature which allows the $Ge_2Sb_2Te_5$ to recrystallize and thus obtain a final state with lower resistance. The shape of the pulse during the RESET operations is shown in Figure 4.5. The total pulse duration is 20 ns with a rising edge of 5 ns and falling edge of 3 ns. Note that the falling edge is a critical parameter in the RESET operation. In the simulations that we performed with a falling edge not fast enough, the melted $Ge_2Sb_2Te_5$ material re-crystallized leading to a final state with lower resistance. In general, the RESET process is a much faster process, making the operating speed of PCRAM limited by the SET programming. The RESET operation (crystalline→amorphous) is simulated
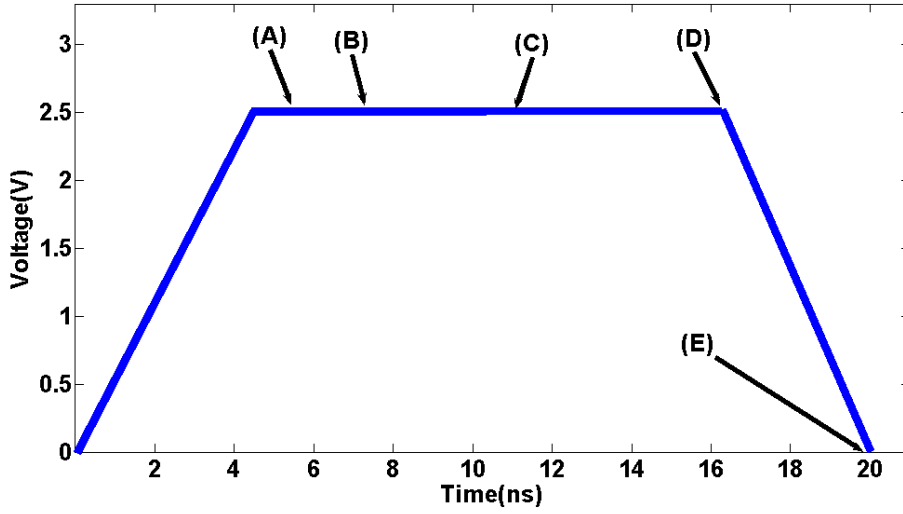
Figure 4.5: Applied RESET pulse to reset the device shown in Figure 4.3. Points (A)-(E) correspond to the crystal structures of Figure 4.9.

with the $Ge_2Sb_2Te_5$ initially in fully crystalline state. The points (A)-(E) in Figure 4.5 correspond to the specific times where the crystalline structure is illustrated through the sequence of images in Figure 4.9. The "mushroom" shaped amorphous dome starts to form in the region where temperatures are above 900 K, and then continues expanding to obtained the final shape as shown in Figure 4.9 (E).

As mentioned above, during this process the material reaches temperatures above melting point as illustrated by Figure 4.6. Temperatures in the RESET process in the $Ge_2Sb_2Te_5$ material go up to 1200 K at the maximum amplitude of the pulse. A peak in the maximum temperature is observed in Figure 4.6 at time t = 18 ns. Figure 4.7 shows the temperature distribution at the time the material reaches the highest temperatures (marked as (D) in Figure 4.5). The highest temperatures are obtained in the region nearest to the heater. The regions with temperature higher than the melting temperature will transform into an amorphous material as seen in Figure 4.9 (E).

Figure 4.8 illustrates the electric field at the maximum amplitude of the pulse (t = 17 ns). Values of the electric field are in the range 0-30 MV/m with the highest values found at the region lying between the $Ge_2Sb_2Te_5$ material and the heater. The role of the electric field in the switching process will be studied in more detail in Chapter 7.
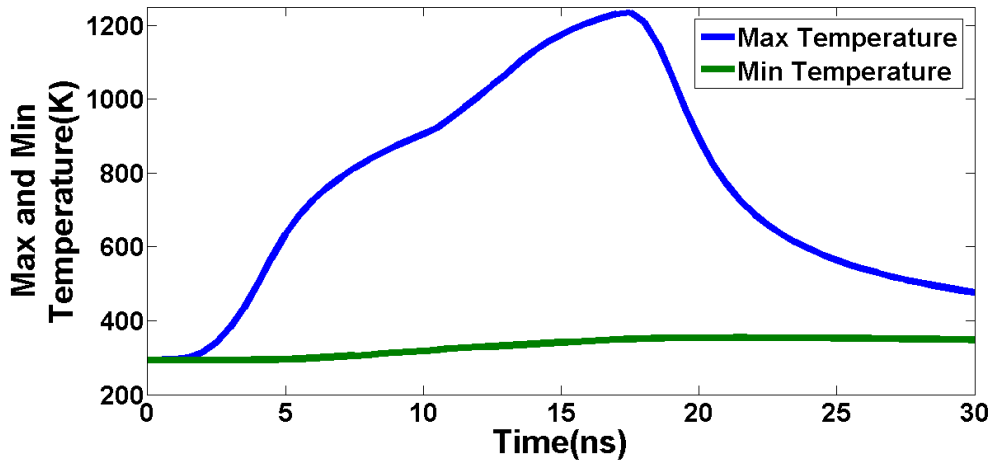
Figure 4.6: Maximum and minimum temperatures in K for the $Ge_2Sb_2Te_5$ layer during the RESET. A peak in the maximum is observed at time t = 18 ns and afterwards the $Ge_2Sb_2Te_5$ layer starts to cool down.
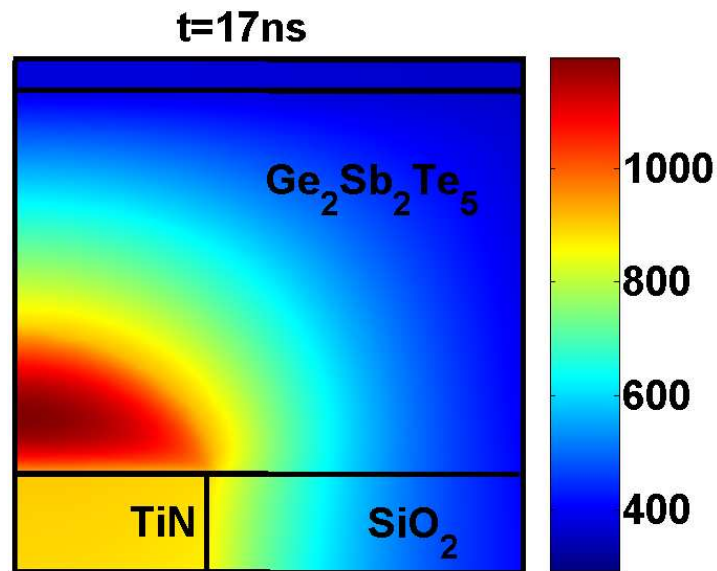


Figure 4.7: Temperature distribution (K) in the PCRAM cell during RESET at time t = 17 ns. Here it is only shown the region of interest with the surrounding areas. Observe the higher temperatures above the heater.
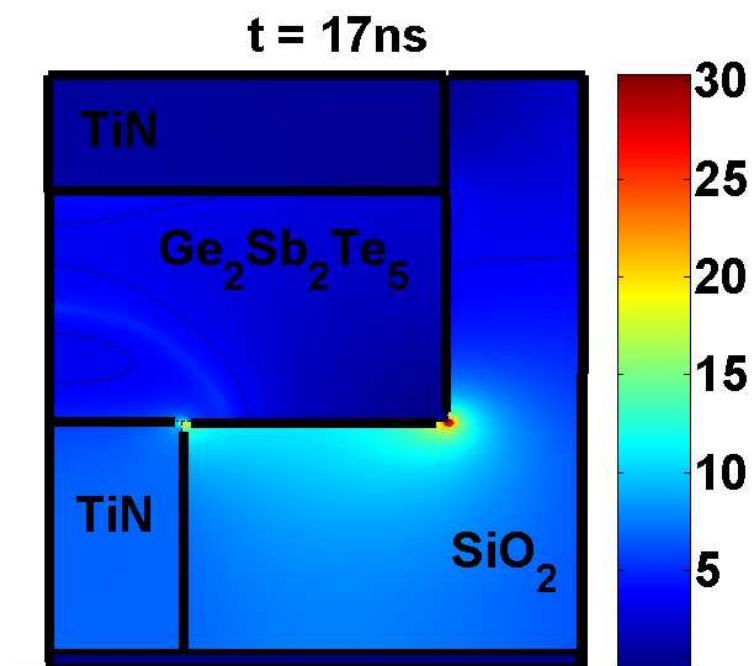
Figure 4.8: Electric field distribution (MV/m) in the PCRAM cell during RESET at time t = 17 ns. Here it is only shown the phase-change region with the surrounding areas. Observe the higher values ($\approx$ 20 MV/m) are obtained in at the corner interface with the heater.
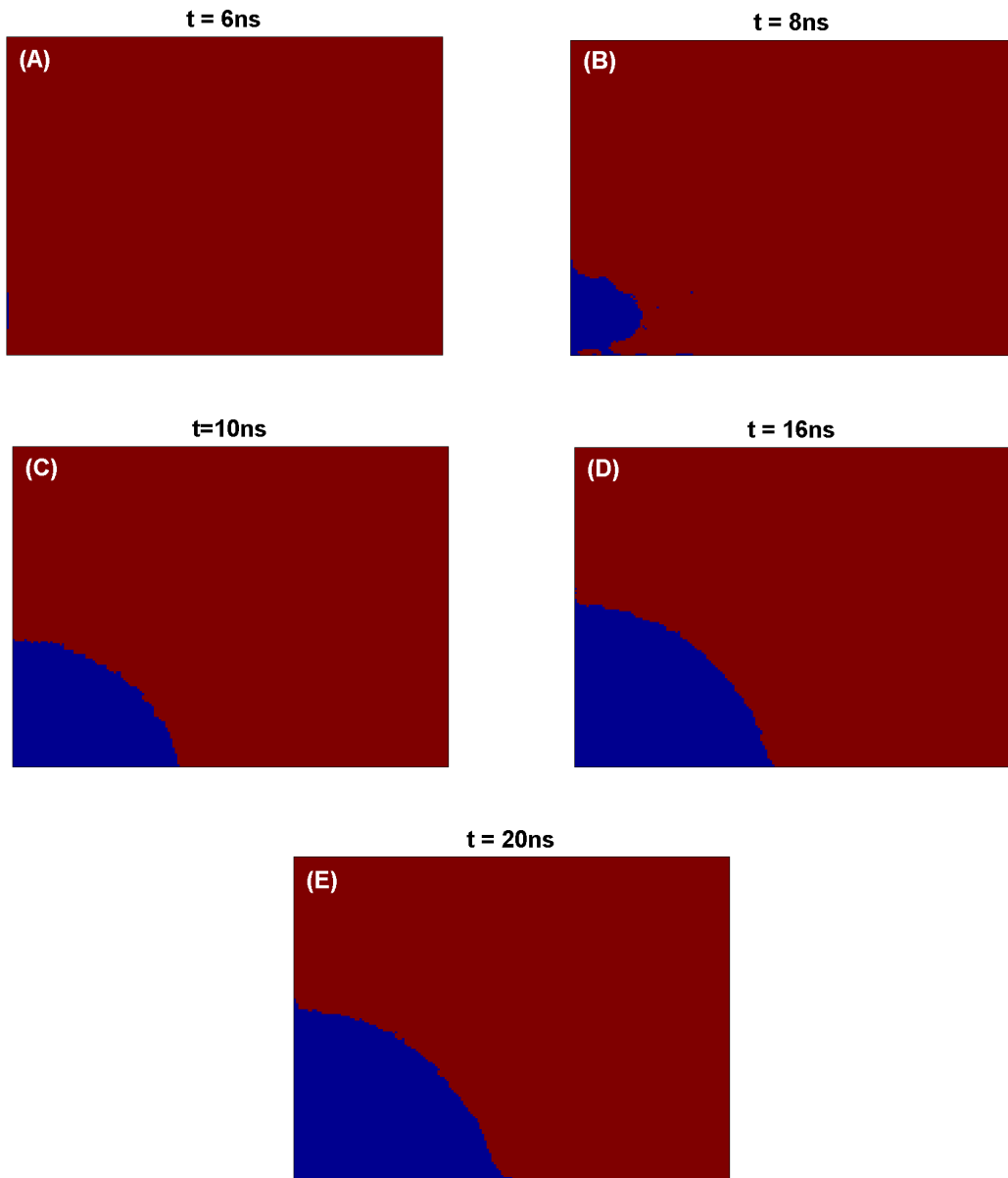
Figure 4.9: Crystal structure of the $Ge_2Sb_2Te_5$ layer for different times during the RE-SET process. From left to right the time is 6 ns, 8 ns, 10 ns, 16 ns, 20 ns in correspondence with marks in Figure 4.9 (A)-(E). The red colour corresponds to the initial crystalline structure. The blue colour corresponds to the amorphous state. The initial monocrystalline state is shown in (A). A small shaped amorphous dome appears (B) at time t = 8 ns and continues growing (C)-(D) until it reaches his final state (E).

In the RESET process there is a decay in the overall crystal fraction in the cell since there is an amorphization of the $Ge_2Sb_2Te_5$ material due to the high temperatures in this region. The decay of the crystal fraction is observed in Figure 4.10. In Figure 4.10, the maximum value of the crystal fraction ($\chi = 1$) corresponds to the total volume of the phase-change region in the cell. The crystal fraction starts to decay after $6ns$ where the maximum amplitude of the pulse is reached, as shown in Figure 4.5. This decay continues until the pulse starts to switch off (t = 17 ns as sketched in Figure 4.5). After switching the device off there is only a slight variation in the crystal fraction.

The evolution of the structure is the result of a complex sequence of events described previously by the GCA approach (Chapter 2, Section 2.5). With the aim of gaining more detail on the dynamics of the amorphization, the rates of the different events revealed by the GCA simulation of the phase-transition (nucleation, growth and dissociation) are plotted in Figures 4.11. Observe that in Figures 4.11 the dissociation rates ($\approx$ 1500 a.u.) are much greater than nucleation rates ($\approx$ 600 a.u.). From Figure 4.11 we observe a transient effect in the growth rates for a short period of time (5-10 ns), where temperatures are between 600-900 K. This effect eventually disappears due to the high temperatures which melts these small crystals. A small "mushroom" shaped amorphous dome appears (as observed in Figure 4.9 (B)) mainly due to dissociation. During the formation of the amorphous dome, small crystal clusters appear and disappear without overcoming the critical nucleus size. The small "mushroom" shaped amorphous dome increases its volume as is seen in Figure 4.9 (B)-(E).

## 4.5.2   Set operation

In the recrystallization of the "mushroom" shaped amorphous dome (SET operation) the material is heated to a temperature between 600-900 K via a moderate electrical pulse of lower amplitude and longer duration (compared to the RESET pulse).

Figure 4.12 shows a typical (simulated) the current-voltage ($I - V$) for this process. When the voltage across the cell is increased up to the characteristic voltage threshold, the resistance of the material suddenly switches from a high resistivity to a low resistivity. This can be described with the electronic transitions between the OFF and ON
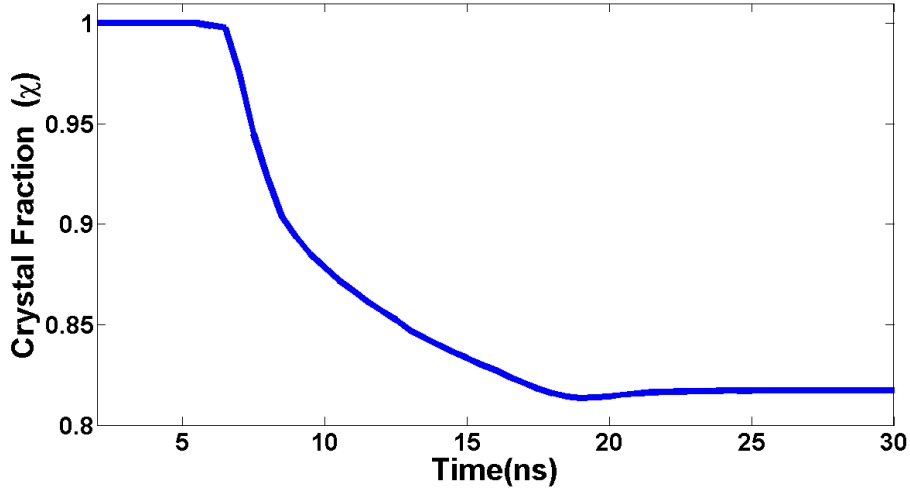
Figure 4.10: Crystal fraction ($\chi$) evolution of the $Ge_2Sb_2Te_5$ layer during the reset. The crystal fraction starts to decay when the temperatures are above 900 K at time t = 6 ns according to Figure 4.6. The minimum value of the crystalline fraction is $X = 0.82$. If the cooling down rate is very slow can lead to recrystallization of the cell as seen at time t $\approx$ 18 ns.

conductive states (as described in Section 3.2.2 and [30]).

The amplitude of the pulse in the SET operation has to be large enough to heat the $Ge_2Sb_2Te_5$ material to a temperature between 600-900 K, for a time period long enough to fully crystallize the amorphous dome. The current necessary to heat the $Ge_2Sb_2Te_5$ material to these temperatures (600-900 K), depends on the material parameters as well as the device structure. For a typical device structure like the one shown in Figure 4.3 with materials properties as in Table 4.2 a pulse of 1.5 V was required. We performed several simulations with lower amplitude pulses but the temperatures were not sufficient to complete crystallize the mushroom shaped dome. The trapezoidal shape of the pulse is illustrated in Figure 4.13. The total pulse duration is 100 ns with a rising edge of 30 ns and falling edge of 30 ns. We also performed different simulations with shorter duration pulses and the results show, in the active region, a residual amorphous region. Therefore, a SET pulse of 100 ns was required to fully crystallize the initial mushroom shaped dome.

Marks (A)-(F) in Figure 4.13 are in correspondence with the crystalline structure
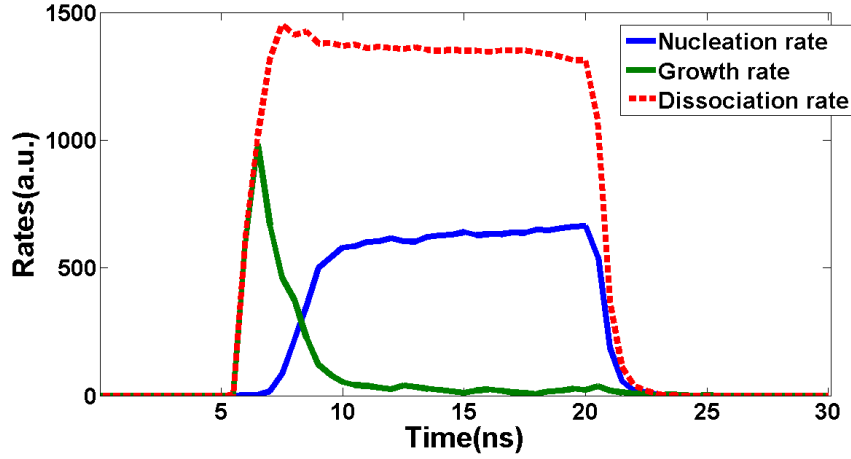
Figure 4.11: Rates of the different events revealed by the GCA simulation of the phase-transition for the RESET process. A big increase in the rates observed at time t = 7 ns. The rates units are arbitrary. The rates rapidly decay at time t = 22 ns when the $Ge_2Sb_2Te_5$ layer shows that the maximum temperatures are around 600 K (as seen in Figure 4.6). In the growth rate a transient increase is observed which rapidly decays after the material reaches melting temperature as seen in Figure 4.6. Dissociation rates are twice as large as the nucleation rates. It should be noticed that at time t = 7 ns the $Ge_2Sb_2Te_5$ layer shows that the maximum temperatures are around melting temperature, consequently transforming the phase change material into is liquid state. Once the phase change material is at his liquid state, the increases in the nucleation rates seen for times t ¿ 7 ns refers to the appearing of a new phase which in this case will be the amorphous phase. Therefore, when the original (parent) phase is the liquid state, nucleation refers to a site transform from the crystalline state to the amorphous state.
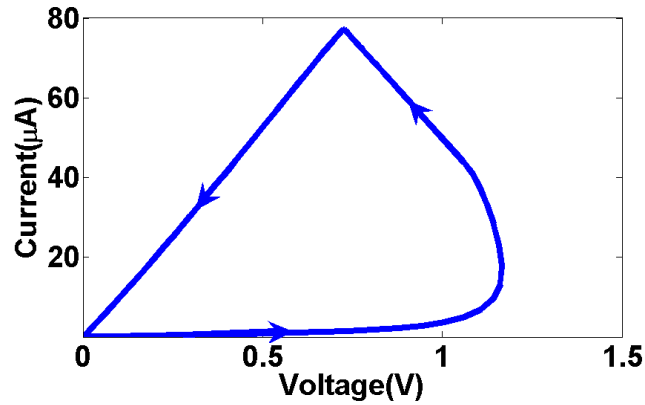
Figure 4.12: $I - V$ characteristic curve during the set process. At 1.2 V the threshold voltage is observed where the amorphous phase switches to a highly conductive state (ON state). After the threshold voltage is reached there is an increase in the current density and drop in the voltage.

as it is illustrated through the sequence of images in Figure 4.14. Initially, there is no crystallization due to the low temperatures present in the phase change material. After this period of time small crystal clusters appear in a region with temperatures around 600 K (Figure 4.14 (B)). At the maximum amplitude of the pulse (Figure 4.14 (B)-(E)) new regions nucleate and the previous crystal clusters continue growing. When the pulse starts to decrease, it is still possible to observe the appearance of new nuclei in the region which still remain amorphous (Figure 4.14 (F)). During this period of time the previously formed crystals continue growing until the initial amorphous dome is completely crystalline.

During the SET process the material is heated to temperatures between the crystallization temperature and the melting temperature for a relatively long period of time, as shown in the extreme values of the temperature (maximum and minimum) in Figure 4.15. The maximum temperature starts to rise after 30 ns, getting to values around 780 K. Two peak values are shown at times t = 34 and 74 ns. Figure 4.16 illustrates the temperature distribution in the phase change material at the time the material reaches the highest temperatures (marked as (E) in Figure 4.14).

Another parameter playing an important role in the transitions in phase change ma-
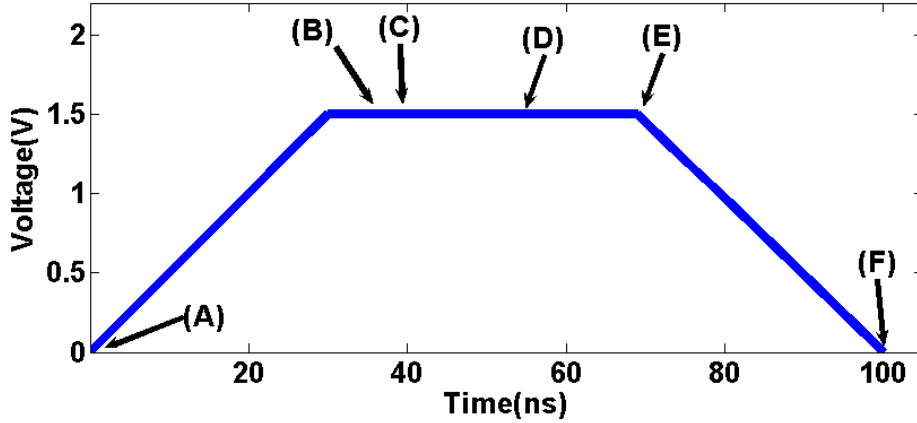
Figure 4.13: Applied SET pulse to set the device.  Marks (A)-(E) correspond to the crystalline structure in Figure 4.14.

terials is the electric field.  When the electric field across the amorphous region reaches a certain material-dependent threshold field (of the order of 10-100 MV/m [109]), the resistivity of the amorphous phase change material suddenly decreases by orders of magnitude, negative differential resistance is observed and threshold switching occurs.  In Figure 4.17, the electric field is illustrated showing the values through the material in agreement with voltage threshold in [109].  The high values of the electrical conductivity in Figure 4.18 illustrate the transition into the ON state of the initial amorphous dome. As a result of the electronically driven switch, more current starts to flow through the material to heat it above the crystallization temperature and crystalline clusters appear in the PCRAM cell, as shown in Figure 4.14 (B)-(F).

In the SET process the aim is to recrystallize the initial amorphous dome shown in Figure 4.14 (A). As a result, there is an increase in the crystal fraction, as illustrated in Figure 4.19, where the value $\chi = 1$ corresponds to the total volume of the phase change region and the value $\chi = 0.82$ corresponds to the volume of the initial amorphous dome. Figure 4.19 shows small temporal fluctuations in the crystal fraction due to the detachment and reattachment of sites from crystals that lead to grain coarsening over a long timescale.

To give more insight of the dynamics of the SET process, the rates of nucleation
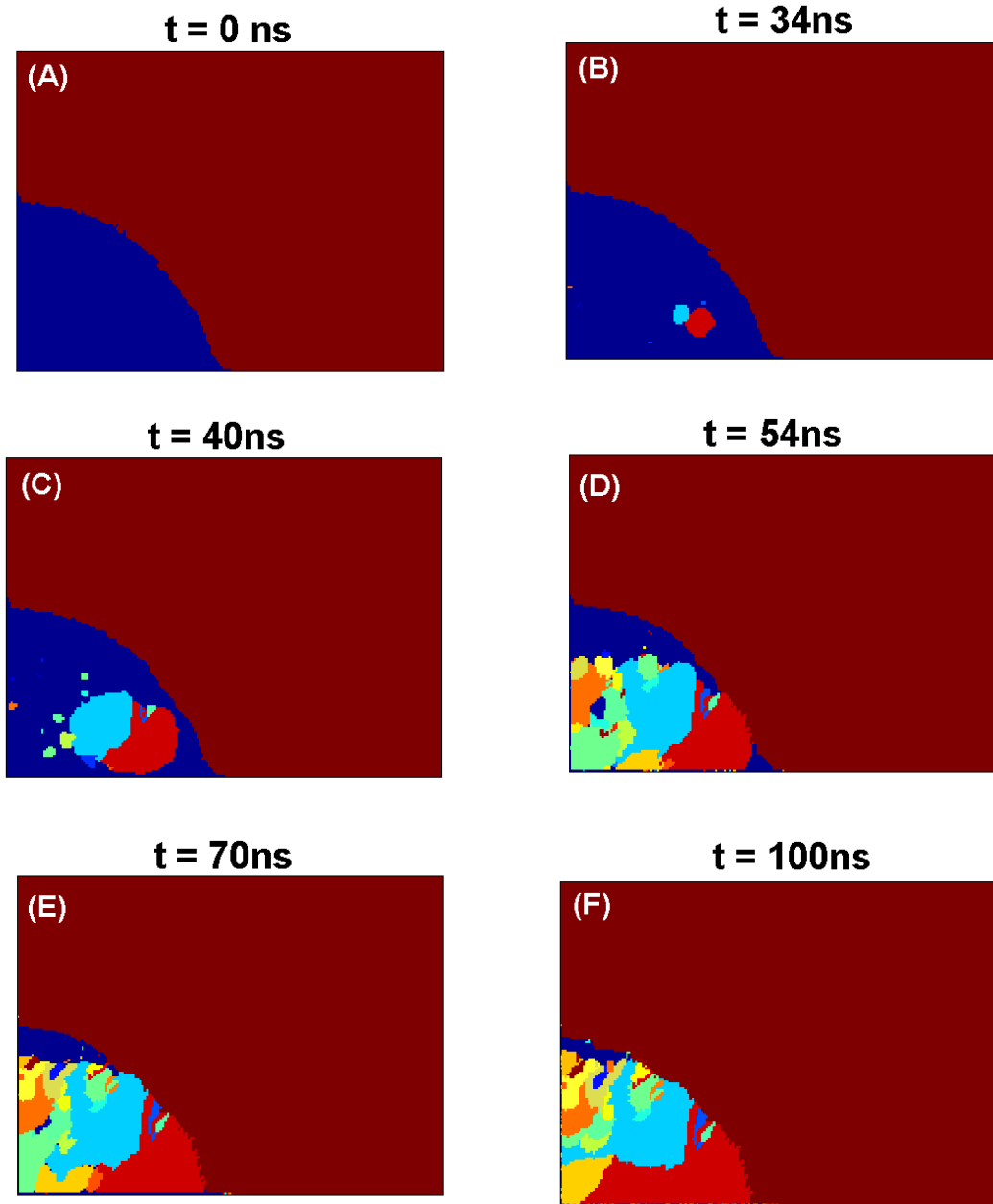
Figure 4.14: Crystal structure of the $Ge_2Sb_2Te_5$ layer for different times during the SET process. From left to right the time is 0 ns, 34 ns, 40 ns, 54 ns, 70 ns, 100 ns in correspondence with marks Figure 4.13 (A)-(F). The initial amorphous dome is shown in (A). A couple of small nuclei appear at time t = 34 ns which continue growing (B)-(E). New crystallites continue to nucleate and grow, as seen in (C)-(E). During cooling down of the device (Figure 4.13 (E)) still some crystallites nucleate and grow (E)-(F). Observe that the final state is fully crystalline (F). The bigger crystals are next to the interface with the heater.
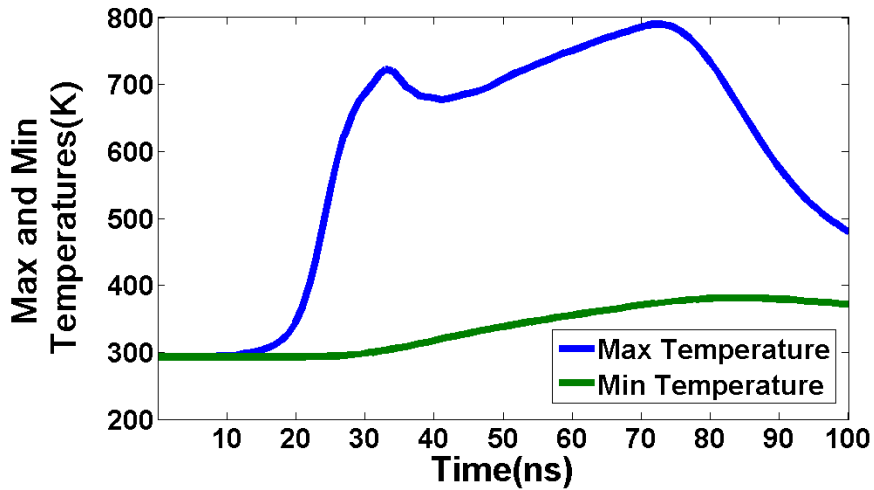
Figure 4.15: Maximum and minimum temperatures in K for the $Ge_2Sb_2Te_5$ layer during the SET. A peak in the maximum is observed at time t = 34 ns where small nuclei appear (Figure 4.14 (B)). These small nuclei have greater thermal conductivity which explain the slight decay in the maximum temperature. A second peak is observed at time t ≈ 70 ns after which the $Ge_2Sb_2Te_5$ layer starts to cool down (Figure 4.13 (E)). At time t = 100ns the maximum temperature is still high (≈ 500 K), equilibrium has been reached according to Figures 4.19 and 4.20. The minimum temperature in the $Ge_2Sb_2Te_5$ layer exhibits a slight increase due to diffusion of heat through this region.
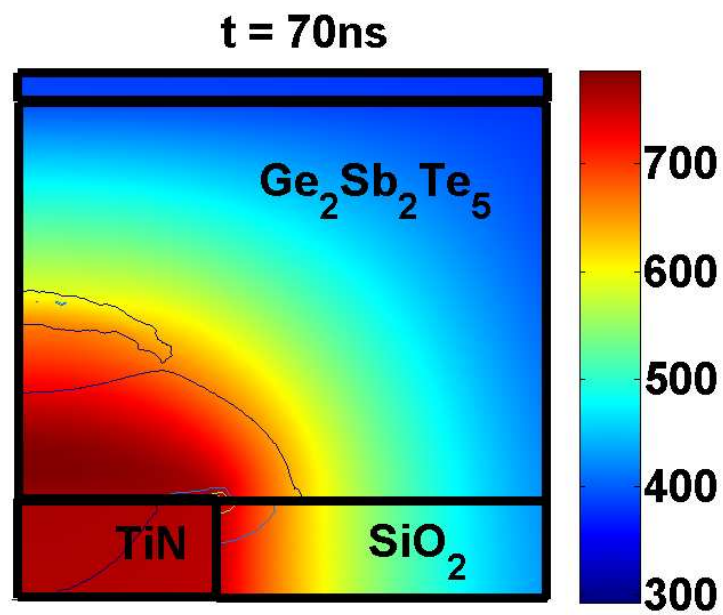
Figure 4.16: Temperature distribution in K of the PCRAM cell during the SET at time t = 70 ns marked in Figure 4.13 (E). Here it is only shown the $Ge_2Sb_2Te_5$ region with part of the surrounding areas. The heater exhibits relatively high temperatures.
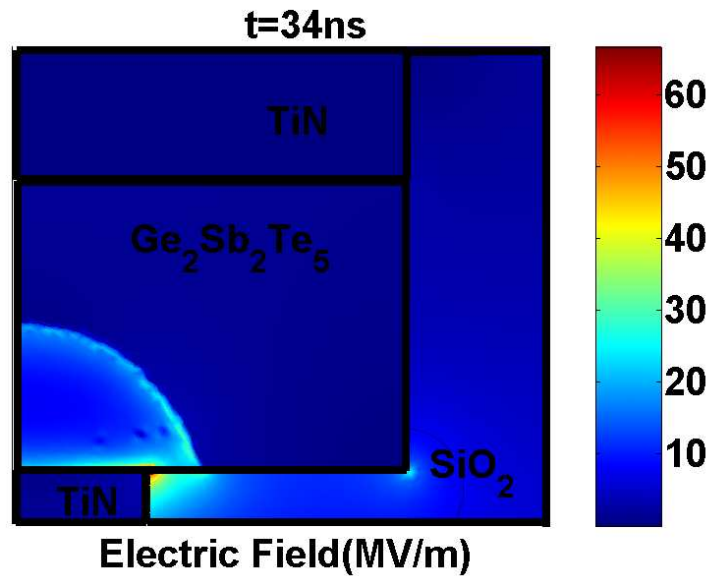
Figure 4.17: Electric field distribution in the PCRAM cell during the SET at time t = 34 ns. At this time the maximum amplitude of the pulse is reached (Figure 4.13 (B)). Observe that the electric field is very high in the corner between the $Ge_2Sb_2Te_5$ layer and the heater with values above 56 MV/m. This value was previously reported as the switching field threshold in [109]. In the regions where field threshold has been reached the amorphous phase switches to a highly conductive state (Figure 4.18) and some crystals start to appear (Figure 4.14 (B)).
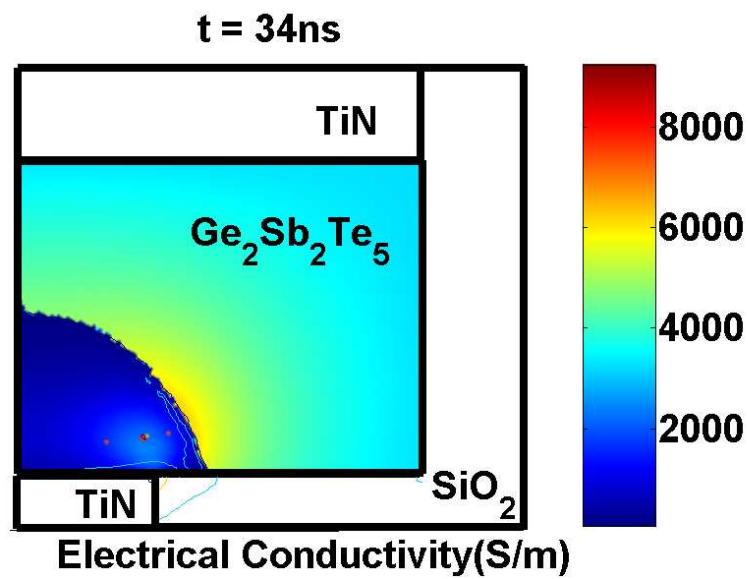
Figure 4.18: Electrical conductivity in the $Ge_2Sb_2Te_5$ layer during the SET at time t = 34ns. Observe the regions with electric field above threshold (Figure 4.17) exhibit a high electrical conductivity as expected in the ON state. In these regions the material is still (mostly) in amorphous state (Figure 4.14 (B)) at this time.
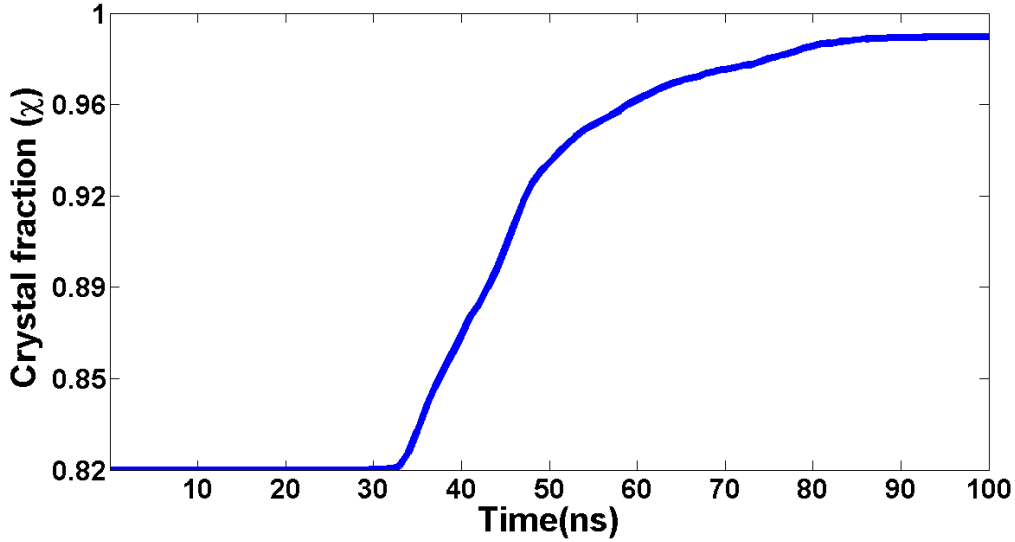
Figure 4.19: Crystal fraction ($\chi$) evolution of the $Ge_2Sb_2Te_5$ layer during the SET. The minimum value of the crystalline fraction is $\chi = 0.82$ corresponding to the initial state in Figure 4.14 (A). At time (t = 34 ns), $\chi$ starts to increase due to nucleation and growth of small clusters as seen in Figure 4.14 (B)-(F).The crystal fraction $\chi$, reaches equilibrium after the device starts to cool down (t $\approx$ 80 ns).

growth and dissociation events are plotted in Figures 4.20 and 4.21.

At the maximum amplitude of the pulse (t > 34 ns) small crystals start to form (as seen in the rates in Figure 4.20). In the period of time (30 ns < t < 50 ns) there is a rapid growth of the initial crystal formed as illustrated in the growth rates in Figure 4.20 and the corresponding Figures 4.14 (B)-(D). After this period of time the previously formed crystals continue growing at slower rate as can be seen by the increase of dissociation rates in Figure 4.20. By the time (t = 70 ns) the initial amorphous dome is almost fully crystalline, as shown in Figure 4.14 (D). The crystallization of the dome continues until the dome is fully crystalline (t $\approx$ 84 ns), which is also observed through the rapid decay in the rates in Figure 4.20.

Another important factor in the dynamics during the SET process is the number of crystals formed. In Figure 4.21 we illustrate the number of crystallites during the SET. The number of crystallites start to increase at (t = 30 ns); for the period of the time 30
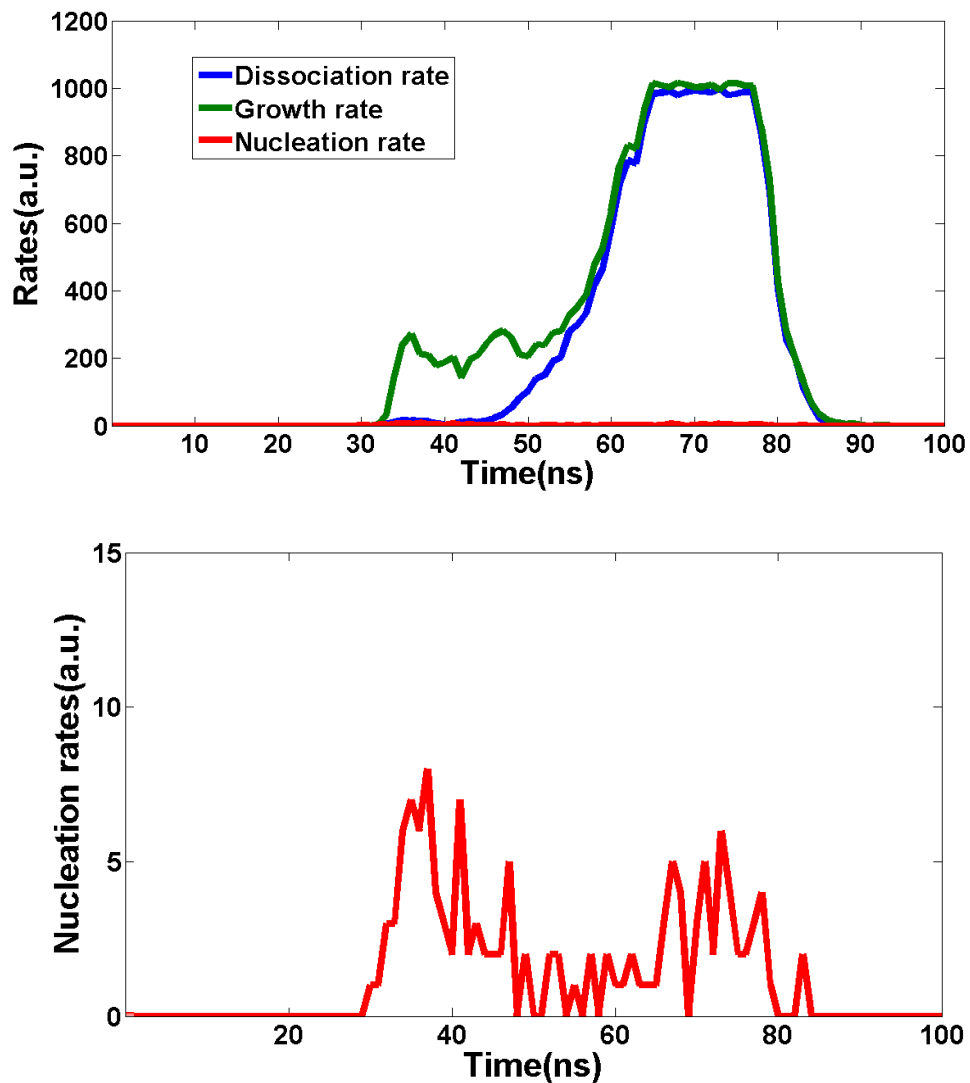
Figure 4.20: Rates of the different events as revealed by GCA algorithm for the SET process. The rates units are arbitrary. At time ($t \approx 34$ ns) there is an increase in the rates. Observe that nucleation is very low compared to growth and dissociation. For times 34 ns $<$ t $<$ 50 ns growth is much higher than dissociation. For t $>$ 50 ns, growth is slightly higher than dissociation. This explains the increase in the crystal fraction ($\chi$) seen in Figure 4.19. The bottom figure shows the nucleation rate during the SET process in a bigger scale. Observed nucleation rates are very low compared to growth and dissociation rates.
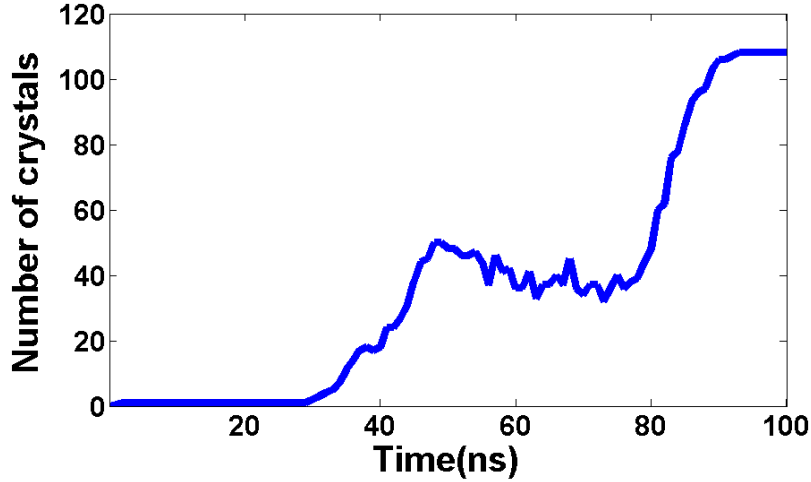
Figure 4.21: Number of crystal clusters with different orientations during the SET. The number of crystals clusters increase for time 30 ns < t < 50 ns. For time 50 ns < t < 80 ns we observe a slight variation. For t > 80 ns there is a second increase in the number of crystal clusters. This can be explained by the appearance of new crystalline sites at the top of the mushroom shaped dome in Figure 4.14 (E)-(F). For this second increase the device starts to cool down but temperatures are still high, as seen in Figure 4.15.

ns < t < 80 ns the number has only slight variations and afterwards, for t > 80 ns, a large increase the number is again observed. This increase can be explained by the small crystallites formed in the remaining amorphous regions in Figure 4.14 (D).

### 4.5.3   Repeatability of the simulations

The GCA approach used to simulate the phase transformation in the coupled physical model is a stochastic simulator. The temporal evolution in this stochastic model is based on an estimate of rates of possible local changes to the state of the systems [29, 110], utilizing a Gillespie algorithm [67, 68]. The time steps generated by the Gillespie algorithm correspond to the fastest rate requiring update. The time stepping in the Gillespie algorithm is defined using a random number [29, 110]. The stochastic simulator allows a random variation of the outcome over the time. This random variation might result in a different final crystalline state during the phase change transformations.
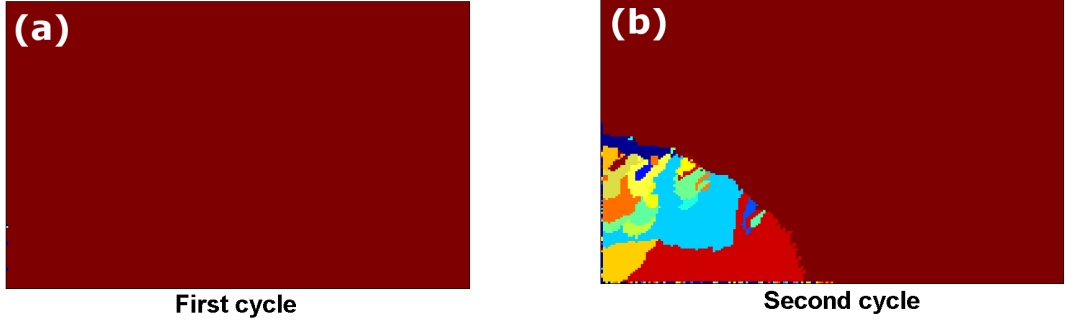
Figure 4.22: Comparison of the initial crystalline state for the first (a) and second (b) cycle in the RESET operation (Figure 4.22 (b) correspond to Figure 4.14 (F)).

In order to study the repeatability of the simulations within the developed model in this work, a comparison of the structural dynamics between the first and second reamorphization cycle is made.

The first amorphization cycle is made in analogue form to the RESET operation described in Section 4.5.1. For this first cycle the $Ge_2Sb_2Te_5$ is initially in a fully monocrystalline state. A pulse of 3 V with the trapezoid shape as shown in Figure 4.5, and duration 20 ns is used. For the second cycle the recrystallized dome is obtained through the SET operation (described in Section 4.5.2). One of the major differences between the first and second amorphization cycles is the initial crystalline state illustrated in Figure 4.22. This difference might lead to a RESET operation with a slightly different amorphous dome. The final amorphous dome obtained by this operation by applying the same pulse is illustrated in Figure 4.23. There is no representative difference observed in Figure 4.23 in the final phase for first and second cycle.

A more detailed comparison of the two different amorphization cycles is done by analyzing the evolution of the crystal fraction, nucleation, growth and dissociation rates. The crystal fraction evolution for the two different cases exhibits a slight variation as illustrated in Figure 4.24. In the second amorphization cycle the initial crystal fraction is smaller than in the first cycle. The difference is due to the fact that the previous SET process does not completely crystallize the amorphous dome, leaving tiny amorphous regions as observed in blue in Figure 4.22. The final crystal fraction also has a small
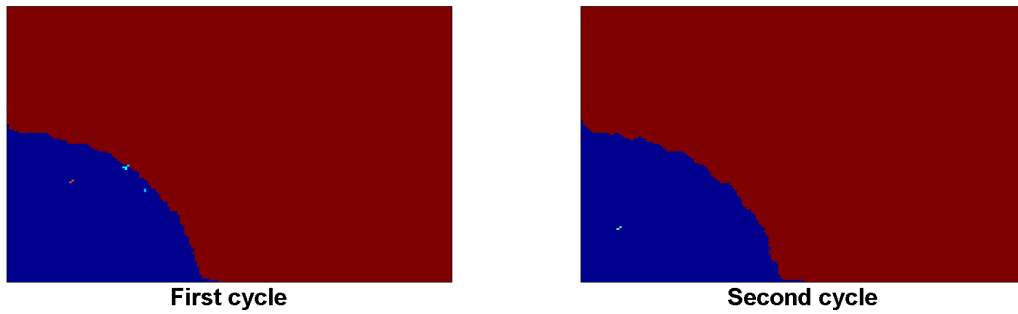
Figure 4.23: Comparison of the final state for the first and second cycle in the RESET operation. In the first cycle the initial state is a monocrystalline. The second cycle has a initial polycrystalline state.
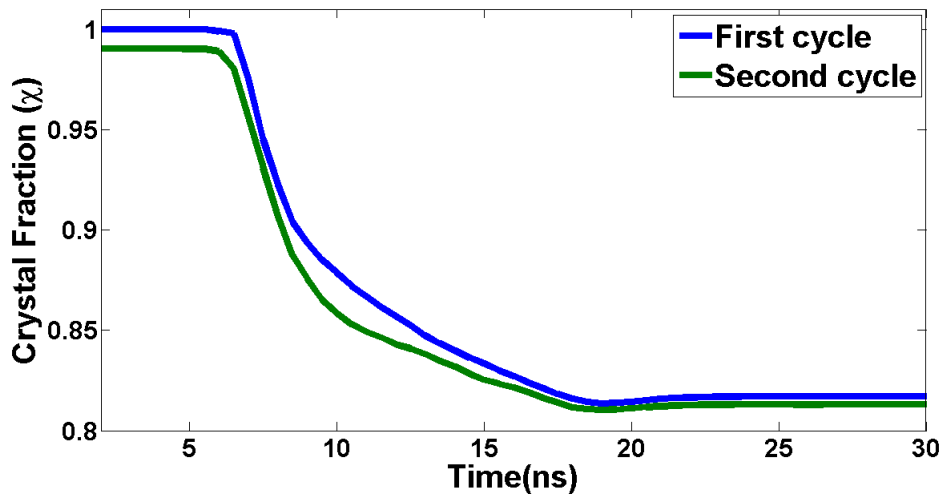


Figure 4.24: Comparison of the crystal fraction ($\chi$) evolution of the $Ge_2Sb_2Te_5$ layer during the RESET for the two different cycles. There is a slightly different initial crystal fraction $\chi$ for the second cycle. This is due to some amorphous sites remaining from the previously SET process (Figure 4.22). The overall evolution of the two cycles is, however very similar, as supported by the rates in Figure 4.25.

difference which might become important for a very large number of cycles and therefore increase the retention loss of amorphous (RESET) cells [90].

In the two different RESET cycles there is a slight variation in the dynamics of the structure as in Figure 4.25. This variation is noticeable in the growth rate at t $\approx$ 7 ns
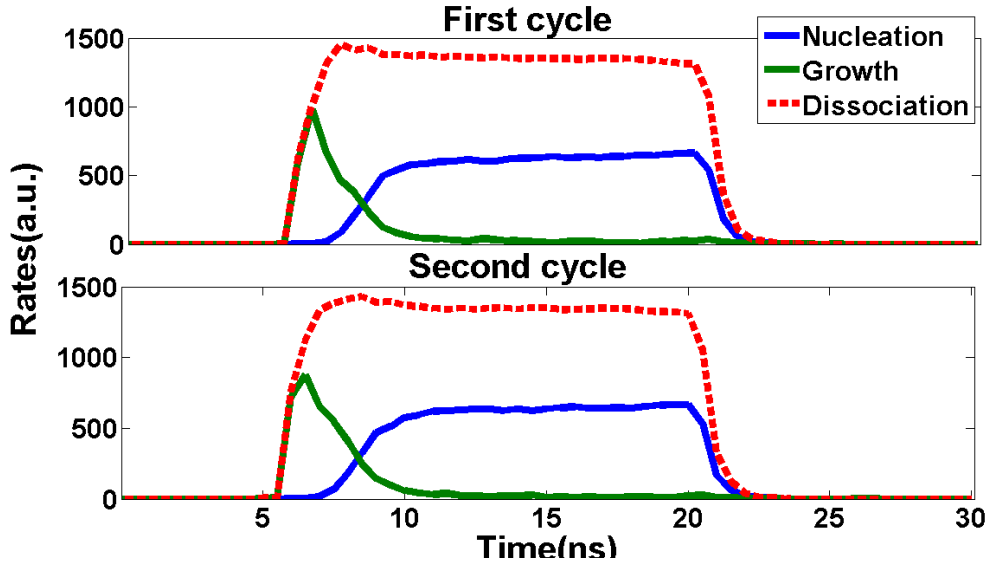
Figure 4.25: Rates of the different events of the $Ge_2Sb_2Te_5$ layer during the two different RESET cycles. The rates units are arbitrary. There is only a small difference at time t $\approx$ 7 ns for the growth rate.

(for example), but is nonetheless small.

The maximum and minimum temperatures in the $Ge_2Sb_2Te_5$ for the two different cycles behave in a similar fashion as is shown in Figure 4.26.

In addition to the study of the repeatability of the simulations RESET process we performed several simulations for the SET process in order to provide dispersion data for some of the most important parameters obtained by the GCA simulator (number of crystals, crystal fraction and resistance). The number of crystal obtained at the end of the SET process has a variance of $\sigma^2 = 24.21$ and standard deviation of $\sigma = 4.921$. Another important factor in the SET process is the full crystallization of the amorphous dome and this can be analyse by the crystal fraction. The crystal fraction ($\chi$) in the SET process has a variance of $\sigma^2 = 2.433 \times 10^{-3}$ and standard deviation of $\sigma = 0.0155$. The standard deviation of both parameters (number of crystals and crystal fraction) is very small indication that these values are clustered closely around the mean. Another very important parameter for the reliability of the PCRAM devices is the resistance obtained at the end of both of the process (SET and RESET). In the SET process the resistance has a variance of $\sigma = 4.66$ k$\Omega^2$ and standard deviation of $\sigma = 2.16$ k$\Omega$ while
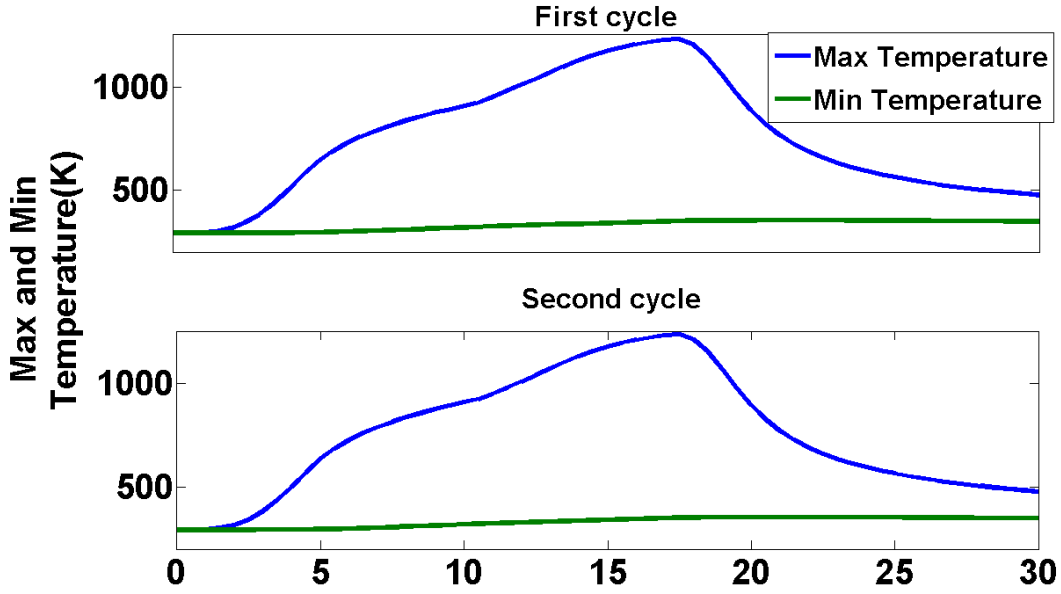
Figure 4.26: Maximum and minimum of the $Ge_2Sb_2Te_5$ layer temperatures during the two different RESET cycles. Observe these extreme temperatures behave in very similar fashion.

in the RESET process it has a variance of $\sigma = 6.03$ k$\Omega^2$ and standard deviation of $\sigma = 2.45$ k$\Omega$.

In summary, in this chapter we have developed a computationally efficient (simple and fast) numerical algorithm that simulates the electrical, thermal, and phase change dynamics in the PCRAM device during the SET and RESET switching operations. This numerical implementation integrates the Ielmini model for threshold switching. The implementation also incorporates a GCA approach for the phase transformations, which is capable of spanning the scales between atomistic methods and bulk scale methods. In fact, each site of our GCA approach represents the volume of a $Ge_2Sb_2Te_5$ monomer. In addition, the GCA approach can easily incorporate new features such as: anisotropy, extension to full 3D capability and the addition of an electric field term in the free energy term (see Chapter 7).

The obtained simulation results provide very useful insight into temporally and spatially resolved kinetics of device temperature, electric field distributions, and phase tran-

sitions. The values obtained for the device temperature and electric field distribution are in good agreement with published values. It has been shown that the phase change transformation strongly depends on the details of the electrical conduction in the $Ge_2Sb_2Te_5$ material. This dependence results in a localized crystallization behavior. In the SET process, it is also shown that the crystallization starts after the threshold field is reached. Threshold field values obtained for SET operations are in very good agreement with previously reported values. The developed simulation tool is expected to substantially contribute to the design of the future PCRAM cell geometries and advanced memory devices as it will be shown in Chapter 5. This simulation tool can be also used to investigate the effect of the pulse (shape and duration) on the phase change dynamics. More importantly it can also be used, as in the next chapter to simulate new applications of phase change devices, in particular their potential for arithmetic and neuromorphic computing.

# Chapter 5

# Accumulation-based arithmetic and neuromorphic computing with phase change materials and devices

In 1990 Carver Mead introduced the term "neuromorphic", defined as the artificial systems sharing organization principles with biological nervous systems. The organization in a brain is different than the organization in a computer. A brain works in parallel, has $10^{11}$ simple distributed computational and memory units, has dedicated point to point connections, is very power efficient, works in analog and continuous time, exhibits learning and is robust to errors. A computer, however, works in serial, has one powerful central CPU, the busses are shared by several components, it is not power efficient, works in discrete time and is sensitive to errors.

The two fundamental units in the formation of memory and learning are the neurons and the synapses. A human brain contains $\approx 10^{11}$ neurons, each with about $10^4$ highly complex interconnections between neurons (synapses) [111]. Neurons are electrical excitable cells which are able to respond to stimuli, conduct impulses and communicate to each other via synapses. The synapses connect axons and dendrites allowing rapid transmission of electrical and chemical signals. A typical neuron is formed by a soma, dendrites and axon as seen in Figure 5.1. The axon carries the output voltage (known as an action potential) of the neuron which is then received by the dendrite as a current
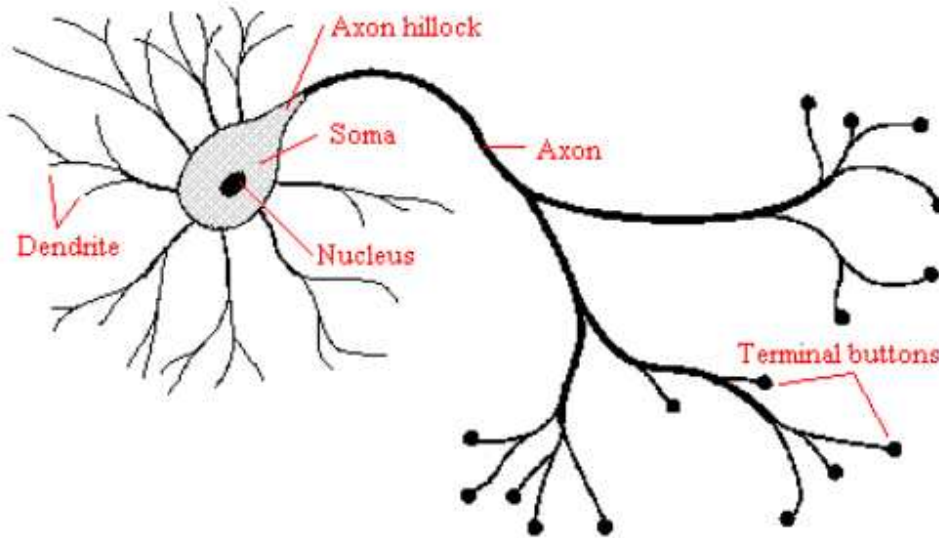
Figure 5.1: Structure of a biological neuron. Taken from [112]

input that flows to the soma and is integrated there. At the axon hillock an action potential is initiated as an integrated input current.

The synapses which give the parallelism, structural and robustness to the brain and are the key factors in perception and learning [113]. Therefore a huge amount of the research in neuromorphic computing focuses on emulating the functions and plasticity of biological synapses [112]. For this purpose CMOS architectures have been designed in the past [114] to emulate synapses. This synaptic behaviour has also been approached by the recent investigations of so-called memristor (memory resistor devices) [115, 116, 117, 118, 119]. Memristors are suitable for synapse realization due to their simple integration, analog memory and ultrahigh density of $10^{12}$ [120]. Similar to a biological synapse, the conductance of a memristor can be incrementally modified by controlling the charge or flux through it. Several other devices have been demonstrated to emulate biological synapses [121, 122, 123, 124, 125] . Phase change memories based on chalcogenide alloys were able to demonstrate a new single nanoscale device showing continuous transition between intermediate conductive states required for synaptic weight chance in biological synapses [112, 126, 127]. Phase change memory type devices have also recently been shown to be capable of implementing a simple form of integrate-and-fire neuron. This

neuronal application utilises a natural accumulation property inherent to phase change materials. This same, accumulation property can also be used to perform arithmetic computing.

This chapter explores the accumulation property exhibited by phase change materials and devices, in a continuous thin film material and in a "mushroom" type PCRAM cell. In this mushroom cell, we have implemented (in simulation) a base-10 accumulator for arithmetic applications by tailoring the input excitation amplitude and duration such that ten input pulses are required to convert the cell from the fully amorphous (or reset) state to the (almost) crystalline (or set) state. This accumulation property can provide a powerful form of arithmetic computing [128, 118]. Moreover, phase change accumulator cells process and store at the same physical location. A computer architecture in which processing and storage are carried out simultaneously and at the same location could offer very significant performance (speed and power) benefits over conventional approaches.

In section 5.3 we turn our attention to the use the accumulative property of phase change materials and devices to provide a particularly simple form of integrate-and-fire "neuron-like" behaviour. These further develop concepts which may become part of new compact computational architectures, based on dense arrays of artificial neurons and other novel signal processors [19].

## 5.1   Multistate memory in a continuous $Ge_2Sb_2Te_5$ thin film material using the GCA approach

The development and study of electrical phase change memories (PCRAM) in recent years has been made mainly for "conventional" binary data storage. Nevertheless, multistate memories are becoming more interesting since they offer greater storage capacity. For binary storage the aim is to ensure complete crystallization (and reamorphization) with a single (electrical or optical) excitation. For multilevel storage, we need to be able to reliably control the partial crystallization/amorphization of the phase-change material. In phase change devices it is possible to control the excitation voltage and current such that partial crystallization occurs at each excitation pulse. The final resistance of

the phase-change cell, after the application of an excitation voltage, will therefore depend on the form of this excitation (pulse amplitude and duration), the subsequent temperature distribution in the phase-change layer, the crystallization kinetics and the various electrical, thermal and physical parameters of the materials used in the cell/device design.

When crystallization has occurred the resistance of the cell changes from that in the purely amorphous phase, with the new resistance depending not only on the total fraction of crystallized material in the cell, but also on the spatial distribution of crystallization. Different crystalline fractions in the material might correspond to different resistance states.

Conventional cell structures such as the "mushroom" phase change element can be programmed to achieve multilevel recording by iterative programming techniques [13]. It was demonstrated that by varying the amplitude of the programming pulses or the trailing edge to control the evolution of temperature, 16 intermediate levels could be programmed. These techniques are based on the fact that the resistance of the phase change cell can be changed by applying pulses with different amplitudes. This results in a "U" characteristic curve where the resistance is measured as a function of the programming current. A typical "U" curve is shown in Figure 5.2. The right hand side of the characteristic "U" curve is obtained by applying pulses with larger amplitudes that result in melting of bigger volumes of the amorphous region (see Figure 5.3). The left hand side of the curve is obtained by applying pulses of lower amplitude or sequences of annealing pulses with appropriate magnitude to crystallize and shrink the size of the amorphous dome [129]. This characteristic curve was obtained for a "mushroom" phase change element with similar structure to that showed in Figure 4.3. The only differences with respect to the structure in Figure 4.3 are: a heater with a 200 nm diameter and a $Ge_2Sb_2Te_5$ layer of 150 nm thickness. Other elements in the geometry are equal in dimensions to Figure 4.3.

In this section the Gillespie Cellular Automata (GCA) approach, described in Section 2.5 and [29], is used to understand and to predict the detail of the phase transformation events that lie behind the multistate memory and phase change processor devices men-
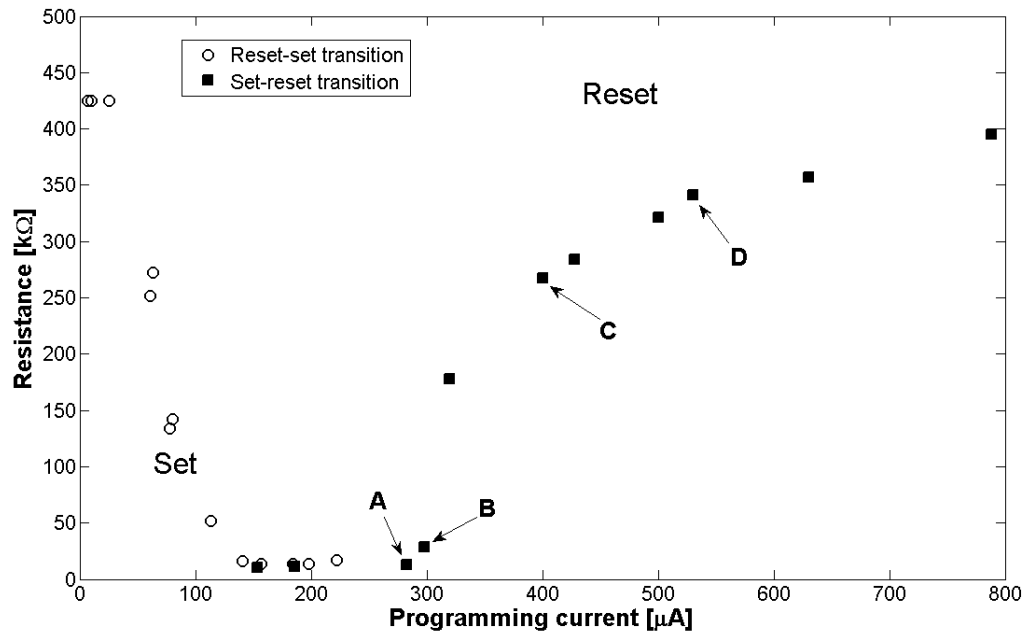
Figure 5.2: Typical R-I curve obtained by varying the current pulse amplitude for a mushroom PCRAM cell. Before the application of the programming pulse, an initialization pulse is applied to fully reset the cell. The circles correspond to the set process whereas the black squares correspond to the reset process. Programming currents with amplitude in the 0-220 $\mu$A range lead to annealing of the amorphous volume and a decrease in the cell resistance, while programming currents with amplitude in the range lead to melting of the active volume and an increase in the cell resistance.
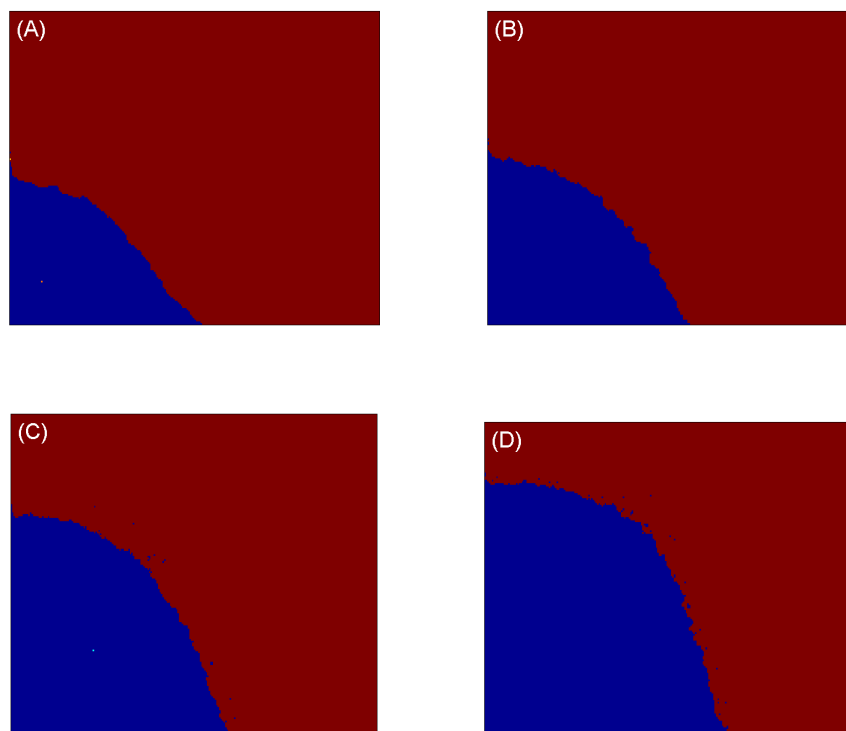
Figure 5.3: Phase distributions in correspondence with marks (A)-(D) in Figure 5.2. Larger amplitude pulses results in bigger volumes of the amorphous region.

tioned before. The work in this section concentrates on the simulation of a continuous $Ge_2Sb_2Te_5$ thin film behavior. The results presented in this section are for the commonly used $Ge_2Sb_2Te_5$ alloy. The $Ge_2Sb_2Te_5$ film layer simulated has an area of 120 nm × 150 nm which corresponds to the area of the phase change layer in the PCRAM structure in Chapter 4. The values used to evaluate the expressions in the GCA approach are as described in Section 2.5 and [29].

The left-hand side in the "U" curve corresponds to the energy accumulation mode explored through the results in Figure 5.4. The right-hand side can be explored by subjecting the cell to a higher temperature where the materials undergoes a transformation to a state between crystalline and amorphous (partial reamorphization). Figure 5.5 illustrates the results of the simulation with the details of the annealing temperatures. In this simulation the $Ge_2Sb_2Te_5$ phase change material was subjected to annealing at low and high temperatures. Firstly, at each low temperature anneal, the crystal fraction monotonically increases, hence "remembering" the previous step. This low temperature regime is called the energy accumulation regime, and can be seen as partial crystallization. Secondly, for high temperature anneals the crystal fraction moves to a given state bringing up the possibility to switch between successive crystalline states without complete resetting (partial re-amophization). Using this technique, 16 different states have been explored in experiments [130].

Figure 5.4 shows the result of the simulation when the initially amorphous material is subjected to successive annealing pulses. Each pulse is simulated by setting the temperature through on the sample cell at 430 $^oC$ for 60 ns with a separation of 940 ns. The sample was reset by the seventh pulse into the amorphous state by setting the temperature for this pulse at 930 $^oC$ for 60 ns. After resetting the cell, one cycle is finished and the cell has completely transformed into the amorphous state. This is repeated for 3 cycles. In a real phase change device, rather than applying temperature pulses, voltage or current pulses have to be applied where the heat is the result of a combination of thermal and electrical effects [130, 131]. In this section, the origin of heating is not considered, only its effects on crystallization. A monotonically increasing crystallized fraction with number of annealing pulses is illustrated in Figure 5.4. With each input temperature

pulse the phase change cell accumulates energy. The crystal fraction at each annealing pulse is in correspondence with a particular resistance in a real device. Therefore it would be straightforward to design a counter by monitoring the cell resistance at each pulse. Moreover, the annealing regime can be tailored in such a way that the percolation threshold is reached after $N$ pulses, providing a suitable arithmetic accumulator response (see Figure 5.6).

In this section the two regimes (accumulation and direct-overwrite) in the U characteristic curve have been explored. The results obtained using the GCA algorithm in a continuous $Ge_2Sb_2Te_5$ thin film support previous results obtained by Wright *et al* [61]. In the next section, we explore the accumulation regime in a real phase change device. Using this regime, both an arithmetic accumulator and a bio-inspired artificial neuron can be designed and implemented.

## 5.2 Accumulator-based phase change devices

Stanford Ovshinsky was the first to suggest the idea of using phase change materials for arithmetic computation [130], and recently Wright *et al* [126] demonstrated in the optical domain and on the (tens of) micrometer length-scale the successful execution of basic arithmetic operations. In this section, we design (in simulation) an accumulator response that can carry out remarkable range of arithmetic computations [118, 128].

As mentioned previously in the Section 5.1, "conventional" binary data storage in PCRAM is achieved by reversible switching between amorphous and crystalline phases using single pulses. For the RESET process, a relatively high amplitude and short duration pulse is used to form the amorphous phase, whereas for the SET process, a low amplitude and short and long duration pulse is used for the crystalline phase. There is a large resistivity contrast between crystalline (low resistivity) and amorphous (high resistivity) phases of the PCRAM cell. In the crystalline state the cell exhibits a low resistance (typically 10 k$\Omega$), while in the amorphous phase the cell exhibits a high resistance (typically $100s$ k$\Omega$ to M$\Omega$). To configure a phase-change device as an arithmetic "computer", we tailor the input pulse amplitude and/or duration such that the SET state is reached (from the RESET state) not with a single pulse (as for normal
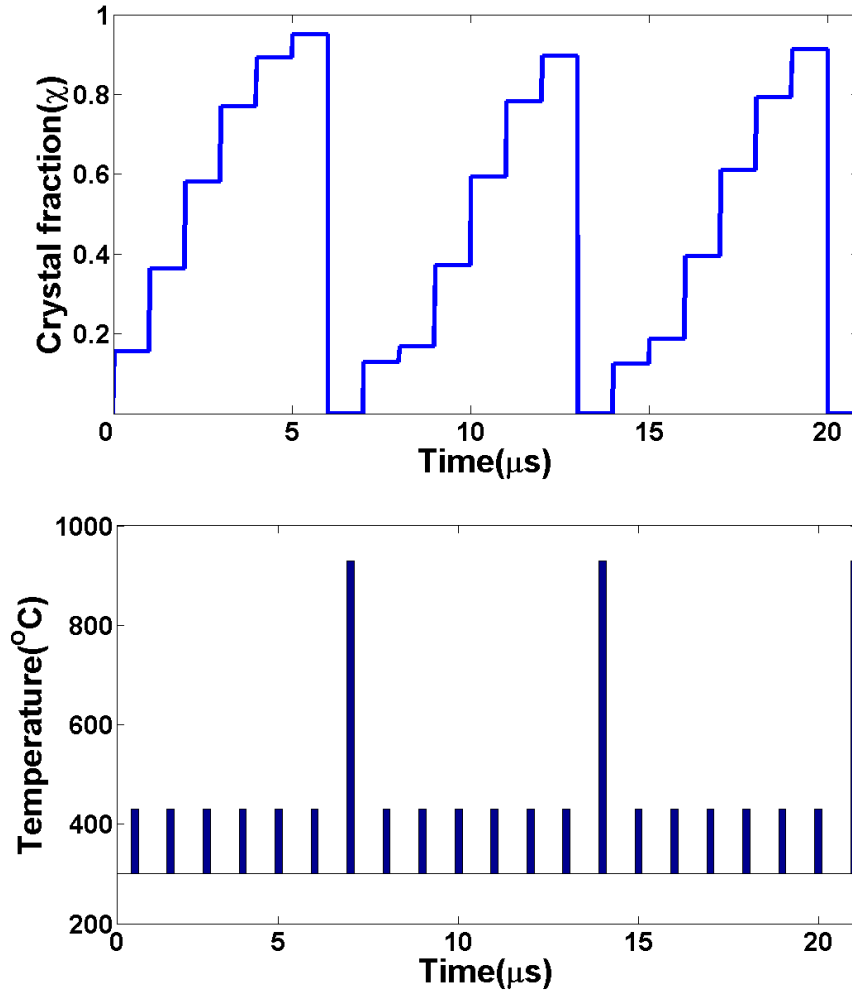
Figure 5.4: Crystal fraction ($\chi$) of a continuous $Ge_2Sb_2Te_5$ thin film as a function of the annealing pulses. In the simulation 3 cycles are reproduced. In each of the cycles, the first six pulses the temperature is set to 430 $^o$C for 60 ns with a separation of 940 ns. The seventh pulse reset the $Ge_2Sb_2Te_5$ sample by a pulse of 930 $^o$C for 60 ns. Observe a slight difference between the first cycle and the rest. The other two cycles exhibit very well defined levels. At the bottom, observe the temperature variation during the annealing.
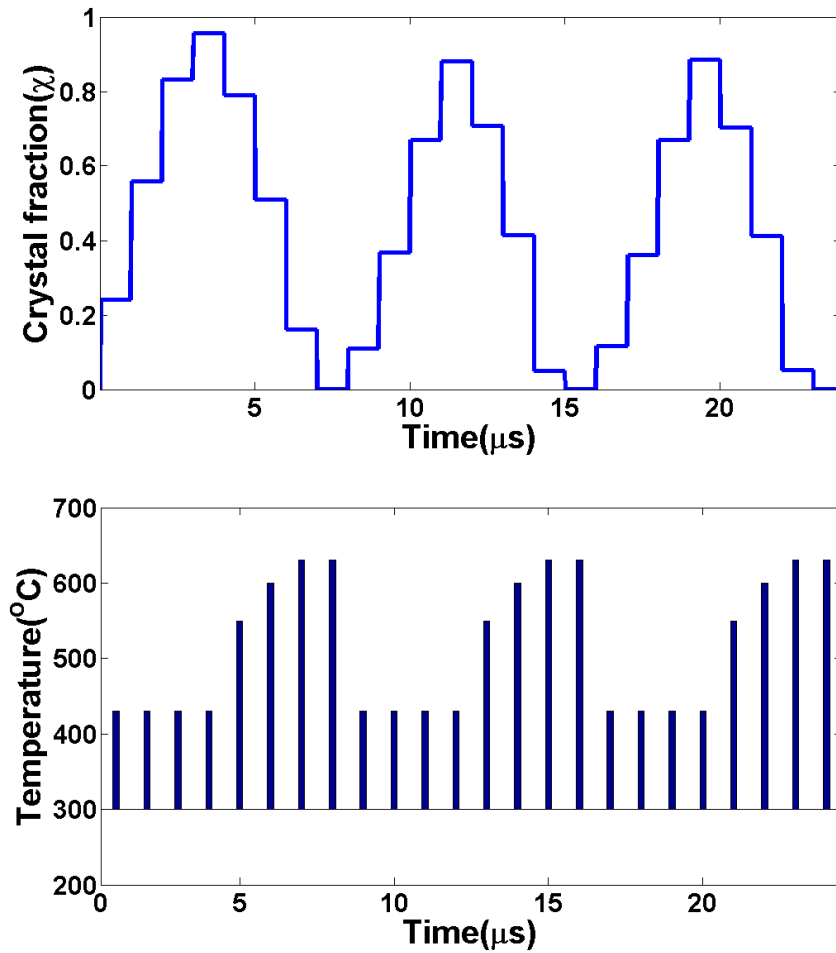
Figure 5.5: Crystal fraction ($\chi$) of a continuous $Ge_2Sb_2Te_5$ thin film as a function of the annealing pulses. In the simulation 3 cycles are reproduced. In each of the cycles, the first four pulses the temperature is set to 430 $^o$C for 60 ns with a separation of 940 ns. The fifth, sixth, seventh, eighth pulses the temperatures are set to 550, 600, 630, 630 $^o$C respectively with 60 ns duration and a separation of 940 ns. At the bottom, observe the temperature variation during the annealing.

binary memory operation) but with a pre-determined number of pulses. Each input pulse will be belong to the energy accumulation region in the left-hand side of the "U" curve in Figure 5.2.

The basic mechanism for implementing a phase change accumulator is shown in Figure 5.6 using a conventional "mushroom" type PCRAM cell. We have used the previously described "mushroom" phase change cell (Figure 4.3) to accumulate the input pulses. The parameter values for each of the elements in the cell are given in Table 4.1. The dynamics of the structure is the result of a complex sequence of events described previously by the GCA approach (Section 2.5) whereas the electro-thermal model remains the same as in Section 4.2 (Ielmini's model). In this instance we have implemented (in simulation) a base-10 accumulator by tailoring the input excitation amplitude and duration such that 10 input pulses are required to convert the cell from the RESET state to the SET state. For this sequence of pulses each pulse applied was identical, with amplitude 1.085 V and 60 ns in duration with a 20 ns falling and up edge. In comparison to this sequence of 10 pulses, a pulse of 1.5 V and duration of 60 ns (Figure 4.12 in Section 4.5.2), was required to completely switch the cell for conventional binary operation.

In the accumulation mode, the cell accumulates energy and eventually acquires enough energy to transform the active region from the fully amorphous starting phase to the crystalline phase. This is demonstrated in Figure 5.7 and Figure 5.8, where the state of the active region of the mushroom cell for the whole sequence of 10 pulses is shown. It can be seen that from state-1 to state-4 a few nuclei have formed in the middle of the amorphous "mushroom" dome, but this not cause a noticeable effect on the cell's resistance. Also, observe in Figure 5.7 that there is no prominent growth of the small nuclei from state-1 to state-4. After the input of the fifth pulse (state-5) a few more nuclei have formed and some are beginning to grow, with further growth clearly evident by state-9, but not enough to decrease the cell resistance to that of the fully crystalline value ($\approx 10$ k$\Omega$). Crystals formed at this stage have reached a bigger size, but they do not form continuous pathways between the top and bottom electrode. Between state-9 and state-10 there is a huge decrease in the resistance level, and by the state-10 the amorphous dome is almost fully recrystallized, as is observed in Figure 5.8. It should be

noticed that Figure 5.6 exhibits a high resistance "plateau" region that corresponds to the state-1 to state-7. In this "plateau" the states have essentially the same resistance values. Nevertheless, the states in the plateau region are different since each of them requires a different number of subsequent excitations pulses (i.e. different amounts of energy) to transform them to the SET state or to a resistance below the decision threshold (here set at 300 k$\Omega$). Hence, here we are not using the recording of information at different levels of resistance in the accumulation mode and this is not the same scheme as proposed for multilevel recording in PCRAM memories [132, 133, 134, 135] or for synaptic functionality [112, 125, 136]. In fact, an ideal accumulator, would have only two different levels of resistance, one for all the states from state-0 to state-(n-1) of a base-n system, situated above the decision threshold, and one for the state-n below the decision threshold. It is also important to mention that in arithmetic computing via accumulation does not require any special methods to combat the resistance drift that affects amorphous or partially amorphous cells [137]. In fact, the low-resistance end-point state of the accumulator (SET state) is substantially stable against resistance drift [133, 134]. In addition, pre-endpoint states will over time drift upwards in resistance causing an increase in the decision "window" between resistances above and below the decision threshold.

The system in Figure 5.6 provides a base-10 accumulator response using a single phase change cell. In this accumulator response, each input pulse transforms the phase change cell sequentially from state 1 to 9 (with the state "0" refers to the RESET state), and after the pulse 10 is applied, the cell "switches" to the low-resistance state (SET state). The "switches" to the low-resistance state can be detected by a simple measurement (to check that the resistance is below the decision threshold) and this resistance level we know that the count from 0 to 9 has been completed. It should highlighted that this is a non-volatile process: the phase change system will retain its existing state even when not powered and when power is re-supplied it will recommence from where it let off. With the accumulator response of the form of Figure 5.6 it has been experimentally demonstrated that arithmetic computations can be carried out in a efficient (in terms of the number of cells) and straightforward manner [128]. Moreover, in the phase change
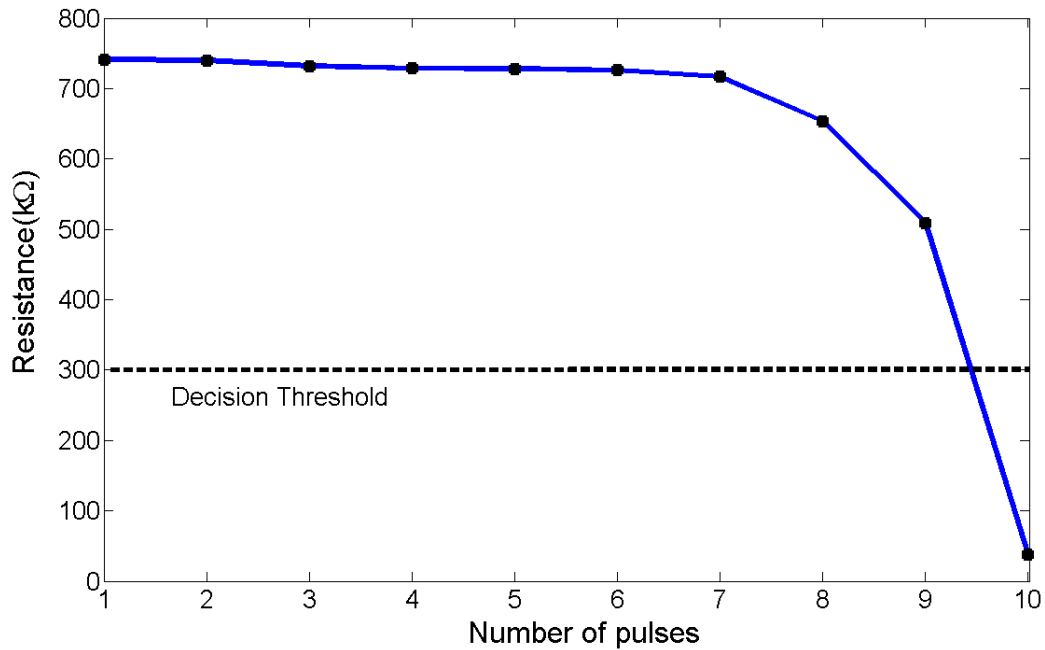
Figure 5.6: The resistance of the PCRAM cell after the application of each of 10 input pulses in a "mushroom" cell phase change memory device structure as in Figure 4.3. Each input excitation pulse was 1.085 V and 60 ns in duration with a 20 ns falling and up edge. This is the basic response for a base-10 accumulator. The first few pulses have insignificant effect of the device resistance ("plateau" region). Between state-9 and state-10 however there is a large decrease in resistance, and by state-10 the resistance is well below our chosen decision threshold of 300 kΩ.

accumulator cell, the computation and the storage are carried out simultaneously and at the same physical location which can provide a a powerful form of non-Von-Neumann computing.

## 5.3    Phase change integrate and fire neuron-like

Artificial neurons have been implemented as silicon neurons (SiNs) in VLSI (very large scale integration) electronic circuits that emulate electrophysiological behavior of real neurons and conductances [138]. Neural systems using silicon neurons operate in real-time at a speed independent of the number of neurons, and they are also very energy efficient. Hence there has been an increasing interest in design and fabrication of spiking neural network VLSI circuits [138, 139]. However, typically used simple neuron cells require approximately 20 transistors to implement low power adaptive neuron circuitry [140]. The number of transistors used can be reduced but at least four transistors are required for one artificial neuron [141]. Therefore a device that can reduce the number of elements used to reproduce the neuron properties can improve the design and development of electronic neural networks. In this section a single element device based on a mushroom-type phase change cell is suggested. The device is capable of mimicking a simple integrate-and-fire neuron, potentially enabling integration of a larger number of cells per chip as compared to conventional approaches.

The first step to construct a complex neuromorphic architecture system is to design bio-inspired element cells with neuron-like properties. From the functional point of view, artificial neurons can be described as circuits with one or more synapse blocks, responsible for receiving spikes from other neurons, and a soma block responsible for the integration of the input signals and the generation of the output analog action potentials and/or digital spikes [138]. In Figure 5.9, the scheme for the circuit of a typical integrate and fire neuron, is illustrated. In this general scheme, the neuron operates as follows: the integrator accumulates the output signals of the pre-synaptic cells. After reaching the threshold voltage the comparator generates the digitized signal, which is then processed by the spiking circuit and converted into a spiking signal. The generated spikes can be used either as a fed back to reinitialize the neuron or as input signal to feed a synapse.
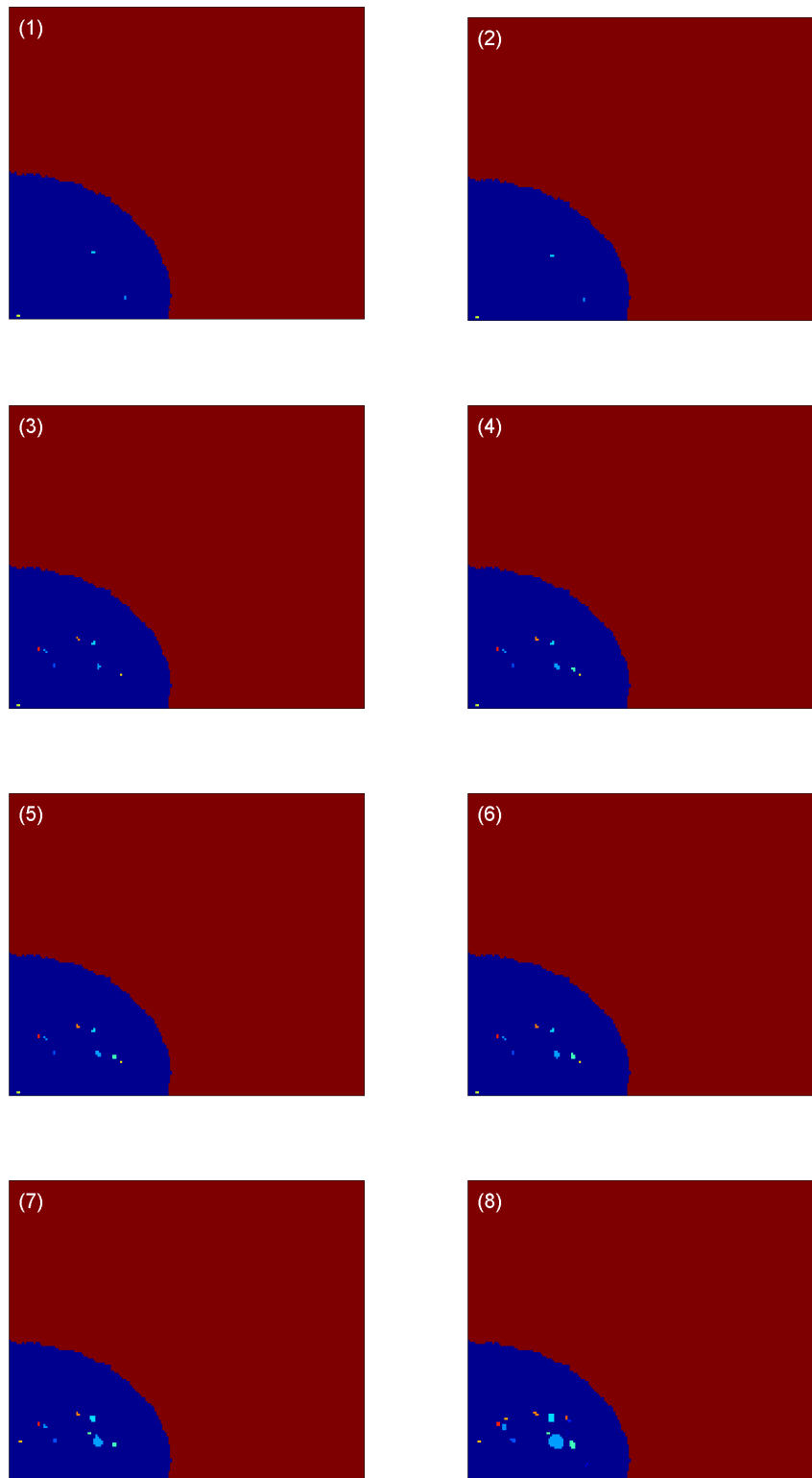
Figure 5.7: Crystal structure of the active region of the PCRAM cell for each state-0 to state-8 in the base-10 accumulator response of Figure 5.6. Each of the input excitation pulses in the sequence has an amplitude of 1.085 V and 60 ns duration, with a 20 ns falling and up edge. From state-1 to state-4 a few nuclei have formed. After the state-5 a few more nuclei have formed and they are begging to grow.
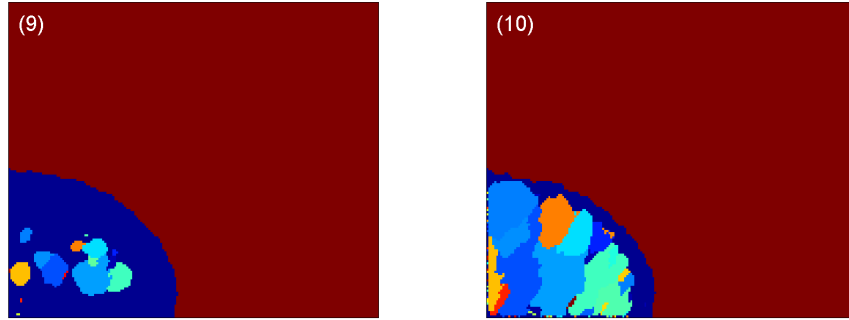
Figure 5.8: Crystal structure of the active region of the PCRAM cell for state-9 and state-8 in the base-10 accumulator response of Figure 5.6. Notice that at state-9 there is a clear evidence of growth in previously formed crystals. At the state-10 the amorphous dome is almost fully re-crystallized and the resistance is well below our chosen decision level of 300 kΩ, as observed in Figure 5.6.

The proposed accumulator neuron submodule is illustrated in Figure 5.10. The accumulator submodule is implemented using phase change materials technology. The phase change cell in the neuron circuit of Figure 5.10 accumulates excitations from the incoming pulse and "fires" (i.e. switches to a low resistance state), causing a high voltage output of the RC filter. Afterwards, this high voltage value of the filter it is used as input to the comparator, causing the comparator to switch. Then the comparator generates the digitized signal necessary to feed the spike circuit. To simulate this integrate and neuron behavior we used the 'mushroom" phase change cell and input pulses of Figure 5.6, a series resistance $R_1$ (in Figure 5.10) with a value chosen to be half of the PCRAM RESET resistance ($R_{RESET} \approx 750$ kΩ) and a reference voltage ($V_{REF}$) chosen for the comparator of $V_{READ}/2$. Thus the input to the comparator would be above $V_{REF}$ for the 9 pulses, but at the tenth pulse would fall below the reference, which will cause the comparator to switch. After switching the comparator will generate an output spike (via spike circuit). Note that $V_{READ}$ could be applied separately to the excitation pulses, or it could also be integrated by using a simple DC offset. The number of pulses required to produce the "fire" of the phase change neuron could be adjusted by varying the amplitude and/or duration of the pulses used. The system implemented in Figure 5.10 is considerably sim-
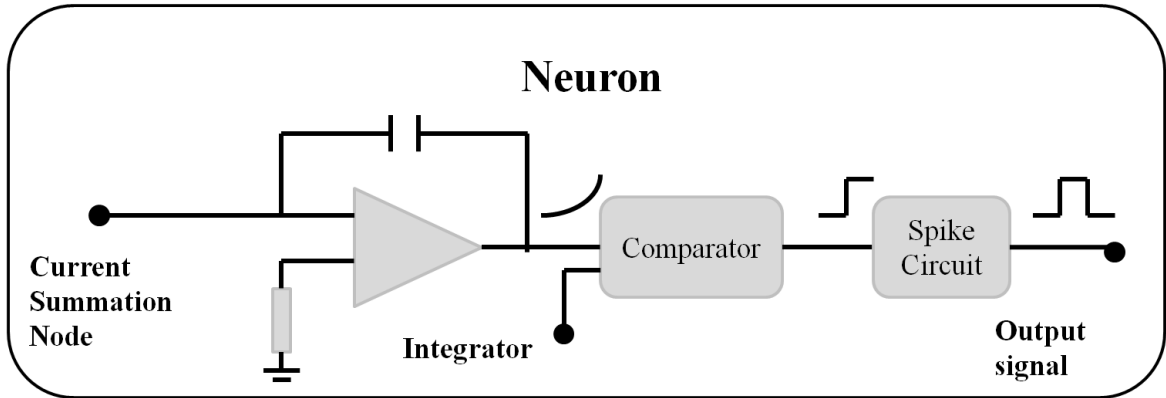
Figure 5.9: General scheme diagram of a typical neuron cell. Input signal from presynaptic cells are accumulated by the integrator. Once the threshold voltage is reached by the accumulator a digitized signal is generated and process in the spiking circuit. A full detailed scheme for the accumulation submodule is illustrated in Figure 5.10.

pler that conventional CMOS neurons that can require, depending on their complexity, typically 8 to 20 CMOS transistors to implement [138]. The output signals generated in the spike circuit can be used to feed the synapse as illustrated in Figure 5.11. Since phase change cells have also recently been shown to be capable, by using the multi-level resistance regime, of emulating a synaptic-like response [112, 124, 125] we can imagine phase change based neuro-synaptic systems. Furthermore, phase change materials can be scaled down to nanoscale dimension [142] and with potential cross-point architecture [143] reaching ultrahigh density and low power consumption and high speed (PCRAM cells have recently [144] been switched in 500 ps). Therefore, it may well be possible to design and build all-phase-change-based "brain-like" processing systems in which neuronal response is provided by a phase-change cell operating in the accumulation regime and the synaptic weighting by a phase-change cell operating in the multi-level resistance regime.

In this chapter, we have investigated multistate phase change memories in a continuous $Ge_2Sb_2Te_5$ thin film material using the previously introduced GCA approach. The model successfully predicts that both crystallization and amorphization (partial or
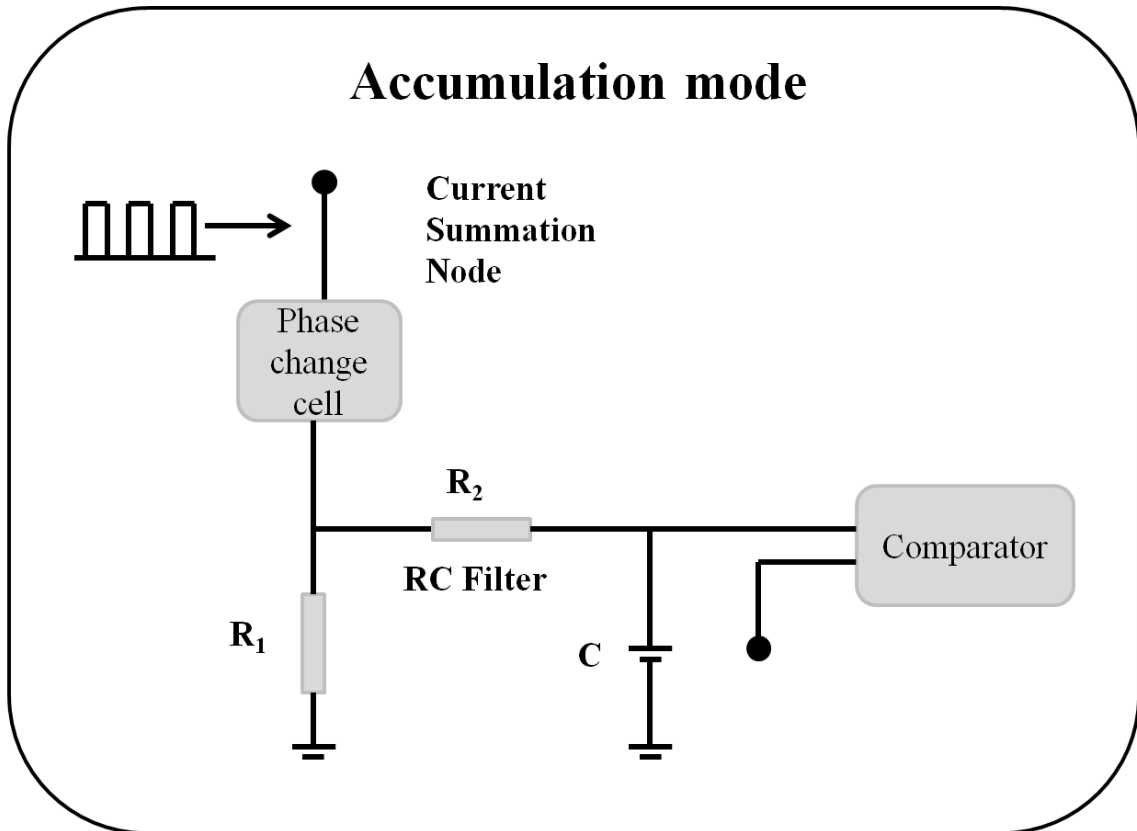
Figure 5.10: Scheme diagram for the accumulation submodule. Here the phase change cell allows us to reproduce accumulation mode. The phase change cell accumulates excitations from the impulses and "fires" (i.e. switches to a low resistance state). The switching of the phase change cell to a low resistance level, causes a high voltage output from the filter. Then the voltage output from the filter is compared to a reference voltage and a digitized signal is generated by the comparator.
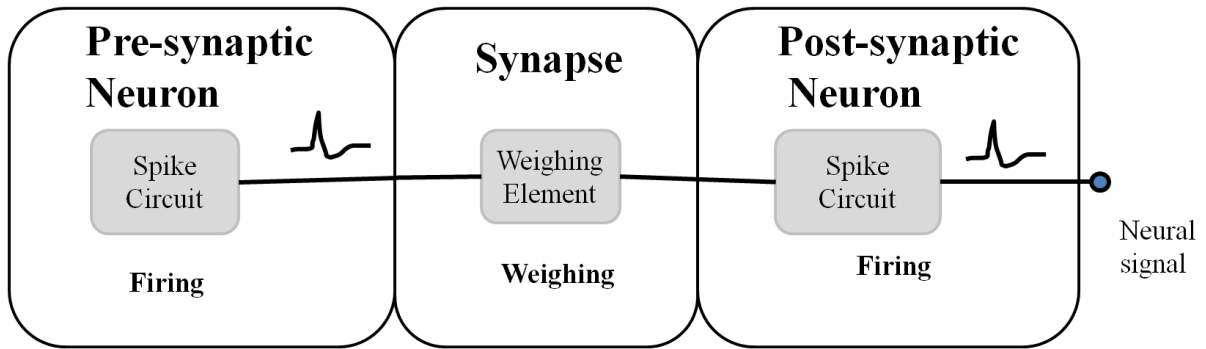
Figure 5.11: Schematic diagram of the interconnection between neurons and synapses. The spike circuit generates an output signal that feeds the synapse. This input signal change the resistance of the weighing element according to its amplitude and duration. The weighing elements can be mimicked using phase change technology as previously demonstrated [112]. In [112] PCRAM synapses are designed in a cross array architecture lying between prespike and postspike electrodes, corresponding to biologically inspired presynaptic and postsynaptic neurons.

complete) can be observed (dependent on the duration and temperature used for annealing), leading to two distinct operating regimes, namely energy accumulation and direct overwrite. We have also exploited the energy accumulation property, in a nanoscale electronic phase change device to provide a base-10 accumulator response. The accumulator response of our system can provide a powerful form of arithmetic computing [128]. The phase-change accumulator cell both calculates (processes) and stores the result of such computations simultaneously in the same cell, potentially providing a powerful form of non-Von-Neumann computing. This accumulator response does not require any special methods to combat the resistance drift. We also show that this same accumulation property can be used to provide a particularly simple form phase-change integrate-and-fire "neuron" which in addition to the already demonstrated phase change synapse might open a new route to the realization of all-phase change neuromorphic computers.

# Chapter 6

# Relaxation oscillations in phase change devices

Electric transport properties of phase change materials are influenced by the generation and recombination processes of nonequilibrium charge carriers [30, 145]. In the field of semiconductors, nonlinear generation and recombination processes [146] can give rise to nonequilibrium phase transitions. These transitions manifest as electrical instabilities, such as threshold switching between a nonconducting and a conducting state, spontaneous oscillations of the current or voltage and nucleation and growth of filaments if sufficiently high electric fields are applied. Generation and recombination induced phase transitions were first studied by Landsberg *et al* [147]. The introduction of concepts and methods from nonlinear dynamics has stimulated a large amount of work in complex spatio-temporal dynamics of filaments, spatio-temporal chaos and higher bifurcations [146, 148].

In phase change materials, relaxation oscillations have been experimentally observed by Schmidt and Callarotti for $1\mu m$ thick films of $Te_{40}As_{35}Ge_7Si_{18}$ subjected to various applied dc bias voltages with different values of series load resistances [149]. In their work they found a linear dependence of the relaxation oscillations with load resistance up to a maximum resistance, where the oscillations ceased. The mechanism proposed for threshold switching was that above a threshold voltage, a conductive filament formed in the high resistance amorphous phase. After a simple circuit analysis it was possible to

calculate the oscillation period, which was in good agreement with their experimental data. In a later work, Carollati et *et al* [150] investigated the nonlinear period of the relaxation oscillations dependence on the nonlinear amorphous state resistance.

More recently relaxation oscillations were experimentally observed in $Ge_2Sb_2Te_5$ devices [97, 151]. Ielmini *et al* [151] measured circuit-controlled relaxation oscillations under various applied voltage pulses.

In addition to the experimentally measured relaxation oscillations the mechanism of such oscillations was explained by Karpov *et al* [97] in the framework of field induced nucleation.

In this chapter we present a brief study of relaxation oscillations in $Ge_2Sb_2Te_5$. Firstly, a model that correctly predicts threshold switching is analyzed under the assumption that threshold switching is due to the generation and recombination of charge carriers. In this model we have to include a parasitic inductance to correctly model the oscillations. At the end we also introduce a simple phenomenological model of the $V - I$ characteristic curve that exhibits threshold switching. With this simple model we also obtained oscillations for phase change materials.

## 6.1 The Ielmini model for threshold switching

We recall the threshold switching model of Ielmini *et al* [152, 95, 30] (and which we previously presented in Section 3.2) before discussing the appearance of electrical relaxation oscillations in a phase change device [152]. In doing so we will explicitly include the dependence of the current on the voltage through the device.

From Section 3.2 we assume that the phase change material separates into two electrically different layers - an "OFF" layer and an "ON" layer. In this model, the collapse of the field in the "ON" layer is the basis of the voltage decrease for currents above threshold switching point, which results in the negative differential resistivity (NDR) regime of conduction and hence threshold switching [95]. Negative differential resistivity (NDR) is defined as the region where

$$R_n := \frac{dV}{dI} < 0,$$ 

(6.1)

According to this assumption the current in the threshold switching region can be calculated with equation (3.4), where $\gamma$ is the nonequilibrium term for the "ON" layer as in equation (3.5) and the constant $B_{12}$ is defined by equation (3.6). Details of the meanings of the quantities in equations (3.4), (3.5) and (3.6) are given in Section 3.2 and [152, 95, 30].

From the current $I$ the field in the "OFF" region can be calculated by the inverse of equation (3.4) and [95, equations (3,4)] as:

$$\mathcal{F}_0(I_c) = \frac{2kT}{qd} \operatorname{asinh} \left[ \frac{\tau_0 \exp[(E_C - E_F)/(kT)]}{2qdA(N_{T1} + N_{T2})} I_c \right] \tag{6.2}$$

The excess trap density in the "ON" layer is governed [95, equation (5)] by a fast timescale process

$$\frac{d\delta}{dt} = G(I_c) - \delta/\tau_n, \tag{6.3}$$

where we assume the injection from the "ON" region [95, equations (4,6)] is

$$G(I_c) = \frac{N_{T1}}{\tau_0} \exp \left[ -\frac{E_{T1} - E_F}{kT} \right] \exp \left[ -\frac{B_{12}}{F_0(I_c)} \right].$$

We can adiabatically eliminate $\delta$ to obtain

$$\delta(I_c) = \tau_n G(I_c). \tag{6.4}$$

Note that the slow manifold corresponding to the solution (6.4) of equation (6.3), is uniformly and strongly stable everywhere, meaning that this elimination is valid as long as the timescale $\tau_n$ is much faster than other processes in the equations.

Hence the "ON" field can be written [95, equations (3,4)] as

$$F_1(I_c) = \frac{2kT}{qd} \operatorname{asinh} \left[ \frac{\tau_0 \exp[(E_C - E_F)/(kT)]}{2qdA(N_{T1} + N_{T2}) + \delta(I_c) \exp[(E_{T2} - E_{T1})/(kT)]} I_c \right] \tag{6.5}$$

According to [95, equation (7)], we can now find the thickness of the "OFF" and "ON" layers respectively using

$$u_{0,a}(I_c) = \min \left[ u_a, \frac{E_{T2} - E_{T1}}{qF_0(I_c)} \right], \tag{6.6}$$

$$u_{1,a}(I_c) = u_a - u_{0,a}(I_c). \tag{6.7}$$

If $I_c$ has opposite polarity, we assume layers form in the opposite order, but their dependence on $I_c$ will be the same; hence

$$0 \leq u_{0,a}, u_{1,a} \leq u_a. \tag{6.8}$$

From [95, equation (8)] we find the total voltage across the PC cell is

$$V(I_c) = F_0(I_c)u_{0,a}(I_c) + F_1(I_c)u_{1,a}(I_c) + R_s I_c, \tag{6.9}$$

where $R_s$ represents a series resistance of the electrodes in the PC device and $V$ has contributions from the two layers ($u_{0,a}$ and $u_{1,a}$).

Note, however that $V(I_c)$ as in (6.9) is a single-valued continuous function of $I_c$. However, $V(I_c)$ is not invertible in the region of interest and this can give rise to a "threshold switching" effect. Note also $V(I_c)$ is not a smooth function -it does not have a derivative at all points, owing to the saturation of $u_{0,a}$ for low values of $I_c$ -and hence there will be a discontinuity of the derivative when $u_{0,a}$ reaches its maximum value $u_a$, i.e., from equation (6.6) when

$$E_{T2} - E_{T1} = qF_0(I_c)U_a.$$

## 6.1.1 Parameters

The parameters we use are essentially the same as those given in [95, 152]. We assume that T = 300 K so that kT = $4.0463 \times 10^{-21}$ J, the mean inter-trap spacing is d = $5 \times 10^{-9}$ m, the energies of the various states are $E_C - E_F = 5.6 \times 10^{-20}$ J, $E_{T1} - E_F = 0$ and $E_{T2} - E_{T1} = 5.44 \times 10^{-20}$ J. The relaxation times are $\tau_n = 10^{-9}$ s, and $\tau_0 = 10^{-15}$ s; note that $\tau_0 \ll \tau_n$. All these parameters are in Table 4.1, Section 4.2. The Fowler-Nordheim coefficient that governs tunnelling from the deep to the shallow wells is assumed to be $B_{12} = 10^9$ Vm$^{-1}$, while the carrier densities are assumed to be $N_{T1} = N_{T2} = 10^{25}$ m$^{-3}$. For the electron charge, recall that $q = 1.6 \times 10^{-19}$ C. We consider a phase change cell with thickness $u_a = 2.4 \times 10^{-8}$ m and contact area $A = 2 \times 10^{-14}$ m$^2$ (in [95] the value of the contact area was taken as $A = 1 \times 10^{-15}$ m$^2$).
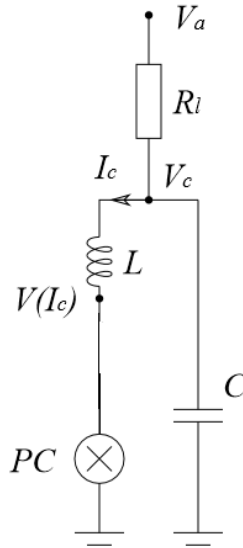
Figure 6.1: Circuit showing a PC cell with a parallel capacitance $C$, a load $R_l$ and a parasitic inductance $L$. For certain input voltages $V_a$ the circuit can generate self-sustaining oscillations.

## 6.2 Relaxation oscillations caused by threshold switching

Consider first the circuit in Figure 6.1 in the case of the inductance $L = 0$. In this case there is one degree of freedom (cf [152, equation (5)]) and

$$\frac{dV}{dt} = \frac{1}{C} \left[ \frac{V_a - V}{R_l} - I_c \right]. \tag{6.10}$$

The lack of a single-valued inverse $I_c(V)$ means that this differential equation can only be solved implicitly and it will hit singular points where $dV/dI = 0$; at these points there will be no unique way of continuing the solution, even if we re-instate the equation (6.3). Note however, that a well-designed ODE solver may successfully resolve the singularity by switching to a different stable value of $I_c$ and continuing this, and it is likely that the oscillations seen in [152] are a result of an artifact of the numerics.

A more robust way to regularize the equations is to include a parasitic inductance as shown in Figure 6.1 and where $0 < L \ll 1$. The current and voltage [153, 154, 155] are

now described by:

$$\frac{dI_c}{dt} = \frac{(V_c - V(I_c))}{L}$$

$$\frac{dV_c}{dt} = \frac{1}{C}\left[\frac{V_a - V_c}{R_l} - I_c\right], \tag{6.11}$$

and give a regular system where switching may occur and the timescale is limited by the parasitic inductance. Figure 6.2 illustrates the case where

$$R_l = 20k\Omega, \quad R_s = 1k\Omega, \quad V_a = 1.2V, \quad L = 100nH, \quad C = 10pF \tag{6.12}$$

such that the capacitor slowly charges with the PC device in its "OFF" state then
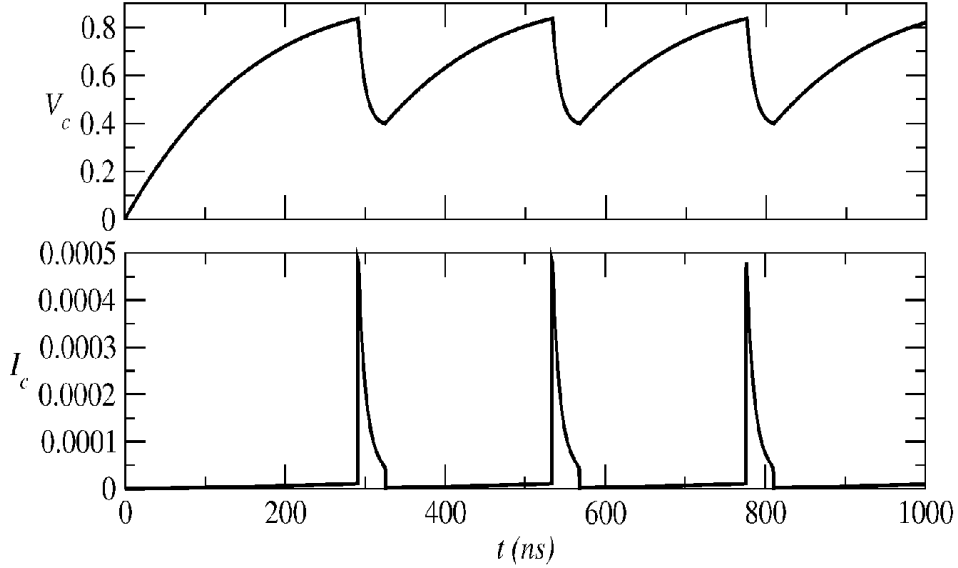


Figure 6.2: Time series, showing relaxation oscillations within the circuit of Figure 6.1 using the model for threshold switching in equation (6.9) and a parasitic inductance.

slowly discharges as the device very rapidly switches to its "ON" state. Note that the fact that the two equations (6.11) are very stiff means that one needs to be careful to choose a suitable integrator and a fairly small timestep to resolve the dynamics. In this case we used $dt = 0.002$ ns as the timestep and the stiff integrator in xppaut [156]. The complete code in xppaut can be found in Appendix B.

Oscillations can appear as switching and recovery dynamics in the phase change material [151]. By applying a bias voltage $V_a$ higher than the holding voltage $V_1$ a

post-switching current suddenly rises to a point in the "ON" state. This transition to the "ON" state occurs almost at constant voltage since the characteristic time for the capacitor discharge is very long compare to the switching time [151]. After discharging the capacitor, the voltage relaxes and the current falls below the holding current $I_2$ i.e., the minimum current to hold the "ON" state [157]. Thus the system returns to the "OFF" state. Afterwards the voltage rises until threshold switching is reached and a new cycle starts.

## 6.3  A simplified model for threshold switching

The threshold switching model of Ielmini *et al* [152, 95, 30] and also in Section 6.1 depends on a huge number of parameters, some of them are difficult to calculate and/or measure experimentally. In this section, we propose a simpler model based on a combination of transcendental functions that produce similar results to the threshold switching model of equation (6.9). Thus

$$V(I) = V_h \tanh(\mu I)(1 + \alpha \text{sech}^2(\mu I)) + R_s I \qquad (6.13)$$

with the parameters and their description as:

- $V_h$ represents a holding voltage (i.e., the minimum voltage to hold the low-resistance region called the "ON" state).

- $1/\mu$ refers to a switching threshold current.

- $\alpha$ is a a dimensionless parameter that describes the voltage overshoot.

In contrast to the model in equation (6.9), the model of equation (6.13) only depends on a small number of parameters $(V_h, \mu, \alpha)$.

Figure 6.3 depicts the $V(I)$ function described by equation (6.13). The high resistance region corresponding to the "OFF" state of the switch is characterized by the threshold voltage $V_1$ with current $I_1$. The low resistance region corresponding to the "ON" state is characterized by a minimum holding current $I_2$ with voltage $V_2$. The region with
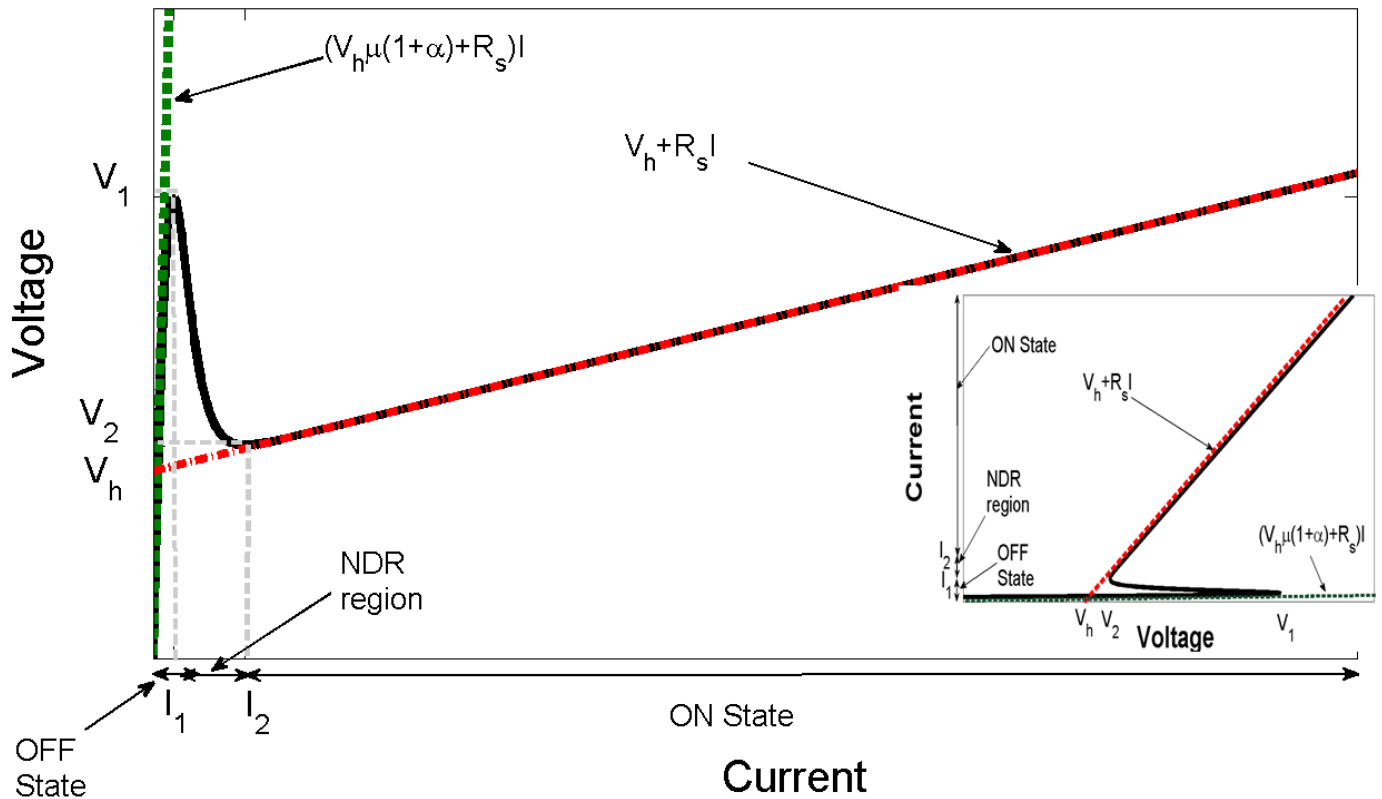
Figure 6.3: The voltage-current $V(I)$ curve from equation (6.13) in black and its asymptotic lines $(V_h \mu(1 + \alpha) + R_s)I$ and $V_h + R_s I$ in green and red respectively. The "OFF" state is characterized by a high resistance whereas the "ON" state corresponds to a low resistance. Above threshold switching is the negative differential resistivity (NDR) region defined by equation (6.1). The critical points for the function $V(I)$ are labelled $(I_1, V_1)$ and $(I_2, V_2)$ where $V_1$ is the threshold voltage with current $I_1$, and $I_2$ is the holding current with voltage $V_2$. In the right hand side, the small box the $I - V$ curve is shown in the usual way.

negative resistance corresponds to the negative differential resistance (NDR) as defined in (6.1).

The function $V(I)$ in equation (6.13) passes through a maximum and minimum that can be obtained by solving

$$\frac{dV}{dI} = V_h \mu (1 - 2\alpha) \mathrm{sech}^2(\mu I) + 3 V_h \mu \alpha \mathrm{sech}^4(\mu I) + R_s = 0. \tag{6.14}$$

Let us introduce $x$ as

$$x = \mathrm{sech}^2(\mu I). \tag{6.15}$$

Thus equation (6.14) can be rewritten in the form

$$V_h \mu (1 - 2\alpha) x + 3 V_h \mu \alpha x^2 + R_s = 0, \tag{6.16}$$

with solutions of the form

$$x_{1,2} = \frac{V_h \mu (2\alpha - 1) \pm \sqrt{(V_h \mu (2\alpha - 1))^2 - 4(V_h \mu)(3\alpha)(R_s)}}{2(V_h \mu)(3\alpha)}, \tag{6.17}$$

where $x_{1,2} > 0$ if and only if $V_h \mu (2\alpha - 1) > \sqrt{(V_h \mu (2\alpha - 1))^2 - 4(V_h \mu)(3\alpha)(R_s)}$. Therefore $x_{1,2} > 0$ if and only if $12 V_h \mu \alpha R_s > 0$ (which follows from assuming $V_h, \mu, \alpha > 0$). As $x_{1,2} > 0$ it is possible to solve equation (6.15) for $I \in R$ giving

$$I_{1,2} = \mathrm{sech}^{-1} \left( \left( \frac{V_h \mu (2\alpha - 1) \pm \sqrt{(V_h \mu (2\alpha - 1))^2 - 4(V_h \mu)(3\alpha)(R_s)}}{6(V_h \mu)(\alpha)} \right)^{1/2} \right). \tag{6.18}$$

The values of the current $I_{1,2}$ are used to calculate their corresponding voltage $V_{1,2}$ with equation (6.13) obtaining

$$V_{1,2} = V(I) = V_h \tanh(\mu I_{1,2})(1 + \alpha \mathrm{sech}^2(\mu I_{1,2})) + R_s I_{1,2}. \tag{6.19}$$

By substituting of the values in Table 6.1 into (6.18) and (6.19), we calculate the points $(I_1, V_1)$ and $(I_2, V_2)$ to be $I_1 = 9.2619\ \mu A$, $I_2 = 42.031\ \mu A$, $V_1 = 0.8512$ V and $V_2 = 0.3920$ V.

Very good agreement with this simplified model (6.13) and the model [95] in Section 6.1, as can be observed in Figure 6.4.
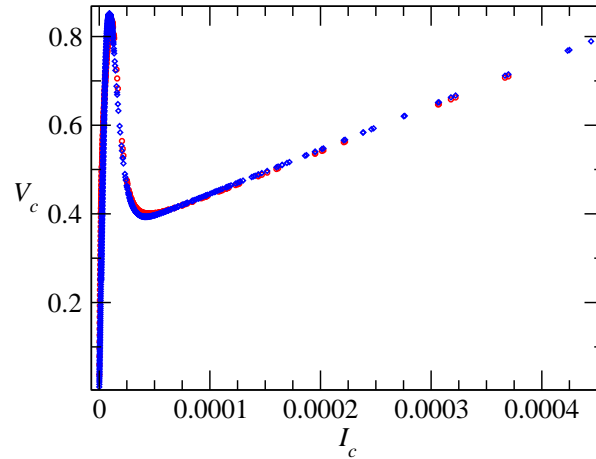
Figure 6.4: Comparison of the calculated $V$-$I$ curves for the two different models: the electronic model from equation (6.9) and the simple model in equation (6.13) in blue and red respectively, with fitted parameters as in Table 6.1.

| | |
|---|---|
| $V_h$ | 0.345 V |
| $\mu$ | 81571 A$^{-1}$ |
| $\alpha$ | 4.761 |

Table 6.1: Fitted values for the simple model (6.13) to the [95] model, as illustrated in Figure 6.4.

## 6.4 Relaxation oscillations in the simplified model for threshold switching

The phase diagram of the relaxation oscillations with the simple model for threshold switching of equation (6.13) is illustrated in Figure 6.5. The curve in blue corresponds to the threshold switching curve model of equation (6.13), whereas in green is the bias load line. The region where oscillations occur is highlighted in red. The set of points $(I_{min}, V_{max})$ and $(I_{max}, V_{max})$ help us to completely describe this region. The region where oscillations occur is delimited by the lines between the points $(I_1, V_1)$, $(I_{max}, V_{max})$, $(I_2, V_2)$ and $(I_{min}, V_{min})$. Clearly $V_{max} = V_1$ , $V_{min} = V_2$, where $V_1, V_2, I_1, I_2$ were determined in Section 6.3 in equation (6.19). The maximum current $I_{max}$ and the minimum current $I_{min}$ are found by the intersection of the line $V(I) = V_{max} = V_1$ and $V(I) = V_{min} = V_2$ with the asymptotic lines depicted in Figure 6.3. More specifically, $I_{max}$ is at the intersection of $V(I) = V_{max} = V_1$ and $V_h + R_s I$, i.e.

$$I_{max} = \frac{V_1 - V_h}{R_s} \tag{6.20}$$

In an analogous way the minimum current $I_{min}$ is found at the intersection $V(I) = V_{min} = V_2$ with $(V_h(1 + \alpha) + R_s)I$ giving:

$$I_{min} = \frac{V_2}{V_h \mu (1 + \alpha) + R_s}. \tag{6.21}$$

Using the fitting values in Table 6.3 the maximum and minimum currents are $I_{min} = 2.4032$ $\mu$A and $I_{max} = 506.20$ $\mu$A.

As mentioned above, relaxation oscillations are found to occur by biasing the phase change materials in the circuit in Figure 6.1 with a *DC* power supply of magnitude $V_a$ and a series resistance $R_l$ such as the load line does not intersect the "ON" or the "OFF" state [149, 152, 157, 150] as illustrated in Figure 6.5. The *DC* load line is described by

$$V(I) = V_a - I R_l \tag{6.22}$$

Therefore the load line has to intersect the $V(I)$ curve in the NDC region. This can be easily calculated to find a range of values for the load resistance $R_l$. Thus, the load
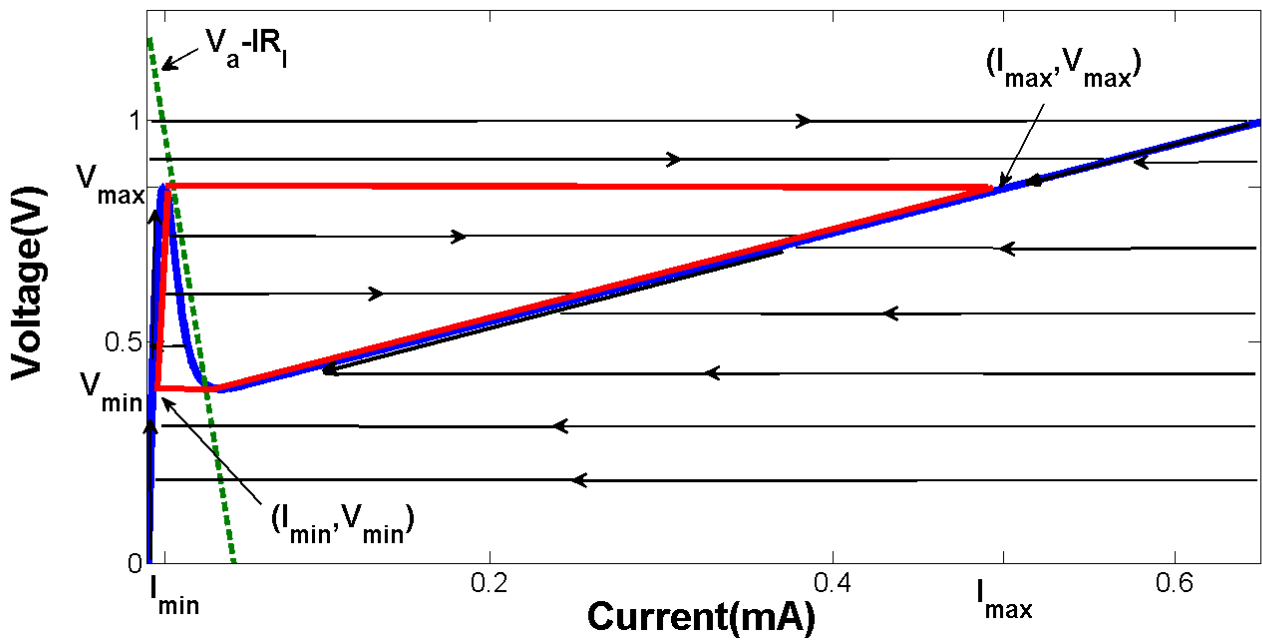
Figure 6.5: Phase diagram of relaxation oscillations with the simplified model for threshold switching of equation (6.13). Note that the load line in green intersects the $V(I)$ curve in blue from equation (6.13) in the NDC region. The region where oscillations occurs is highlighted in red and is delimited by the lines form between the points $(I_1, V_1)$, $(I_{max}, V_{max})$, $(I_2, V_2)$ and $(I_{min}, V_{min})$. A complete description of these lines is on the text. Here we highlight the points $(I_{min}, V_{min})$ and $(I_{max}, V_{max})$ which help in the description of the red region. The DC load line is green and it is described by $V(I) = V_a - IR_l$.

resistance has to be in the range $[R_1, R_2]$ where $R_1$ and $R_2$ are the slope of the lines connecting the points $(0, V_a)$ with $(I_0, V_0)$ and $(I_1, V_1)$ respectively. Values for $R_1$ and $R_2$ are calculated by equation (6.22) resulting in $R_1 = 19.23$ k$\Omega$ and $R_1 = 37.66$ k$\Omega$. According to the parameters used in this analysis (in 6.12), the slope of the load line (described by $V(I) = V_a - IR_l$) is $R_l = 20$ k$\Omega$, which clearly allows to exhibit oscillations under these parameters.

In Figure 6.6 we illustrate a comparison of relaxation oscillations under the two different models for threshold switching presented in equation (6.9) and equation (6.13).
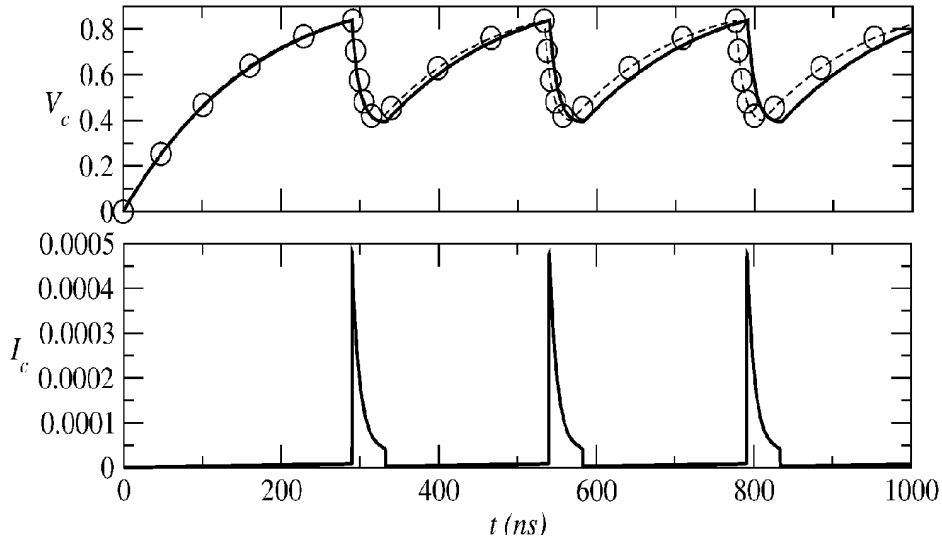


Figure 6.6: Comparison of relaxation oscillations using the simple model (6.13) for threshold switching, with parameters in Table 6.1. The dashed line shows the oscillations for the full model in equation (6.9).

## 6.5 Discussion of relaxation oscillations in $Ge_2Sb_2Te_5$ material

In contrast to the model used in [152, 158] we obtained an explicit and more robust system of ODE's that provides relaxation oscillations the $Ge_2Sb_2Te_5$ phase change material. We should point out the requirement of a limiting inductance in the system of ODE's. The necessity of this parasitic inductance is general for a circuit in parallel with a negative

resistive elements [157, 150, 154, 153]. More important, it has been reported in several publications that to correctly model the relaxation oscillations in systems with negative differential conductivity [157, 150, 154, 153] it necessary to incorporate the parasitic inductance. It should also be mentioned that to obtain relaxation oscillations we do not require to incorporate the full dynamics of the excess trap density in the "ON" layer described in (6.3).

We obtained a simple explicit function for modeling the $V - I$ characteristic curve that seems to approximate the characteristic curve obtained in [152] very accurately without losing smoothness at any point. With this simplified model, we also obtained relaxation oscillations that were in very good agreement with the full Ielmini model. In contrast to the Ielmini model of threshold switching, our simplified model only requires a small number of parameters. Moreover, some of the parameters of the Ielmini model can be very difficult to measure or to calculate.

The oscillations in [152, 158] exhibit an obvious damping due to the progress of crystallization at high current phases of the oscillations during the cycles. More explicitly, after 10-20 oscillations cycles, a collapse in the amplitude of the oscillation was observed as a result of the complete crystallization of amorphous dome. By adopting threshold switching phase change materials with negligible crystallization it might improve the stability of oscillations avoiding the damping effect [159]. Moreover the results about the frequency of oscillations as a function of the applied voltage obtained by Ielmini *et al* [152], suggest the possibility of tunable voltage-controlled oscillators with phase change materials. The progress of crystallization at high current phases can be modelled by reducing the amount of material $u_a$ in equation (6.6). Crystallization can be included by adding time dependence on $u_a$.

Besides the purely electronic explanation [30, 95, 152] the alternative explanation suggested by Karpov *et al* [158] (Section 3.3) attributes relaxation oscillation to the low and high conductive states of crystalline and amorphous phases. According to this model the $Ge_2Sb_2Te_5$ phase change material oscillates between the two states where a filament forms and decays creating a pathway through the electrodes.

# Chapter 7

# Threshold switching via electric field induced nucleation in phase change memory devices

Electrically-driven transitions from the amorphous to the crystalline phase in PCRAM (as seen in Chapter 4) devices exhibit characteristic threshold switching. The mainstream understanding of this threshold switching phenomenon is that it is initiated electronically via the influence of high electric fields. However, a completely different approach to these conventional electronic models of threshold switching has recently been suggested, based on electric field induced lowering of the system free energy, leading to the field induced nucleation of conducting crystal filaments. In this chapter we investigate this alternative view by carrying out physically realistic simulations of the threshold switching process in typical phase change materials and in typical device structures, both with and without electric field dependent energy contributions to the system free energy. The results show that threshold switching can be obtained by a mechanism driven purely by electric field induced nucleation, but the fields required are of the order 300 MV/m, and significantly larger than the experimentally measured threshold fields.

## 7.1   Electric field induced nucleation

A characteristic feature of the electrically-driven amorphous to crystalline (SET) transition is the existence of a threshold electric field that must be exceeded for switching to occur. As previously mentioned (Section 3.1), the mainstream understanding of this switching phenomenon is that it is based on the generation and recombination of carriers through trap levels and a generation mechanism driven by both electric field and carrier densities [30, 87, 112]. However, recent work has suggested that field induced (crystal) nucleation could instead be responsible [97, 158, 96], and models for such field-assisted nucleation were able to predict several experimental observations, such as the relationship between threshold voltage, device thickness, temperature, (switching) delay time and relaxation oscillations [158, 96, 32]. Such models concentrated on the role of the electric field in lowering the nucleation barrier (and the associated critical nucleus size), but were later extended by Kohary *et al* [69, 70] to include a fuller kinetic treatment that was able to identify field ranges where electric field effects might play a significant role in the crystallization [69]. However, field induced nucleation effects have not been included into physically realistic models of PCRAM devices. In this chapter, the SET (amorphous to crystal) transition in phase change "mushroom" type cells both with and without electric field induced nucleation effects is investigated. This approach might help to determine whether or not field induced nucleation could be the driving force behind the characteristic threshold switching behaviour of phase change memories.

In PCRAM devices the switching process is modelled by combining electrical, thermal and phase transformation models. The electrical and thermal models are implemented using finite element software ($Comsol^{TM}$) and simultaneously solve the Laplace and heat-diffusion equations. The phase transformations are performed through a cellular automata approach, previously described (Section 2.5). The fully coupled electrical, thermal and phase change is performed following the numerical implementation previously described in Section 4.4. In the conventional approach to electrical modeling of PCRAMs, the experimentally observed threshold switching effect is usually described by some form of field-dependent electrical conductivity for the amorphous phase [94, 87, 30, 108]. More specifically, the electrical conductivity of amorphous phase ($\sigma_{amor}$) of $Ge_2Sb_2Te_5$, as used

so far in this thesis, was described in equation (4.8).

However, if threshold switching is really a result of field induced nucleation rather than a field-dependent conductivity of the amorphous phase, then an appropriate modeling approach would have to include electric field energy terms in the crystallization model while excluding field-dependent conductivity from the electrical model; such an approach is used below and we compare the results to those obtained from a more conventional switching model.

## 7.2 Field induced nucleation in a $Ge_2Sb_2Te_5$ continuous thin film

The concept of the electric field induced nucleation in $Ge_2Sb_2Te_5$ has been introduced by Karpov et al. [31, 96, 97] and later extended by Kohary in [69, 160, 79]. This approach is based on the decrease of the electrostatic energy of the system by the formation of a relatively high-conducting crystal nucleus in a relatively non-conducting amorphous matrix. This nucleated particle decreases the electrostatic energy ($W_E$) according to [97] as in (3.7). Therefore, the Gibbs free energy $F$ of the new particle in the presence of the field is

$$F = A\sigma - \Omega\mu + W_E \tag{7.1}$$

where $A$ and $\Omega$ are the particle surface area and volume of the conductive particle respectively, $\sigma$ is the surface tension, and $\mu$ is the chemical potential between the two phases. The critical radius ($R_{sph}$) and nucleation barrier ($W_{sph}$) are calculated by minimizing the Gibbs free energy $F$. In the case of spherical nuclei, the expressions for $R_{sph}$ and $W_{sph}$ are given by (3.9) and (3.10).

The Gibbs free energy $G$ determines the rate at which each of the possible events (nucleation, growth and dissociation) in the previously described Gillespie cellular automata (GCA) approach can occur and is given by

$$G = (A\sigma - Vg) \tag{7.2}$$

where $A$ and $V$ are the surface area and volume, respectively, of a crystal cluster, $\sigma$ is the surface energy and $g$ the bulk free energy difference between the amorphous and crystalline phases. In traditional theoretical treatments of crystallization in phase change materials [49, 87, 18], the bulk energy difference term $g$ is considered to be dependent only on temperature via a form such as:

$$g = g(T) = H_f \left[ \frac{7T}{T_m} \frac{(T_m - T)}{(T_m + 6T)} \right] \tag{7.3}$$

where $H_f$ is the enthalpy of fusion and $T_m$ is the melting point [49]. However, according to recent works [32, 69, 96, 97, 158] the formation of a (relatively) high conductivity crystal nucleus in an otherwise (relatively) non-conducting amorphous matrix will decrease the electrostatic energy $(W_E)$ of the system. To elucidate the role of the electric field $E$, the additional term can be incorporated into our $GCA$ simulator by adding an electric field term to the bulk free energy difference $g$. Therefore $g$ can be considered as a function of both temperature and of the electric field:

$$g = g(T) + g(E), \tag{7.4}$$

with

$$g(E) = \frac{E^2 \varepsilon}{2n}, \quad and \quad \varepsilon = \varepsilon_0 \varepsilon_r, \tag{7.5}$$

where $\varepsilon_0$ the electric permittivity of free space, $\varepsilon_r$ the relative permittivity and $n$ is the depolarising factor, which is 1/3 for a spherical particle [69]. Using (7.4) and (7.5) the rates $R(T, E)$ at which a site $(i, j)$ transforms from amorphous to crystalline (as previously in 2.44) is now given by

$$\mathcal{R}(T, E) = \upsilon \exp\left( \frac{E_a}{k_B T} \right) \left[ -\frac{A\sigma + Vg}{2k_B T} \right] \tag{7.6}$$

where $E_a$ is the activation energy, $A$ and $V$ are the surface and volume of a basic unit (monomer) of the crystalline phase (for example in $Ge_2Sb_2Te_5$ this is estimated [49] to be $2.9 \times 10^{-22}$ cm³), $k_B$ is Boltzmann's constant, $\upsilon$ is a frequency factor.

To elucidate the role of both the electric field $E$ and temperature $T$, equation (7.6) can be used together with the $GCA$ simulator described previously to simulate phase transformations in phase change materials and devices.

| Symbol | Value | Unit |
|--------|-------|------|
| $H_f$ | 1121 | J/cm$^3$ |
| $\sigma$ | 0.066 | J/m$^2$ |
| $\varepsilon$ | 100 | |
| $T_m$ | 889 | K |
| $\upsilon$ | $4\times 10^{22}$ | Hz |

Table 7.1: Crystallization parameters. See [108]

First, the crystallization of "bulk" phase change material (i.e. continuous thin films) under field induced nucleation is investigated. For this purpose the common $Ge_2Sb_2Te_5$ alloy is used and the time for a sample of this material to fully crystallize under different temperatures and electric fields is calculated. The temperatures and electric fields through the whole sample are assumed constant and uniform. Figures 7.1, 7.2 and 7.3 show the simulation results for a sample of $80 \times 80$ nm$^2$ in size. The parameter values are taken from literature [49, 69] and are summarized in Table 7.1.

Figure 7.1 illustrates the dependence on electric field and temperature of the critical nucleus size (critical radius) according to (3.9). The critical radius is practically unaffected under the presence of low fields (E < 300 MV/m), whereas large fields (E > 300 MV/m) reduce its size.

Figure 7.2 shows that at (relatively) low field values (< 100 MV/m) the overall crystallization time at any particular temperature is relatively unaffected by the presence of the field, but at larger fields (> 100 MV/m) there can be a reduction in crystallization time. For example, the crystallization time at temperature T = 480$^o$ C can be reduced from 31 ns to 10 ns in the presence of an electric field E > 100 MV/m in comparison to crystallization time under a low electric field. Another example is that the sample crystallizes in 31 ns for electric fields between 1 MV/m and 100 M/m and temperature of $\approx$ 405$^o$ C, whereas for E $\approx$ 300M V/m and temperature of T = 385$^o$C the same crystallization time is obtained. Note that the crystallization temperatures obtained here are much higher than those reported by standard calorimetry (DSC) measurements (e.g. 155$^o$C in [161]), but the recent ultra-fast DSC measurements [162] have shown

that the crystallization temperature increases drastically with heating rate (e.g., from $\approx$ 180$^o$C at 50 Ks$^{-1}$ to $\approx$ 350$^o$C at 40 000 Ks$^{-1}$).

The results of Figure 7.2 are in good agreement with the previous work by Kohary *et al* [69] where only nucleation effects were considered. However the GCA approach allows a physically realistic simulation of both nucleation and growth effects. Furthermore, with this particular advantage it is possible to determine the dominant crystallization mechanism in different regions of the (T,E) crystallization "map" in Figure 7.2. The commonly used $Ge_2Sb_2Te_5$ phase change material has been described as a "nucleation-dominant" material [19, 23]. This mechanism can be observed for temperatures below 400 $^o$C as typified in the crystal structure in Figure 7.3 (a) and Figure 7.3 (b). In contrast, at temperatures above $\approx$ 480 $^o$C coupled with electric values below 100 MV/m becomes "growth-dominated" as typified by Figure 7.3 (c). This behaviour is consistent with recent experimental results showing high growth velocity values for high temperatures [162, 35]. However there is a very interesting behaviour, illustrated in Figure 7.3 (d), when crystallization becomes again nucleation dominated for high temperatures and electric fields ($> 100$ MV/m). This is a clear indication of the role played by the electrical field induced nucleation in this region.

## 7.3 Field-induced nucleation and switching in PCRAM devices

### 7.3.1 Methodology

In the last section a detailed study of the role of the electric field induced nucleation in "bulk" phase change materials was presented. Now, with the aim to determine if field induced nucleation alone can account for the characteristic threshold switching, a real phase change device is used. For this purpose, simulations of a specific "mushroom" cell structure, as shown in Figure 4.3 in Section 4.4 were performed.

As previously (Chapter 4) the $Comsol^{TM}$ finite-element model for the electro-thermal calculations determines the local temperature and electric field, while the crystallization is modelled using the GCA code linked to (called from) $Comsol^{TM}$. In the $GCA$ approach
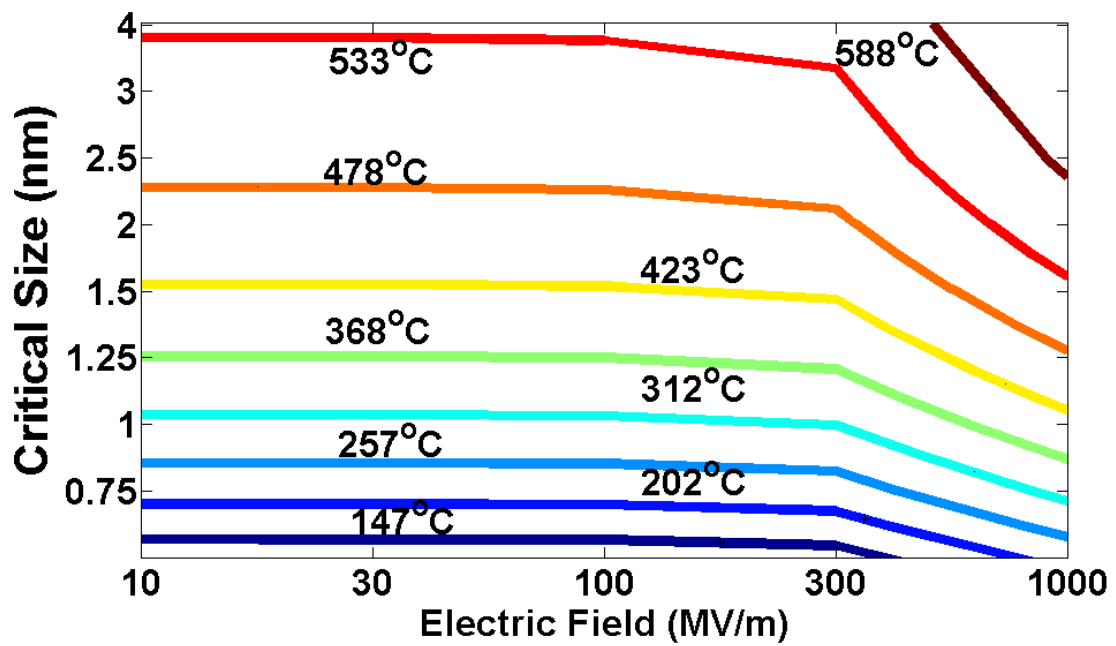
Figure 7.1: Critical radius dependence on temperature and electric field. The influence of the electric field in the critical radius is negligible for values below ($\approx 300$ MV/m), whereas above this value a decrease in the critical radius is observed. An increase on the temperature results in an increase of the critical radius.
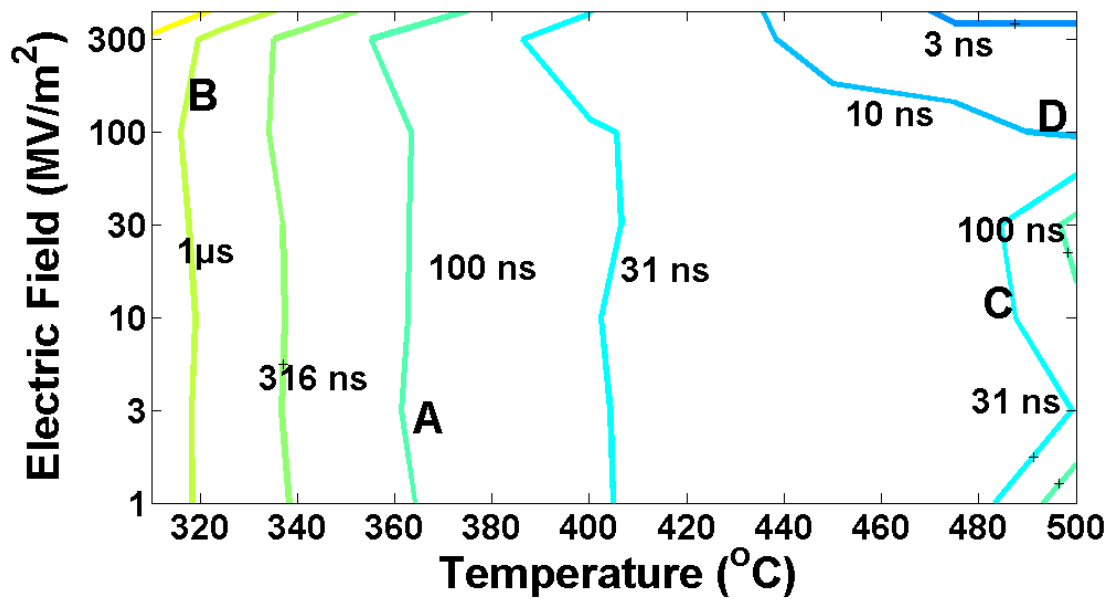
Figure 7.2: Crystallization times for the $Ge_2Sb_2Te_5$ phase change material for a sample of 80nm $\times$ 80nm in size, as a function of both temperature and electric field. The crystallization time is practically unaffected for low fields (E <100 MV/m) whereas larger fields (E > 100 MV/m) reduce the crystallization time. The letters (A)-(D) correspond to the different regions of the (T,E) crystallization nanostructure depicted in Figures 7.3(a)-(d) respectively.
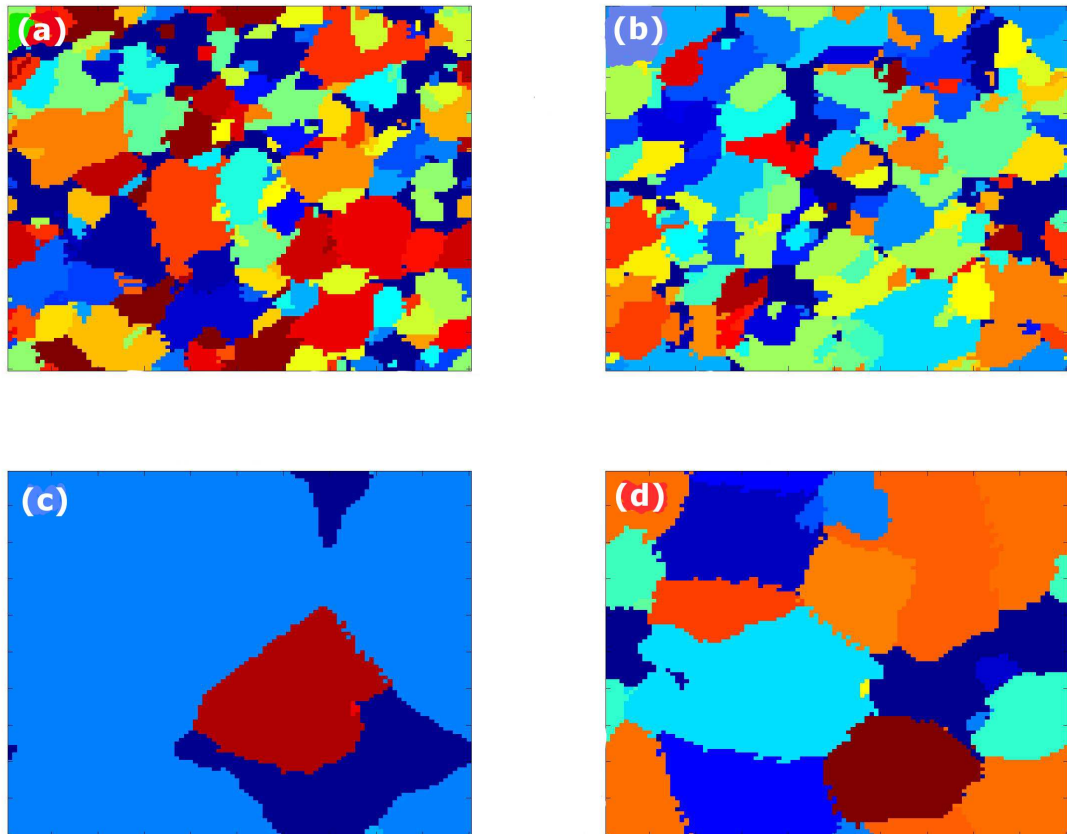
Figure 7.3: Crystalline structure of the $Ge_2Sb_sTe_5$ bulk material for the different set of points in the different regions of the (T,E) crystallization map (see Figure 7.2). For temperature below 400 $^o$C "nucleation-dominant" crystallization is observed (a)-(b). High temperatures lead to "growth-dominant" crystallization (c). At high temperatures and high fields crystallization becomes "nucleation-dominated"(d).

a rectangular mesh with square elements of size $\approx 0.82$ nm was used. Thus, the element size of the diameter corresponds to the diameter of a monomer of $Ge_2Sb_2Te_5$. In the GCA approach, the Gillespie algorithm determines an internal time step whereas for the electro$-$thermal simulations the time step is $dt = 0.5$ ns. This time step value was chosen assuming the region of interest is approximately isothermal between steps. Due to the rapid heating and cooling rates ($\approx 10^{11}$ K/s) present in PCRAM devices, the choice of $dt$ is a compromise between maintaining the isothermal assumption and giving reasonable computational times.

The crystallization behaviour and the electrical response in the "mushroom" cell structure were investigated and compared using the three different methods below:

I. The "traditional" electronic model was used to characterize the threshold switching behaviour, i.e. the amorphous phase electrical conductivity is electric-field dependent, as described by Ielmini *et al* [30]. Within this method the bulk free energy is considered to be only temperature dependent, i.e. $g_A = g(T)$

II. In this method the field energy term is added in the free energy, i.e. $g_B = g(T, E)$, while the electric-field dependence of the amorphous phase conductivity, remains the same as in Method I.

III. In this case the electric field dependence of the conductivity is removed from the threshold switching simulation, but it is assumed that the free energy depends on both temperature and the electric field, i.e, $g_C = g(T, E)$. In the case that field induced crystallization turns out to be the driving force for threshold switching, then it is expected that the characteristic threshold-type $I - V$ curves should be generated using this method.

Therefore, with Methods I and III it is possible to describe and simulate the conventional electronic approach and the field induced nucleation approach to threshold switching, respectively (while Method II combines both effects).

## 7.3.2   Results

Methods I, II and III were used to obtain $I - V$ characteristic curves in order to compare the different theories of threshold switching. For this purpose simulations for the PCRAM device of Figure 4.3, Section 4.4 were performed. The PCRAM cell was placed in series with a 10 kΩ resistor and the material parameters used in the simulations are summarised in Table 7.2. In all cases a 30 ns/30 ns ramped up/down excitation voltage was used. The results of $I - V$ simulations for the PCRAM device are shown in Figures 7.4 (a)-(b).

The $I - V$ curve obtained using a "conventional" simulation approach, i.e. assuming electric field dependent conductivity in the amorphous phase but without adding the electric field contribution to the free energy (Method I) is shown in Figure 7.4 (a) (Curve A). The characteristic threshold switching is observed with the threshold voltage being around 1 V, in good agreement with published experimental results for this type of device [87, 30]. In Figure 7.4 (a) we also show the $I - V$ curve obtained when the field dependent conductivity has been removed from the simulation (curve B). In this case no switching is observed, even for relatively high applied voltages. Here we have only shown the case where a 3 V pulse was applied. Simulations with higher applied pulses were also performed but no switching was observed (even at pulses up to 4 V).

All the $I - V$ curves obtained in Figure 7.4 (b) include the electric field contribution in the free energy. Curve C in Figure 7.4 (b) is obtained by Method III (i.e. the field does contribute to the free energy but the electric field dependence of amorphous phase conductivity is removed). Threshold switching is again observed but a significantly increased voltage (3 V) is required. Indeed if the same Method III is simulated for smaller voltage pulses than this, threshold switching behavior was not observed. Note that the "kinks" in the $I - V$ curve of case C reflect real effects and are not simulation artefacts; for example the kink at ($\approx$ 80 mA, 2.7 V) arises from a short-lived transitory re-amorphization of part of the crystallizing region during switching (and results in a final re-crystallized "dome" that is larger than the starting amorphous "dome" -see Figure 7.6 (b)). The $I - V$ curve E using Method II is also depicted in Figure 7.4 (b). This case is performed under the two assumptions, i.e. field dependence of the amorphous phase

conductivity and a field term in the free energy. Curve E also generates the characteristic S-shaped threshold switching.

The simulations presented in this section (Curves A,C,E) confirm that the characteristic S-shaped threshold switching observed in phase-change devices can be generated by the inclusion of the electric field dependent amorphous conductivity, either with or without the addition of the electric field term in the free energy.

However, when only field dependent free energy is assumed, relatively high temperatures and fields are required to produce the characteristic threshold switching. This can be observed with greater detail in Figures 7.5 (a)-(b), where the temperatures and electric fields obtained in the $Ge_2Sb_sTe_5$ layer of the PCRAM cell are shown. The final re-crystallized structure of the "active" region is also depicted in Figures 7.6 (a)-(b). Method I was used for Figures 7.5 (a) and 7.6 (a), whereas in Figures 7.5 (b) and 7.6 (b), Method III was used.

The electric fields required by Method III (field dependent term included in the free energy but the conductivity was not field dependent) to observe the switching behavior are very large ($\approx$ 270 MV/m, as in Figure 7.5 (b)). In comparison, more reasonable fields($\approx$ 60 MV/m as in Figure 7.5 (a)) are observed in the case where field dependent amorphous conductivity and no field contribution are considered (Method I). These electric field values are in good agreement with experimental measured results (eg. 56 MV/m in [109]). In the case of field induced nucleation, different simulations were performed varying the relevant parameters in (7.6) in a reasonable range without having any significant change in the threshold switching (except for the depolarising factor $n$). In Figure 7.7 we illustrate the case for a depolarisation factor of $n = 1/10$ that correspond to the crystallised nucleus elongated 5-times in the direction of the field in comparison to its diameter. Observe in Figure 7.7 the lower threshold voltage required for electrical switching in comparison to the Curve C in Figure 7.4 (b). It should be pointed out that by changing the depolarising factor to $n = 1/10$, the factor $\varepsilon/n$ in the bulk free energy (7.5) will be equal to 100/1/10=1000. In comparison the values used by Karpov *et al* [163] for $\varepsilon = 16$ and $n = 1/20$ give a factor $\varepsilon/n = 320$, which will result in a much smaller contribution to the bulk free energy term.
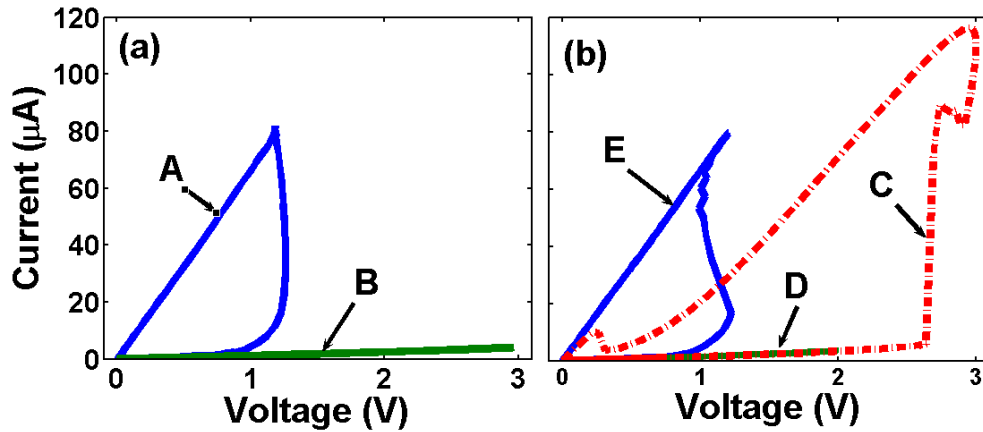
Figure 7.4: Simulated $I - V$ curves for the PCRAM device of Figure 4.3 using a 30 ns/30 ns ramped up/down applied voltage. Curve A in (a) is the $I - V$ curve obtained by Method I (i.e. amorphous phase conductivity is electric field dependent but the the free energy does not include the electric field term ); observe that the threshold switching occurs slightly above 1 V, in agreement with published experimental results [87, 30]. In (a) it is also shown curve B for which the field dependent conductivity has been removed from the simulation and no switching occurs even at high applied voltages. Curve C in (b) is the $I - V$ curve obtained by Method III (i.e. field contributes to the free energy but the dependence on the field for amorphous conductivity was removed); threshold switching is again observed but requiring a relative high voltage (3 V). In curve D the same case is simulated with smaller voltages but does not produce evidence of threshold switching. Here it is also shown the curve E obtained by Method II (i.e. field dependent conductivity and field term in free energy).
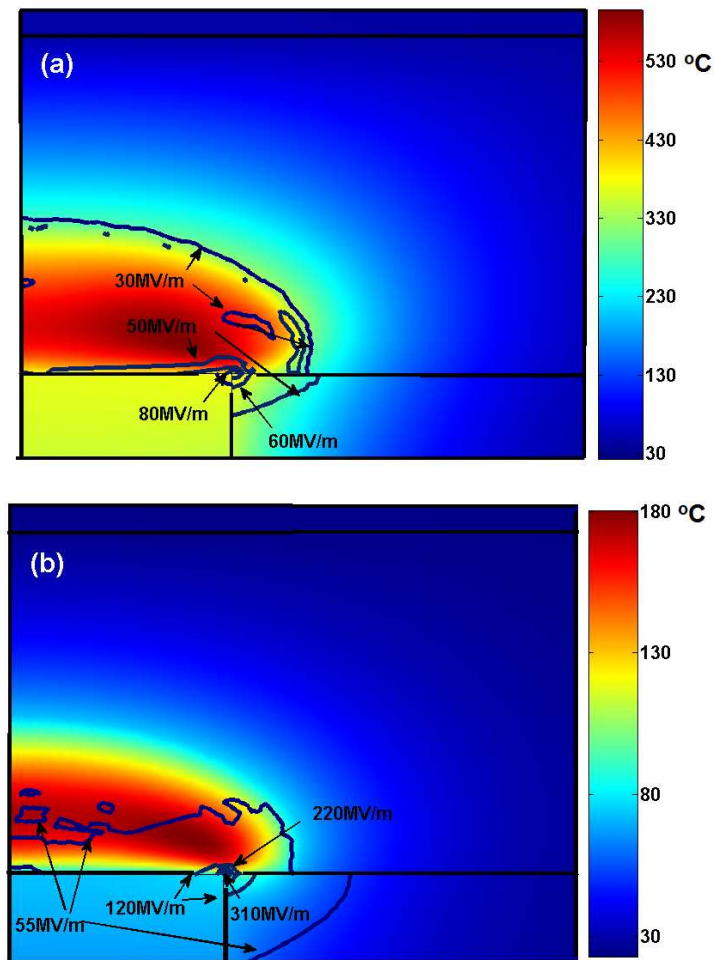
Figure 7.5: Simulated device temperature and electric fields during the SET pulse at the time when the maximum electric field is reached (i.e., at 22 ns for (a) and 27 ns for (b)). Figure 7.5 (a) was obtained using Method I. In this case the switching is electronically driven as suggested in [30]. Figure 7.5 (b) was obtained using Method III (i.e., switching is field induced driven). The SET pulse used in (a) was 2 V whereas for (b) was 3 V.
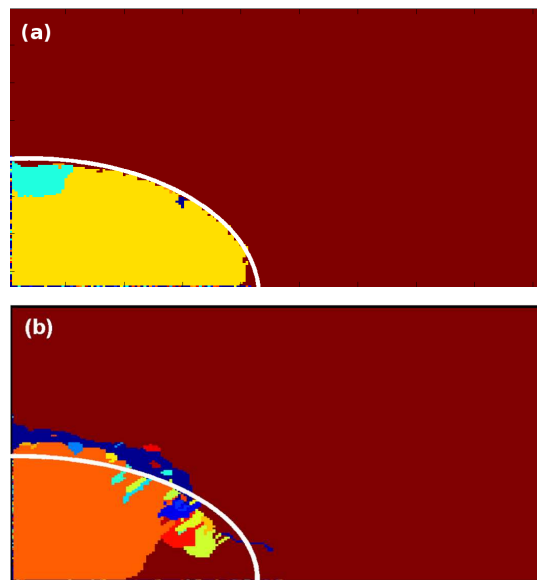
Figure 7.6: Crystalline structure at the end of the SET pulse (a)-(b). Figure 7.6 (a) was obtained using Method I. In this case the switching is electronically driven, as suggested in [30]. Figure 7.6 (b) was obtained using Method III (i.e. switching is field induced driven). The SET pulse used in (a) was 2 V whereas for (b) was 3 V. The white line represents the boundary of the initial amorphous dome. Observe in (b) a larger amorphous dome, generated as a result of a transient re-amorphization during switching.
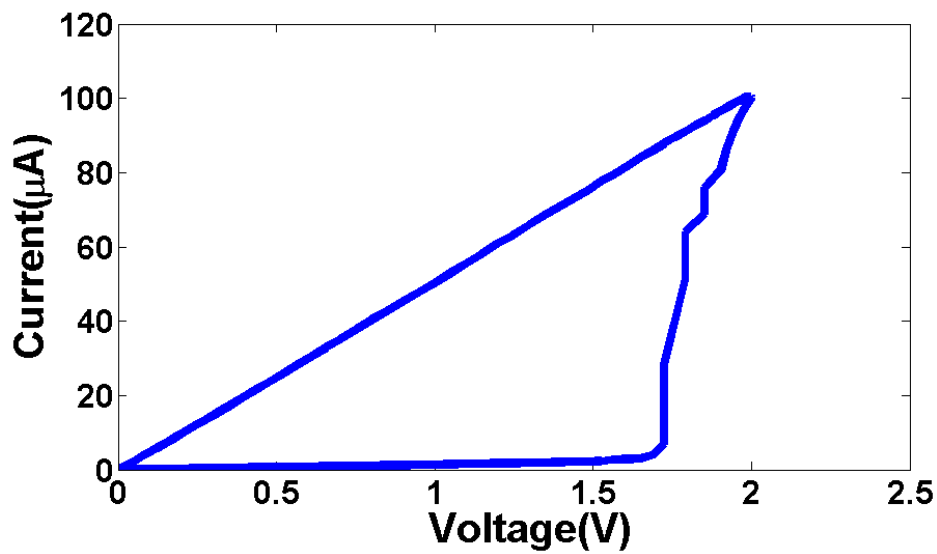
Figure 7.7: This $I - V$ curve is obtained by Method III (i.e. field contributes to the free energy but the dependence on the field for amorphous conductivity was removed). For this curve we change the depolarising factor $n = 1/10$ that corresponds to the crystallised nucleus elongated 5-times in the direction of the field in comparison to its diameter. Observe the lower threshold voltage required for electrical switching in comparison to the Curve C in Figure 7.4 (b).

| Element | K(W/mK) | C(J/m$^3$K) | $\sigma(\Omega m)^{-1}$ |
|---|---|---|---|
| $TiN(heater)$ | 17 | $7 \times 10^5$ | $1.12 \times 10^5$ |
| $TiN(electrode)$ | 19 | $2.16 \times 10^6$ | $5 \times 10^6$ |
| $SiO_2$ | 1.4 | $3.1 \times 10^6$ | $1 \times 10^{-16}$ |
| $W(electrode)$ | 175 | $2.35 \times 10^6$ | $18 \times 10^6$ |
| $Ge_2Sb_2Te_5(amorphous)$ | 0.2 | $1.25 \times 10^6$ | $\sigma_{0am} \exp(\Delta \xi_{am}/KT)$ |
| $Ge_2Sb_2Te_5(crystalline)$ | 0.5 | $1.25 \times 10^6$ | $\sigma_{0crys} \exp(\Delta \xi_{crys}/KT)$ |

Table 7.2: Thermal and Electrical material properties. See [108].

In this chapter, physically realistic simulations of the "SET" (i.e. crystallization) process in electrical phase change ($Ge_2Sb_2Te_5$) memory devices under the conventional electronic and electric field induced nucleation models were obtained. The results of such devices show that threshold switching can be obtained by a mechanism driven purely by electric field induced nucleation, as suggested by Karpov *et al* [97, 158, 96, 32]. However, electric field values obtained within this mechanism are very large($\approx$ 270 MV/m) compared to recent experimentally measured threshold fields (56 MV/m for $Ge_2Sb_sTe_5$ -see[109]). The conventional explanation of threshold switching, i.e., electronic processes leading to a field-dependent amorphous phase conductivity, is much closer to measured threshold fields and switching voltage.

The role of the electric field in the switching process has been studied and discussed, but to fully understand and explore all the limitations of phase change memory it is necessary to investigate this mechanism under different structures and devices. More important, it might be also necessary to incorporate the effect of the electric field on the activation energy of nucleation as it is been suggested recently by Li *et al* [98]. A consistent theory of threshold switching has to show some universal device properties as mentioned by Hudgens *et al* [81], such as:

  (i) Linear dependence of the threshold voltage with respect to the separation of the electrodes.

 (ii) Temperature dependence of the threshold voltage.

(iii) Holding voltage does not depend on the space between the electrodes. This holding voltage seem to depend on the electrode material properties.

(iv) The ON state does not depend on the electrode area.

(v) Turn-on delay. After the threshold voltage has been reached, there is a "switching delay" time for the high conductive state to appear.

(vi) Turn-off delay. The recovery of the initial high resistance state, once the ON state current is suppressed, shows a recovery time of the order tens of $ns$.

# Chapter 8

# Conclusions and further work

The underlying mechanisms of phase change transformations and the relation between structural and electrical properties in phase change materials are quite complex and need to be understood more deeply. Direct correlation of structural phases to their electrical states is difficult. Furthermore, detailed knowledge of the nanostructure becomes important to establish sources of variability. While at atomic scale some computational approaches have been made [163, 164, 165] none of these studies show the nanostructures of the amorphous and crystalline regions during actual electrical switching processes in real devices [44, 166, 165, 167, 168, 169]. The Gillespie Cellular Automata (GCA) approach developed in this thesis has, on the other hand, been demonstrated to be a powerful tool to understand the nanostructure evolution during realistic switching events in real devices. This GCA approach was reviewed and contrasted against some other approaches highlighting their strengths and limitations in Chapter 2. Due to the potential to span length scales between *ab initio* scale methods and bulk scale methods, the GCA approach is suitable for realistic simulations of phase change materials. The GCA approach can be enhanced in the future with the extension to a full $3D$ capability and to include important inhomogeneities such as interfacial nucleation. However such extensions may slow down the speed of simulations; in particular for 3D simulations a large increase in the number of monomers will be required. In addition, future enhancements could include dependence of crystal growth characteristics on the orientation for the crystals (anisotropy) [170].

Electrical properties, threshold switching and the relation to structural changes are crucial for application in real phase change devices. In chapter 3, we presented a review of the possible switching mechanisms that have been proposed. A full description of the purely electronic explanation by Ielmini and the non-electronic explanation for threshold switching, based on field-induced nucleation by Karpov, were described. These two theoretical approaches are used in Chapter 7 to further investigate threshold switching by carrying out physically realistic simulations in typical phase change devices. The purely electronic explanation is also used later in Chapter 6 to investigate the origin of the experimentally observed relaxation oscillations exhibited by phase change memory devices under voltage conditions near to threshold switching voltage.

In chapter 4 of this thesis, an implementation of the GCA approach in addition with the electronically-driven mechanism for threshold switching to realize physically realistic simulations of the SET and RESET processes in phase change memory devices was described. The numerical implementation given in this chapter can be used not only to perform complete coupled physical simulations in PCRAM devices, but also in any other electronic device based on phase change material, such as phase change nanowire and bridge devices. In the GCA-PCRAM simulations we obtained a detailed direct correlation between the structural phase and their electrical states during the SET and RESET process. We showed that the phase change transformation strongly depends on the details of the electrical conduction in the $Ge_2Sb_2Te_5$ material. The values for the threshold field and threshold voltage are in very good agreement with values reported in the literature.

A better understanding of transient crystallization processes, i.e., nucleation and growth rates during switching, could lead to future research work to investigate the effect of the pulse shape and duration on the phase change dynamics, so enabling faster crystallization in a similar manner to reported in [171]. Fast crystallization can also be achieved by controlling the crystallization kinetics of a phase-change material by applying a constant low voltage to induce prestructural ordering, followed by a main pulse to induce crystal nucleation and growth of the phase change material [144]. Fast crystallization under prestructural ordering may be better understood with help of the

cluster-size distribution, which can easily be obtained by the GCA approach.

In chapter 5, the energy accumulation and direct overwrite regimes in $Ge_2Sb_2Te_5$ thin film material for arithmetic computing and multistate memories were explored. The simulation results show the possibility to control reliably the partial crystallization and amorphization that lies behind new phase change arithmetic processors and multistate memories. By using the energy-accumulation property we designed and obtained (in simulation) a base-10 accumulator response in a simple nanoscale phase change device that can provide a powerful form of arithmetic computing. It should be pointed out that the computation and storage are carried out simultaneously and at the same phase-change accumulator cell, potentially providing a powerful form of non-Von-Neumann computing. We showed that the same accumulator response can also provide a particularly simple form of phase-change integrate-and-fire "neuron". The number of elements necessary for the system implementation of the phase change "neuron" is considerably less than the number of elements required by conventional CMOS neurons. It has been demonstrated recently that phase change devices can also emulate a synaptic-like response, which in combination with the phase-change integrate-and-fire "neuron" means that there is the potential to design and build "all-phase-change brain-like" (or neuromorphic) processing systems.

It should be pointed out that arithmetic computing with phase change materials and devices is a complete new field of research, providing a broad range of problems to address. For example, to reliably control the the partial crystallization for the implementation of very high-order bases it is required to have a better understanding of the structural transitions during the switching in real devices. Moreover, the intrinsic reliability characteristics of phase change devices will become critically important for the improvement in the cost and performance at the chip-level. Future investigations could also focus on the integration of the output signal generated in the spike circuit in the neuron-like system to feed a synapse element. It might be also possible to scale down the devices used and potentially employ the croos-point architecture to reach ultrahigh density and low power consumption and speed. Moreover, the full integration of synapses and neurons might be used to process information in different process like learning and

adaptation.

Besides structural transitions between amorphous and crystalline phases there are, according to Ielmini and others, also electronic switches from a low conductive state to a high conductive state (and vice versa) near the threshold voltage. The combination of electronic switching and recovery effects in $Ge_2Sb_2Te_5$ phase change memory devices gives rise to periodic oscillations when the PCRAM cell is subjected to a voltage near to the threshold switching voltage. In chapter 6, we use the electronic switching view of threshold switching to explore the possible origin of relaxation oscillations effects. We examine and argue that to correctly model the oscillations it is necessary to include a parasitic inductance in the PCRAM circuit, while the complete dynamical modelling of the carriers is not necessary. We have also considered a simplified model comprising a combination of transcendental functions that fits the V-I characteristic curve, where the model parameters represent the holding voltage, switching threshold current and voltage overshoot. With this simplified model we also obtained relaxation oscillations that were in very good agreement with the full Ielmini model and with experiments.

The effect of the dynamics of the excess trapped electron concentration could be a topic of future research. Recently Karpov *et al* [158] explained the mechanism of relaxation oscillations using the framework of field induced nucleation. In future work we could include this alternative explanation of the threshold switching suggested by Karpov *et al* [31, 32, 97]. The progress of crystallization can also be considered by adding time dependence in the description of the ON and OFF electric layers.

Finally, in Chapter 7 the threshold switching effect was revisited and two different explanations were discussed. First we investigated the crystallization of a continuous $Ge_2Sb_2Te_5$ thin film material under field induced nucleation. By doing this we were able to identify regions were the electric field potentially plays a significant role in nucleation. At low fields ($< 100$ MV/m) the overall crystallization time is unaffected by the presence of the field, but at relatively large fields ($> 300$ MV/m) there is a reduction of the crystallization time. Moreover, the GCA approach allows identification of regions of the temperature and electric field where one can find nucleation or growth dominant mechanisms. Secondly we consider the effect of field induced nucleation in a PCRAM device.

Our simulations showed that the threshold switching characteristic can be obtained by a mechanism driven purely by field induced nucleation. However, the fields necessary were relatively high ($\approx 300$ MV/m). This suggests that the explanation of threshold switching involving mainly electronic processes, such as by generation and recombination of hot electrical carriers as suggested by Ielmini *et al* [30] may be more realistic, since it predicts switching fields closer to experimentally measured values. Nevertheless, the mechanism of threshold switching is still very much a topic for debate and very much worthy of further study. It should be also pointed out that the extension to full 3D capability will be included for the study of filament formation in future investigations.

Since they were discovered in 1968 by Stanford Ovshinsky, phase change materials have revolutionized the memory technology field. Many research communities, universities and industrial research laboratories have been involved in the investigations of phase change materials and devices for binary applications. However, as shown in this thesis, phase change devices also potentially open up a new route for novel computing architecture, that combines processing and storage in a non Von-Neumann manner. The simulation and modelling tools developed in this thesis should continue to prove extremely useful in the design and understanding of such future advanced devices.

# Appendix A

# List of Publications

List of publications produced as result of the work conducted during this doctoral study.

1. Jorge A. Vázquez Diosdado, Peter Aswhin, Krisztian Kohary and C. David Wright. *Threshold switching via electric field induced crystallization in phase change memory devices*, Appl. Phys. Lett., Volume 100, Issue 25, pp. 253105, 2012.

2. C. David Wright, Jorge A. Vázquez Diosdado, L.Wang, Y-Liu, Peter Ashwin, Krisztian Kohary, M. M. Aziz, P. Hosseini, R. J. Hicken. *Exploiting the memristive-like behaviour of phase change materials and devices for arithmetic, logic and neuromorphic processing.* Nature Conference: Frontiers in Electronics Materials, Aachen, 17th - 20th Jun 2012, Technical Digests of Frontiers in Electronic Materials, pages 163-164.

3. C. David Wright, Lei Wang, Mustafa M. Aziz, Jorge A. Vázquez Diosdado and Peter Ashwin. *Phase-change processors, memristors and memflectors.* Physica Status Solidi B, 1-7 (2012), volume 249.

4. Krisztian Kohary, Jorge A. Vázquez Diosdado, Peter Aswhin and C. David Wright. *Electric-field assisted crystallisation in phase-change.* Physica Status Solidi B, 1-5 (2012),volume 249, pages 1897-1901.

5. C. David Wright, Peiman Hosseini, Jorge A. Vázquez Diosdado. *Nanoscale non Von-Neumann computing with phase-change devices.* Accepted to Adv. Func. Mat. in November 2012.

6. Krisztian Kohary, Jorge Vazquez-Diosdado, Peter Ashwin, David Wright. *Role of Enthalpy and Relative Electric Permittivity in Electric Field Induced Nucleation.* 2012 MRS Spring Meeting (San Francisco), Mater. Res. Soc. Symp. Proc., volume 1431.

7. C. David Wright, P. Hosseini and J. A. Vazquez Diosdado. *Accumulation-based Arithmetic Computing with Phase-Change Materials and Devices.* Non-Volatile Memory Technology Symposium (NVMTS). November, 2012.

8. Rosemary Cobley,C. David Wright, Jorge A. Vázquez Diosdado and Peter Ashwin. *Multilevel phase change memory spice model incorporating resistance drift effects.* To be submitted to Microelectronics Journal in December 2012.

9. Vazquez J, Ashwin P, Kohary K, Wright C. D. *Phase-change RAM modelling and design via a Gillespie-type cellular automata approach.* 2010 IEEE International Conference on Electronics, Circuits, and Systems, ICECS 2010 - Proceedings, pages 1013-1016.

10. C. D. Wright, S. Ashawaraya, P. Ashwin, M. M. Aziz, R. J. Hicken, K. I. Kohary, Y. Liu, A. S .H. Marmier, P. Shah, J. Vazquez and Lei Wang. *Phase-change technologies: from PCRAM to probe-storage to processors.* EPCOS 2010 Symposium, September 2010.

# Appendix B

# Relaxation oscillations

In this appendix, we attached the `xppaut` code that is used to simulate the relaxation oscillations in Chapter 6.

```
# DYNAMICAL VARIABLES
# current through cell
init Ic = 0.0
# voltage across capacitor
init Vc = 0.0


# CIRCUIT PARAMS
# load resistance (ohms)
par Rl = 20e3
# series resistance (ohms)
par Rs = 1e3
# voltage (V)
par Va = 1.2
# inductance (H)
par L = 1e - 7
# capacitance (F)
par C = 1e - 11
```

# MATERIAL PARAMS

# kT Boltzmann. Has change to $4.0463e-021$ in Joules

par $kT = 4.0463e-21$

# trap spacing (m)

par $dz = 5e-9$

# Ec-Ef, ET1-Ef, ET2-Ef (eV) # using $Ef = 0$ not in $eV$ in $J$

par $Ec = 5.6000e-020$ $Et1 = 0$ $Et2 = 5.4400e-020$ $Ef = 0$

# relaxation times (s)

par $taun = 1e-9$

# should be $1e-15$

# changing to $1e-17$ gives better results.

par $tau0 = 1e-15$

# Fowler-Nordheim coefficient ($1e9\ Vm^-1 = 1e7\ Vcm^-1$) in $V/m$

par $B12 = 1e9$

# carrier densities ($1e19cm^-3$ in $m^-3$)

par $Nt1 = 1e25$

par $Nt2 = 1e25$

# electron charge (coulombs)

par $q = 1.6e-19$


# CELL DIMENSION PARAMS

# thickness ($24nm$ in m)

par $ua = 2.4e-8$

# area ($1000nm^2$ in $m^2$)

# was par $A = 1e-15$

par $A = 2e-14$


# simulator

# par $alpha1 = 1e3$

# par $alpha3 = -1e5$

# par $alpha5 = 1e8$


# rescale time by scale

par $scale = 1e - 9$

# $asinh(x) = ln(x + sqrt(1 + x * x))$

$asinh(x) = ln(x + (1 + x * x)^0.5)$

# empirical fit (14/12/11 PA)

$sech(x) = 2/(exp(x) + exp(-x))$

$mu = 81571$

$h(x) = Rs * x + 0.345 * tanh(x * mu) * (1 + 4.671 * sech(x * mu)^2)$


# $nn1 = Nt1 * exp(-(Et1 - Ef)/kT)$

# not used - $nn2 = Nt2 * exp(-(Et2 - Ef)/kT)$

# from equation (2.5) with $dn2 = 0$

#

$Finside = (Ic * tau0 * exp((Ec - Ef)/kT))/(2 * q * A * dz * (Nt1 + Nt2))$

$Foff = ((2 * kT)/(q * dz)) * (asinh(Finside))$

$Foffa = abs(Foff)$

# injection from off to on layer from eqn (2.8)

$G = nn1 * exp(-B12/Foffa)/tau0$

# find thickness of off layer (corrected from (2.9)

$uaua = if(Foffa > 0)then((Et2 - Et1)/(q * Foffa))else(ua)$

$uaoff = max(0, min(ua, uaua))$

$uaon = ua - uaoff$

# balance excess trap density in "ON" layer on fast timescale

# from $dn2' = scale * (G - dn2/taun)$

$dn2 = taun * G$

# $gamma = (Nt1/(Nt1+Nt2)) * (taun/tau0) * exp(-B12/Foffa) * exp(Et2-Et1/kT)$

# from equation (2.5) with dn2 non zero

$Fon = (2*kT/(q*dz))*asinh((Ic*tau0*exp((Ec-Ef)/kT))/(2*q*A*dz*(Nt1+Nt2)*(1+(dn2/(Nt1+Nt2))*exp((Et2-Et1)/kT))))$

# voltage across cell

$V = Foff*uaoff + Fon*uaon + Rs*Ic$

# EMPIRICAL FIT to S-shaped curve

# $V = h(Ic)$

# EQUATIONS OF MOTION

# for voltage across cell and series resistance is

# Note that $L*Ic' = Vc - V$

#

$dIc = scale*((Vc-V))/L$

$dVc = scale*((Va-Vc)/Rl - Ic)/C$

$Ic' = dIc$

$Vc' = dVc$

aux uaoffis=uaoff

aux uaonis =uaon

aux Vis=V

aux Finsideis=Finside

aux Foffis=Foff

aux Fonis=Fon

aux Vcis=Vc

aux dIcis=dIc

aux dVcis=dVc

aux ddn2cis=dn2

aux Gis=G

# aux dn2is=dn2

# aux gammais=gamma

@$dt = .001, total = 1000$

@ $meth = stiff$

@ $xmin = -1, xmax = 1, ymin = -2, ymax = 2, zmin = -2.5, zmax = 7.5$

@ $xlo = -1, ylo = -2, xhi = 1, yhi = 2$

# Very big bounds!!

@ $maxstor = 10000000, bounds = 1e50$

# auto params

@ $epss = 1e - 9, epsu = 1e - 9, epsl = 1e - 9, parmax = 1, parmin = 0.05,$ $dsmax = 0.001, dsmin = 5e - 5$

@ $ds = 0.0001 \ nmax = 300 \ normmax = 1000$

# Bibliography

[1] C. Lam. Cell design considerations for phase change memory as a universal memory. pages 132–133, 2008.

[2] K. Kim. Future memory technology: challenges and opportunities. pages 5–9, 2008.

[3] N. Yamada, E. Ohno, N. Akahira, K. Nishiuchi, K. Nagata, and M. Takao. High speed overwritable phase change optical disk material. *Japanese Journal of Applied Physics*, 1987.

[4] S. Kimihiro, S. Masataka, I. Tsutomu, N. Ariyoshi, and Y. Masanobu. Near- Field Optical Recording/Readout Using a 405 nm Wavelength GaN Laser Diode. *Rev Laser Eng.,*, 35(2):86–90, 2007.

[5] Andrew Ellis, Fatima Gunning, and Tadhg Healy. Optical multiplexing for high speed systems. pages 182–182a, 2005.

[6] Ashley, J. and Bernal M.P. and Burr, G.W. and Coufal, H. and Guenther, H. and Hoffnagle, J. A. and Jefferson, C. M. and Marcus B. and Macfarlane, R.M. and Shelby, R.M and Sincerbox, G.T. Holographic data storage. volume 44, pages 341–368, 2000.

[7] D. Chen. Challenges and opportunities for optical storage. pages 13–17, 2005.

[8] R. D. Pashley and S.K. Lai. Flash memories: the best of two worlds. *IEEE Spectrum*, 26(12):30–33, 1989.

[9] Kuang-Yeu Lu, Chih-Yuan Hsieh and Liu Rich. Future challenges of flash memory technologies. *J. Micr. Eng.*, 86:283–286, 2009.

[10] R. Annunziata, P. Zulani, M. Borghi, G. De Sandre, L. Scotti, C. Prelini, I. Tosi, M.and Tortelli, and F. Pellizer. Phase change memory technology for embedded non volatile memory applications for 90 nm and beyond. volume DOI: 10.1109/IEDM, page pp. 97100, 2009.

[11] G. Servalli. 45 nm generation phase change memory technology. volume DOI: 10.1109/IEDM.2009.5424409., 2009.

[12] Marissa A. Caldwell, Simone Raoux, Robert Y. Wang, Philip H.-S Wong, and Delia J. Milliron. Synthesis and size-dependent crystallization of colloidal germanium telluride nanoparticles . *J. Mater. Chem.*, 20(7):1285–1291, 2010.

[13] T. Nirschl, J.B. Philipp, T. D. Happ, G.W. Burr, B. Rajendran, M.-H. Lee, A. Schortt, M. Yang, M. Breitwisch, C.-F. Chen, E. Joseph, M. Lamorey, R. Cheek, S.-H. Chen, S. Zaidi, S. Raoux, Y.C. Chen, Y. Zhu, R. Bergmann, H.-L. Lung, and C. Lam. Write strategies for 2 and 4-bit multi-level phase-change memory. In *Electron Devices Meeting, 2007. IEDM 2007. IEEE International*, 2007.

[14] Chieh-Fang Chen, A. Schortt, Lee M.H., S. Raoux, Shih Y.H., M. Breiwisch, F.H. Baumann, E.K. Lai, T.M. Shaw, P. Flaitz, R. Cheek, E.A. Joseph, S.H. Chen, B. Rajendran, Lung H.L., and C. Lam. Endurance Improvement of $Ge_2Sb_2Te_5$ Based Phase Change Memory. volume 44, pages 1–2, 2009.

[15] Feng Xiong, Alberto D. Liao, David Estrada, and Eric Pop. Low-Power Switching of Phase-Change Materials with Carbon Nanotube Electrodes. *Science*, 332(6029):568–570, 2011.

[16] T. Siegrist, P. Jost, H. Volker, M. Woda, P. Merkelbach, C. Schlockermann, and M. Wuttig. Disorder-induced localization in crystalline phase-change materials. *Nature Materials*, 10(3), 2011.

[17] M.H.R. Lankhorst. Modelling glass transition temperatures of chalcogenide glass. applied to phase-change optical recording materials. *J.Non-Cryst.Solids*, 297(210), 2002.

[18] D. Lencer, M. Salinga, and Matthias Wuttig. Design Rules for Phase-Change Materials in Data Storage Applications. *Adv. Mater.*, 23(18):2030–2058, 2011.

[19] S. Raoux and M. Wuttig. *Phase Change Materials Science and Applications*. Springer, San Jose, CA, 1st edition, 2008.

[20] M. Chen, K. A. Rubin, and R.W. Barton. Compound materials for reversible, phase-change optical data storage . *Appl. Phys. Lett.*, 49(9):502 – 504, 1986.

[21] S. Sakka and J.D. Mackenzie. High pressure effects on glass. *J. Non-Cryst.Solids*, 1(107-142), 1969.

[22] Yusum K., T. Nakai, S. Ashida, N. Ohmachi, N. Morishita, and N. Nakamura. Highspeed crystallization characteristics of GeSbTeBi materials used for next generation rewritable DVD with blue laser and NA = 0.65. page 211  213, 2005.

[23] Matthias Wuttig and Noboru Yamada. Phase−change materials for rewriteable data storage. *Nature Mater*, 6(824), 2007.

[24] S.R. Elliott. *Physics of Amorphous Materials*. Longman, New York, 2nd edition, 1984.

[25] K.M. Rabe and J.D Joannopoulos. Theory of the structural phase transition of GeTe. *Phys. Rev. B*, 36(6631), 1987.

[26] T. Matsunaga and N. Yamada. Structural investigation of $GeSb_2Te_4$ : A highspeed phase-change material. *Phys. Rev B*, 69:104111, 2004.

[27] Matthias Wuttig, Lüsebrink, Daniel Wamwangi, Wojciech Welnic, Michael Gilleben, and Richard Dronskowski. The role of vacancies and local distortions in the design of new phase-change materials. *Nat. Mater.*, 6:122 – 128, 2007.

[28] Simone Raoux, Welneic Woijech, and Daniel Ielmini. Phase change materials and their application to non−volatile memories. *Chem. Rev*, 110(1):240–267, 2010.

[29] P. Ashwin, B.S.V. Patnaik, and C.D Wright. Fast simulation of phase-change processes in chalcogenide alloys using a Gillespie-type cellular automata approach. *J. Appl. Phys.*, 104(8):084901, 2008.

[30] Daniele Ielmini and Yuegang Zhang. Analytical model for subthreshold conduction and threshold switching in chalcogenide based memory devices. *J. Appl. Phys.*, 102(5):054517, 2007.

[31] V.G Karpov, Y.A. Kryukov, I.V. Karpov, and M. Mitra. Field induced nucleation in phase change memory. *Physical Review B,*, 78(5):052201, 2008.

[32] V.G. Karpov, Y.A. Kryukov, S.D. Savransky, and I.V. Karpov. Nucleation switching in phase change memory . *Appl. Phys. Lett.*, 90(12):123504, 2007.

[33] D. Kashchiev. *Nucleation: Basic Theory with Applications.* Butterworth-Heinemann, Oxford, 1st edition, 2000.

[34] Alexander Milchev. *Electrocrystallization: Fundamentals of Nucleation and Growth.* Pergamon Press, Massachusetts, USA, 1st edition, 2002.

[35] Ken Kelton and Alan Lindsay Greer. *Nucleation in Condensed Matter: Applications in Materials and Biology.* Pergamon Materials Series, 1st edition, 2010.

[36] Gibbs J. *The scientific papers of J. Willard Gibbs.* Dover Publications, New York, 1961.

[37] M. Volmer and A. Weber. Keimbildung in übersättigten Gebilden. *Zeitschrift fr Physikalische Chemie*, 119(277), 1926.

[38] M. Volmer and A. Weber. Kinetische Behandlung der Keimbildung in übersättigten Dämpfen. *Annalen der Physik*, 24(719), 1935.

[39] L. Landau and E. Lifshitz. *Statistical Physics.* Pergamon Press, Oxford, 1969.

[40] J.A Kalb. *Crystallization kinetics in antimony and tellurium alloys used for phase change recording.* PhD thesis, RWTH Aachen, 2006.

[41] K.F. Kelton. Crystal nucleation in liquids and glasses. *Solid State Phys.*, 45:75–177, 1991.

[42] David T. Wu. Nucleation theory. *Solid State Phys.*, 50:37–187, 1997.

[43] T. Nonaka, G. Ohbayashi, Y. Toriumi, Y. Mori, and H. Hashimoto. Crystal structure of GeTe and Ge/sub 2/Sb/sub 2/Te/sub 5/ meta-stable phase. *Thin Solid Films*, 370(1-2):258–261, 2000.

[44] J. Akola and Jones R.O. Structural Phase Transitions on the Nanoscale: The Crucial Pattern in the Phase-Change Materials $Ge_2Sb_2Te_5$ and GeTe. *Phys. Rev. B.*, 76:235201, 2007.

[45] J.W. Christian. *The theory of transformations in metals and alloys.* Pergamon Press, Oxford, 2nd edition, 1975.

[46] Melvin Avrami. Kinetics of Phase Change. II Transformation-Time Relations for Random Distribution of Nuclei. *J. Chem. Phys*, 8(2), 1940.

[47] M.J. Starink. Kinetic equations for diffusion-controlled precipitation reactions. *J. Mater. Sci.*, 32(15):4061–4070, 1997.

[48] Michael C. Weinberg, Dunbar P. Birnie III, and Vitaly A. Shneidman. Crystallization kinetics and the JMAK equation. *J. Non-Cryst. Solids.,*, 219(1):89–99, 1997.

[49] S. Sendaker and C.D. Wright. Models for phase-change of $Ge_2Sb_2Te_5$ in optical and electrical memory devices. *J. Appl. Phys.*, 95(2):504–511, 2004.

[50] Norikazu Ohshima. Crystallization of germanium-antimony-tellurium amorphous thin film sandwiched between various dielectric protective films. *J. Appl. Phys.*, 79(5):8357, 1996.

[51] G. Ruitenberg, A.K. Petford-Long, and R.C Doole. Determination of the isothermal nucleation and growth parameters for the crystallization of thin $Ge_2Sb_2Te_5$ films . *J. Appl. Phys.*, 92(6):3116, 2002.

[52] V. Weidenhof, I. Friedrich, S. Ziegler, and M. Wuttig. Laser induced crystallization of amorphous $Ge_2Sb_2Te_5$ films. *J. Appl. Phys.*, 89(6):3168, 2001.

[53] R.F Mehl and W.A. Johnson. Reaction kinetics in processes of nucleation and growth. *AIME*, 135:416–456, 1939.

[54] J. Kohout. An alternative to the JMAK equation for a better description of phase transformation kinetics. *J. Mater. Sci.*, 43:1334–1339, 2007.

[55] D. Turnbull and J.C. Fisher. Rate of nucleation in condensed systems. *J. Chem. Phys.*, 17(1):71–73, 1949.

[56] H.B. Singh and A. Holz. Stability limit of supercooled liquids. *Solid State Communications*, 45(11), 1982.

[57] Noboru Yamada, Eiji Ohno, Kenichi Nishiuchi, and Masatoshi Takao. Rapid-phase transitions of $GeTe - Sb_2Te_3$ pseudobinary amorphous thin films for an optical disk memory . *J. Appl. Phys*, 69(5):2849, 1991.

[58] V.M. Glazov, S.N. Chizhevskaya, and N.N. Glagoleva. *Liquid Semiconductors*. Plenum Press, New Work, 1969.

[59] D. Kashchiev. Nucleation at variable supersaturation. *Surface Science*, 18(2):293–297, 1969.

[60] Konstantin B. Blyuss, Peter Ashwin, A.P Bassom, and C. David Wright. Master-equation approach to the study of phase-change processes in data storage media. *Physical Review E*, 72:011607, 2005.

[61] C.D. Wright, P. Ashwin, and K. Blyuss. Master-equation approach to understanding multistate phase-change memories and processors. *Appl. Phys. Lett.*, 90(6):063113, 2007.

[62] D.-H. Kim, F. Merget, M. Laurenzis, P.H. Bolivar, and H. Kurz. Electrical percolation characteristics of $Ge_2Sb_2Te_5$ and Sn doped $Ge_2Sb_2Te_5$ thin films during the amorphous to crystalline phase transition. *J. Appl. Phys.*, 97:083538, 2005.

[63] Alexander V. Kolobov, Paul Fons, Anatoly I.Frenkel, Alexei L. Ankudinov, Junji Tominaga, and Tomoya Uruga. Understanding the phase-change mechanism of rewritable optical media. *Nature Materials*, 3, 2004.

[64] Motoyasu Terao and Morikawa Takahito ant Ohta Takeo. Electrical Phase-Change Memory: Fundamentals and State of the Art. *Jpn.J. Appl. Phys.*, 48:080001, 2009.

[65] W. Yu, C.D. Wright, S.P. Banks, and E.P Palmiere. Cellular automata method for simulating microstructure evolution. In *Science, Measurement and Technology, IEE Proceedings*, 2003.

[66] S. Vendantam and B.S.V. Patnaik. Efficient numerical algorithm for multiphase field simulations. *Phy. Rev. E*, 73:E016703, 2006.

[67] Daniele T. Gillespie. Exact stochastic simulation of coupled chemical reactions. *J. Phys. Chem.*, 81(25):2340, 1977.

[68] Yang Cao, Daniele T. Gillespie, and Linda R. Petzold. Adaptive explicit−implicit tau-leaping method with automatic tau selection. *J. Chem. Phys.*, 126(22):224101, 2007.

[69] Krisztian Kohary and C.David Wright. Electric field induced crystallization in phase−change materials for memory applications. *Appl. Phys. Lett.*, 98(22):223102, 2011.

[70] Jorge A. Vázquez Diosdado, Peter Aswhin, Krisztian Kohary and C. David Wright. Threshold switching via electric field induced crystallization in phase change memory devices. *Appl. Phys. Lett.*, 100(25):253105, 2012.

[71] Alain Karma and Wouter-Jan Rappel. Quantitative phase-field modeling of dendritic growth in two and three dimensions. *Phys. Rev. E*, 57(4):4323–4349, 1998.

[72] Konstantin B. Blyuss, Peter Ashwin, C. David Wright, and Andrew P. Bassom. Front propagation in a phase field model with phase-dependent heat absorption. *Phys. D*, 215(2):127–136, 2006.

[73] Ingo Steinbach and Oleg Shchyglo. Phase-field modelling of microstructureevolution in solids: Perspectives and challenges. *Applications of Phase Field Modeling in Materials Science and Engineering*, 15(3):87–92, 12011.

[74] Peter Stefanovic, Mikko Haataja, and Nikolas Provatas. Phase field crystal study of deformation and plasticity in nanocrystalline materials. *Physical Review E*, 80(4):046107, 2009.

[75] T.H. Lee and S.R. Elliott. Ab Initio Computer Simulation of the Early Stages of Crystallization: Application to $Ge_2Sb_2Te_5$ Phase-Change Materials. *Phys. Rev. Lett.*, 107(14), 2011.

[76] B.J. Kooi. Extension of the Johnson-Mehl-Avrami-Kolmogorov theory incorporating anisotropic growth studied by Monte Carlo simulations . *Phys. Rev. B.*, 73(5):054103, 2006.

[77] Zhaohui FAN and David E. Laughlin. Three dimensional crystallization simulation and recording layer thickness effect in phase change optical recording. *Jpn. J. Appl. Phys.*, 42(800-803), 2003.

[78] R. Kobayashi, J.A Warren, and W.C. Carter. Vector-valued phase field model for crystallization and grain boundary formation. *Phys. D*, 119(3-4):415–423, 1998.

[79] Krisztian Kohary, Jorge A. Vázquez Diosdado, Peter Ashwin, and Wright C. David. Electric-field-assisted crystallisation in phase-change materials . *Phys. Status Solidi B*, 249(10):1897–1901, 2012.

[80] Stanford Ovshinsky. Reversible electrical switching phenomena in disorder structures. *Phys. Rev. Lett.*, 21(20):1450–1453, 1968.

[81] Stephen Hudgens. Progress in understanding the Ovshinsky Effect: Threshold switching in chalcogenide amorphous semiconductors . *Phys. Status Solidi B*, 249(10):1951–1955, 2012.

[82] I. Friedrich, V. Weldenhof, W. Njoroge, P. Franz, and M. Wuttig. Structural transformations of $Ge_2Sb_2Te_5$ films studied by electrical resistance measurements. *J. Appl. Phys.*, 87:4130–4134, 2000.

[83] B.K. Ridley. Specific negative Resistance in Solids. *Proc. Phys. Soc.*, 82(6):169–178, 1963.

[84] H.K. Henisch. Amorphous-semiconductor switching. *Sci. Am.*, 221(30):30–41, 1963.

[85] Kurl E. Petersen and David Adler. A model for the on state of amorphous chalcogenide threshold switches . *J. Appl. Phys.*, 50(7), 1979.

[86] S.H. Lee and H.K. Henisch. Threshold switching in chalcogenide glass films. *Appl. Phys. Lett.*, 22(5):230, 1973.

[87] A. Redaelli, A. Pirovano, A. Benvenuti, and A.L. Lacaita. Threshold switching and phase transition numerical models for phase change memory simulations. *J. Appl. Phys.*, 103:111101, 2008.

[88] Hellmut Fritzsche. Why are chalcogenide glasses the materials of choice for Ovonic switching devices? *Nature Materials*, 68:878–882, 2007.

[89] D. Adler, M.S Shur, and M. Silver. Threshold switching in chalcogenide glass thin films. *J. Appl. Phys.*, 51(6):3289, 1980.

[90] A. Pirovano, Lacaita A.L., F. Pellizer, S.A. Kostylev, A. Benvenutti, and R. Bez. Reliability study of phase-change nonvolatile memories. *IEEE Trans. On Materials Reliability*, 4(3):422–427, 2004.

[91] R.A Street and N.F. Mott. States in the Gap in Glassy Semiconductors. *Phys. Rev. Lett*, 35(19):1293, 1975.

[92] N.F. Mott and E.A. Davis. *Electronic Processes in Non-Crystalline Materials.* Clarendon Press, Oxford, 1971 edition, 1979.

[93] David Adler. Switching phenomena in thin films. *J. Vac. Sci. Technol*, 10(728), 1973.

[94] H.-S.P Wong, S. Raoux, Kim S., J. Liang, J.P. Reifenberg, Bipin Rajendran, Mehdi Asheghi, and Kenneth E. Goodson. Phase change memory, a comprehensive and thorough review of pcm technologies, including a discussion of material and device issues, is provided in this paper. In *Proceedings. of the IEEE*, volume 3, 2010.

[95] Simone Lavizzari, Daniele Ielmini, and Andrea L. Lacaita. Transient model for recovery and relaxation oscillations in phase-change memories. *IEEE TRANSACTIONS ON ELECTRON DEVICES*, 57(3257-3264), 2010.

[96] I.V Karpov, M. Mitra, D. Kau, G. Spadini, Y.A Kryukov, and V.G Karpov. Evidence of field induced nucleation in phase change memory. *J. Appl. Phys.*, 92(17):173501, 2008.

[97] M. Nardone, V.G. Karpov, D.C.S. Jackson, and I. V. Karpov. A unified model of nucleation switching . *Appl. Phys. Lett.*, 94(10):103509, 2009.

[98] J.M. Li, Yang H.X., and Lim K. G. Field-dependent activation energy of nucleation and switching in phase change memory. *Appl. Phys. Lett.*, 100(263501), 2012.

[99] Dominic Lencer, Martin Salinga, Blazej Grabowski, Tilmann Hickel, Jörg Neugebauer, and Matthias Wuttig. A map for phase-change materials. *Nat. Mater.*, 7:972–977, 2008.

[100] G.W. Burr. Overview of candidate device technologies for storage-class memory. *IBM J, Res.Dev*, 52(210):449–464, 2008.

[101] T. Kaplan and D. Adler. Electrothermal switching in amorphous semiconductors. *J. Non-Crystals. Solids.*, 8:538–543, 1972.

[102] D.M. Kroll and M.H. Cohen. Theory of electrical instabilities of mixed electronic and thermal origin. *J. Non-Crystals. Solids.*, 8:544–551, 1972.

[103] C.D. Wright, P. Shah, Lei Wang, M. M. Aziz, A. Sebastian , H. Pozidis. Write strategies for multi-Terabit per square inch scanned-probe phase-change memories. *Appl. Phys. Lett.*, 97(17):173104, 2010.

[104] Ho-Ki Lyeo, David G. Cahill, Bong-Sub Lee, John R. Abelson, Min-Ho Kwon, Ki-Bum Kim, Stephen G. Bishop, and Byung-Ki Cheong. Thermal conductivity of phase-change material $Ge_2Sb_2Te_5$. *Appl. Phys. Lett.*, 89(15):151904, 2006.

[105] E.-K Kim, S.-I. Kwun, S.-M Lee, H. Seo, and J.-G Yoon. Thermal boundary resistance at $Ge_2Sb_2Te_5/ZnS : SiO_2$ interface. *Appl. Phys. Lett.*, 76(26):126852, 2000.

[106] Chubing Peng, Lu Cheng, and Mansuripur M. Experimental and theoretical investigations of laser-induced crystallization and amorphization in phase-change optical recording media. *Appl. Phys. Lett.*, 82(9):4183, 1997.

[107] V. Giraud, J. Cluzel, V. Sousa, A. Jacquot, A. Dauscher, B. Lenoir, H. Scherrer, and S. Romer. Thermal characterization and analysis of phase change random access memory. *Appl. Phys. Lett.*, 98(1):013520, 2005.

[108] L. Wang, P. Shah, M.M. Aziz, E. Varesi, R. Bez, M. Moroni, and F. Cazzaniga. The Design of Rewritable Ultrahigh Density Scanning-Probe Phase-Change Memories . *IEEE Trans. Nanotech.*, 10(900), 2011.

[109] D. Krebs, S. Raoux, C.T. Rettner, G.W. Burr, M. Salinga, and M. Wuttig. Threshold field of phase change memory materials measured using phase change bridge devices. *Appl. Phys. Lett.*, 95:082101, 2009.

[110] J. Vazquez, P. Ashwin, K. Kohary, and C.D. Wright. Phase-change RAM modelling and design via a Gillespie-type cellular automata approach. In *Electronics, Circuits, and Systems (ICECS), 2010 17th IEEE International Conference on, 12th - 15th Dec 2010, IEEE Explore, no. ICECS 2010*, pages 1013–1016, 2011.

[111] David A. Drachman. Do we have brain to spare? *Neurology*, 64:2004–2005, 2005.

[112] Duygu Kuzum, Rakesh G.D. Jeyasingh, Byoungil Lee, and H.-S. Philip Wong. Nanoelectronic Programmable Synapses Based on Phase Change Materials for Brain-Inspired Computing. *Nano Lett.*, 12(5):21792186, 2011.

[113] Yang Dan and Mu-Ming Poo. Spike timing-dependent plasticity: From synapse to perception. *Physiol. Rev.*, 86:10331048, 2006.

[114] C. Dorio, David Hsu, and Miguel Figueroa. Adaptive cmos: from biological inspiration to systems-on-a-chip. volume 90, pages 345–357, 2002.

[115] L.O Chua. Memristor-the missing circuit element. *IEEE Trans. Circuit Theory*, 18(507-519), 1971.

[116] James M. Tour and Tao He. Electronics: The fourth element. *Nature*, 453:42–43, 2008.

[117] Sung Hyun Jo, Ting Chang, Idongesit Ebong, Bhavitavya B. Bhadviya, Pinaki Mazumder, and Wei Lu. Nanoscale Memristor Device as Synapse in Neuromorphic Systems. *Nano Lett*, 10(4):1297–1301, 2010.

[118] Krisztian Kohary, Jorge A. Vázquez Diosdado, Peter Ashwin, and Wright C. David. Phase-change processors, memristors and memflectors. *Phys. Status Solidi B*, 249(10):1978–1984, 2012.

[119] C. D. Wright, J. A. Vazquez-Diosdado, L. Wang, Liu Y., P. Ashwin, K.I. Kohary, M. M. Aziz, P. Hosseini, and R.J. Hicken. Exploiting the memristive-like behaviour of phase-change materials and devices for arithmetic, logic and neuromorphic processing. pages 163–164, 2012.

[120] Qianfgei Xia. Nanoscale resistive switches: devices, fabrication and integration. *Appl. Phys. A.*, 102(4):955–965, 2011.

[121] Chang Ting Jo, Sun Hyun, Idongesit Ebong, Bhavitavya B. Bhadviya, Pinaki Mazumder, and Wei Lu. Nanoscale Memristor Device as Synapse in Neuromorphic Systems. *Nano. Lett.*, 10(4):12971301, 2010.

[122] Fabien Alibart, Stéphanie Pleutin, David Guerin, Christophe Novembre, Stéphane Lefant, Kamal Lmimouni, Christian Gamrat, and Dominique Vuillaume. An Organic Nanoparticle Transistor Behaving as a Biological Spiking Synapse. *Adv. Funct. Mater.*, 20:330337, 2010.

[123] M. Suri, O. Bichler, D. Querlioz, O. Cueto, L. Perniola, V. Suosa, D. Vuillaume, C. Gamrat, and B. DeSalvo. Phase change memory as synapse for ultra-dense neuromorphic systems: Application to complex visual pattern extraction. pages 4.4.1–4.4.4, 2011.

[124] Kuzum Duygu and R.G.D. Jeyasingh. Energy efficient programming of nanoelectronic synaptic devices for large-scale implementation of associative and temporal sequence learning. pages 30.3.1–30.3.4, 2011.

[125] Mana Suri, Oliver Bichler, Damien Querlioz, Boubacar Traoré, Olga Cueto, Luca Perniola, Veronique Suosa, Dominaque Vuillame, Christian Gamrat, and Barbara DeSalvo. Physical aspects of low power synapses based on phase change memory devices . *J. Appl. Phys.*, 112(5):054904, 2012.

[126] C. David Wright, Yanwei Liu, Krisztian I. Kohary, Aziz Mustafa M., and Robert J. Hicken. Arithmetic and Biologically-Inspired Computing Using Phase-Change Materials . *Adv. Mat.*, 23(30):3408–3413, 2011.

[127] Shimeng Yu, Yi Wu, R. Jeyasingh, D. Kuzum, and H.P. Wong. An Electronic Synapse Device Based on Metal Oxide Resistive Switching Memory for Neuromorphic Computation. *IEEE Transaction on Electron Devices*, 58(8):2729–2737, 2011.

[128] C. David Wright, Peiman Hosseini, and Jorge A. Vazquez Diosdado. Nanoscale non von-Neumann computing with solid-state phase-change devices. *Adv. Mat.*, Accepted, 2012.

[129] K. Nakayama, M. Takata, A. Kasai, A. Kitagawa, and J. Akita. Pulse number control of electrical resistance for multi-level storage based on phase change. *J. Phys. D, Appl. Phys.*, 40(17):5061–5065, 2007.

[130] Stanford R. Ovshinsky. Optical Cognitive Information Processing  A New Field. *Jpn. J. Appl. Phys.*, 43:4695, 2004.

[131] C.D. Wright, M. Armand, and M. M Aziz. Terabit-Per-Square-Inch Data Storage Using Phase-Change Media and Scanning Electrical Nanoprobes. *IEEE Trans. Nanotechnol.*, 5(1):50–61, 2006.

[132] N. Papandreou, A. Panzati, A. Sebastian, E. Eleftheriou, M. Breitwisch, C. Lam, and H. Pozidis. Estimation of amorphous fraction in multilevel phase-change memory cells. *Solid-State Electron*, 54(9):991–996, 2010.

[133] D. Ielmini, D. Sharma, S. Lavizzari, and A. L. Lacaita. Reliability Impact of Chalcogenide-Structure Relaxation in Phase-Change Memory (PCM) CellsPart I: Experimental Study. *IEEE TRANSACTIONS ON ELECTRON DEVICES*, 56(5), 2009.

[134] D. Ielmini, D. Sharma, S. Lavizzari, and A. L. Lacaita. Reliability Impact of Chalcogenide-Structure Relaxation in Phase-Change Memory (PCM) CellsPart II: Physics-Based Modeling. *IEEE TRANSACTIONS ON ELECTRON DEVICES*, 56(5), 2009.

[135] N. Papandreou, A. Sebastian, Pantazi, M. Breitwisch, C. Lam, H. Pozidis, and E. Eleftheriou. Drift-resilient cell-state metric for multilevel phase-change memory. pages 3.5.1–3.5.4, 2011.

[136] D. Kuzum, R.G.D. Jeyasingh, and H.-S.P. Wong. Energy efficient programming of nanoelectronic synaptic devices for large-scale implementation of associative and temporal sequence learning. pages 30.3.1–30.3.4, 2011.

[137] Mukut Mitra, Yeonwoong Jung, Daniel S. Gianola, and Ritesh Agarwal. Extremely low drift of resistance and threshold voltage in amorphous phase change nanowire devices. *Appl. Phys. Lett.*, 96(22):222111, 2010.

[138] Giacomo Indervi, Bernabé Linares-Barranco, Tara Julia Hamilton, André van Schaik, Ralph Etienne-Cummings, Tobi Delbruck, Shih-Chii Liu, Piotr Dudek,

Philipp Häfliger, Sylvie Renaud, Johannes Schemmel, Gert Cauwenberghs, John Arthur,Kai Hynna, Fopefolu Folowosele, Sylvain Saighi, Teresea Serrano-Gotarredona, Jayawan Wijekoon, Yingxue Wang and Kwabena Boahen. Neuromorphic silicon neuron circuits. *Front. Neuroscience*, 5(73):1–23, 2011.

[139] Jayawan H. B. Wijekoon and Piotr Dudek. Compact silicon neuron circuit with spiking and bursting behaviour. *Neural Networks*, 21(2-3):524534, 2008.

[140] J.H.B Wijekoon and P. Dudek. Simple analogue vlsi circuit of a cortical neuron. pages 341–368, 2000.

[141] Giacomo Indervi and Chiara Bartolozzi. Synaptic dynamics in analog vlsi. *Neural Comput.*, 19(10):2581–2603, 2007.

[142] R. Bez. Chalcogenide pcm: a memory technology for next decade. pages 1–4, 2009.

[143] DerChang Kau, S. Tang, I.V. Karpov, R. Dodge, B. Klehn, J.A. Kalb, J. Strand, A. Diaz, N. Leung, J. Wu, S. Lee, T. Langtry, Chang Kuo-wei, C. Papagianni, Lee Jinwook, J. Hirst, S. Erra, E. Flores, N. Righos, H. Castro, and G. Spadini. A stackable cross point phase change memory. pages 1–4, 2009.

[144] D. Loke, T. H. Lee, W.J. Wang, L.P. Shi, R. Zhao, Y.C. Yeo, T.C. Chong, and S.R. Elliott. Breaking the Speed Limits of Phase-Change Memory. *Science*, 336(6088):1566–1569, 2012.

[145] Daniele Ielmini. Threshold switching mechanism by high-field energy gain in the hopping transport of chalcogenide glasses. *Phys. Rev. B.*, 78(035308), 2008.

[146] Eckerhard Schöll. *Nonequilibrium Phase Transitions in Semiconductors*. Springer-Verlag, 1st edition, 1987.

[147] P.T. Landsberg and A. Pimpale. Recombination-induced nonequilibrium phase transitions in semiconductors. *J.Phys C*, 9:1243, 1976.

[148] Eckerhard Schöll. *Nonlinear Spatio-Temporal Dynamics and Chaos in Semiconductors*. Cambridge University Press, 1st edition, 2005.

[149] Pierre E. Schmidt and Roberto C. Callarotti. The operation of thin film chalcogenide glass threshold switches in the relaxation oscillations. *Thin Solids Films*, 42(277):277–282, 1977.

[150] Pierre E. Schmidt and Roberto C. Callorotti. Theoretical and experimental study of the operation of ovonic switches in the relaxation oscillation mode. II. The discharging characteristic during the equivalent circuits. *J. Appl. Phys.*, 55(8):3148–3152, 1984.

[151] D. Ielmini, D. Mantegazza, and Lacaita A.L. Voltage-Controlled Relaxation Oscillations in Phase-Change Memory Devices . *IEEE Electron Device Lett.*, 29(568):568 – 570, 2008.

[152] Simone Lavizzari, Daniele Ielmini, and Andrea L. Lacaita. A new transient model for recovery and relaxation oscillations in phase-change memories. *IEEE TRANSACTIONS ON ELECTRON DEVICES*, 57(1838-1845), 2010.

[153] M.P. Shaw, H.L. Grubin, and I.J. Gastman. Analysis of an inhomogeneous bulk "S-shaped" negative differential conductivity element in a circuit containing reactive elements. *Transaction on Electron Devices*, 20(2):169–178, 2011.

[154] P. R. Solomon, M.P. Shaw, and H.L. Grubin. Analysis of Bulk Negative Differential Mobility Element in a Circuit Containing Reactive Elements. *J. Appl. Phys.*, 43(1):159–172, 1972.

[155] M.P. Shaw and I.J. Gastman. Current instabilities in "S-shaped" negative differential conductivity elements. *J. Non-Crystalline Solids*, 8-10:990–1003, 1972.

[156] Bard Ermentrout. *Simulating, Analyzing, and Animating Dynamical Systems: A Guide to XPPAUT for Researchers and Students (Software, Environments and Tools)*. Society for Industrial and Applied Mathematics, 1st edition, 1987.

[157] Pierre E. Schmidt and Roberto C. Callarotti. Theoretical and experimental study of the operation of ovonic switches in the relaxation oscillation mode. I. The charging characteristic during the off state. *J. Appl. Phys.*, 55(8):3144–3147, 1984.

[158] M. Nardone, V.G Karpov, and I. V. Karpov. Relaxation oscillations in chalcogenide phase change memory. *J. Appl. Phys.*, 107(5):054519, 2010.

[159] S. Prakash, Asokan S., and D.B. Ghare. A guideline for designing chalcogenide-based glasses for threshold switching characteristics. *IEEE Electron Device Lett.*, 18(2):45–47, 1997.

[160] K.I. Kohary, J. Vazquez Diosdado, P. Ashwin, and C.D. Wright. Role of Enthalpy and Relative Electric Permittivity in Electric Field Induced Nucleation. volume 1431, 2012.

[161] J. Kalb, F. Spaepen, and M. Wuttig. Calorimetric measurements of phase transformations in thin films of amorphous Te alloys used for optical data storage . *J. Appl. Phys.*, 93(2389), 2003.

[162] J. Orava, A.L. Greer, B. Gholipour, D.W. Hewak, and C.E. Smith. Characterization of supercooled liquid $Ge_2Sb_2Te_5$ and its crystallization by ultrafast-heating calorimetry. *Nat. Mater.*, 11:279–283, 2012.

[163] V.G. Karpov, Y.A. Kryukov, M. Mitra, and I.V. Karpov. Crystal nucleation in glasses of phase change memory . *J. Appl. Phys.*, 104(5):054507, 2008.

[164] Zhimei Sun, Jian Zhoua, and Rajeev Ahuja. Structure of Phase Change Materials for Data Storage. *Phy. Rev. E*, 96(5):055507, 2006.

[165] Alexander V. Kolobov, Paul Fons, Anatoly I. Frenkel, Alexei L. Ankudinov, Junji Tominaga, and Tomoya Uruga. Understanding the phase-change mechanism of rewritable optical media. *Nature Mater*, 3:703 – 708, 2004.

[166] J. Hegedüs and S.R. Elliott. Microscopic Origin of the Fast Crystallization Ability of Ge-Sb-Te Phase-Change Memory Materials. *Nat. Mater.*, 7:399405, 2008.

[167] Z. M. Sun, J. Zhou, and R. Ahuja. Unique Melting Behavior in Phase-Change Materials for Rewritable Data Storage. *Phy. Rev. Lett.*, 98(5):055505, 2007.

[168] W. Welnic, A. Pamungkas, R. Detemple, C. Steimer, S. Blugel, and M. Wuttig. Unravelling the interplay of local structure and physical properties in phase-change materials. *Nat. Mater.*, 5:5662, 2006.

[169] Z. Sun, J. Zhou, and R. Abuja. Structure of Phase Change Materials for Data Storage. *Phys.Rev.Lett.*, 96:055507, 2006.

[170] Yeowoong Jung, Sung-Wook Nam, and Ritesh Agarwal. High-Resolution Transmission Electron microscopy Study of Electrically-Driven Reversible Phase Change in $Ge_2Sb_sTe_5$ Nanowires. *Nano Lett.*, 11(3):13641368, 2011.

[171] Dae-Hwan Kang, Nan Young Kim, Hongsik Jeong, and Byung-ki Cheong. Understanding on the current-induced crystallization process and faster set write operation thereof in non-volatile phase change memory. *Appl. Phys. Lett.*, 100(6), 2012.